

ABSTRACT

Title of dissertation: STRUCTURED PLASMA WAVEGUIDES
AND DEEP EUV GENERATION ENABLED BY
INTENSE LASER-CLUSTER INTERACTIONS

Brian David Layer, Doctor of Philosophy, 2012

Dissertation directed by: Professor Howard Milchberg
Department of Physics

Using the unique properties of the interaction between intense, short-pulse lasers and nanometer scale van-der-Waals bonded aggregates (or ‘clusters’), modulated waveguides in hydrogen, argon and nitrogen plasmas were produced and extreme ultraviolet (EUV) light was generated in deeply ionized nitrogen plasmas. A jet of clusters behaves as an array of mass-limited, solid-density targets with the average density of a gas.

Two highly versatile experimental techniques are demonstrated for making preformed plasma waveguides with periodic structure within a laser-ionized cluster jet. The propagation of ultra-intense femtosecond laser pulses with intensities up to 2×10^{17} W/cm² has been experimentally demonstrated in waveguides generated using both methods, limited by available laser energy. The first uses a ‘ring grating’ to impose radial intensity modulations on the channel-generating laser pulse, which leads to axial intensity modulations at the laser focus within the cluster jet target. This creates a waveguide with axial modulations in diameter with a period between

35 μm and 2 mm, determined by the choice of ring grating. The second method creates modulated waveguides by focusing a uniform laser pulse within a jet of clusters with flow that has been modulated by periodically spaced wire obstructions. These wires make sharp, stable voids as short as 50 μm with a period as small as 200 μm within waveguides of hydrogen, nitrogen, and argon plasma. The gaps persist as the plasma expands for the full lifetime of the waveguide. This technique is useful for quasi-phase matching applications where index-modulated guides are superior to diameter modulated guides. Simulations show that these ‘slow wave’ guiding structures could allow direct laser acceleration of electrons, achieving gradients of 80 MV/cm and 10 MV/cm for laser pulse powers of 1.9 TW and 30 GW, respectively.

Results are also presented from experiments in which a nitrogen cluster jet from a cryogenically cooled gas valve was irradiated with relativistically intense (up to 2×10^{18} W/cm²) femtosecond laser pulses. The original purpose of these experiments was to create a transient recombination-pumped nitrogen soft x-ray laser on the $2p_{3/2} \rightarrow 1s_{1/2}$ ($\lambda = 24.779$ Å) and $2p_{1/2} \rightarrow 1s_{1/2}$ ($\lambda = 24.785$ Å) transitions in H-like nitrogen (N^{6+}). Although no amplification was observed, trends in EUV emission from H-like, He-like and Li-like nitrogen ions in the 15 – 150 Å spectral range were measured as a function of laser intensity and cluster size. These results were compared with calculations run in a 1-D fluid laser-cluster interaction code to study the time-dependent ionization, recombination, and evolution of nitrogen cluster plasmas.

STRUCTURED PLASMA WAVEGUIDES
AND DEEP EUV GENERATION ENABLED BY
INTENSE LASER-CLUSTER INTERACTIONS

by

Brian David Layer

Dissertation submitted to the Faculty of the Graduate School of the
University of Maryland, College Park in partial fulfillment
of the requirements for the degree of
Doctor of Philosophy
2012

Advisory Committee:
Professor Howard Milchberg, Chair/Advisor
Professor Chris Davis
Professor Rick Ellis
Professor Hans Griem
Professor Ki-Yong Kim

© Copyright by
Brian David Layer
2012

Acknowledgments

First of all, I would like to thank my advisor, Professor Howard Milchberg. Without his guidance and faith in my potential, my life would likely have taken a very different path. The high standards he sets for those around him are what have allowed me to develop as a scientist.

I had the pleasure of sharing that journey with my fellow graduate students Dr. Sanjay Varma, Dr. Andy York and Dr. Yu-Hsin Chen. Research is a team effort, and without them none of the work I've been involved in would have been possible. I'm grateful to Dr. Riq Parra, Professor Ki-Yong Kim, Professor Vinod Kumarappan and Dr. Hua Sheng for their patience and instruction during my initial years with the group. Our new generation of graduate students, Sung-Jun Yoon, Jennifer Elle, Andy Goers, George Hine also deserves credit for their assistance, as their insights, energy and enthusiasm have made research a pleasure. I thank our theoretical counterparts, Professor Tom Antonsen and Dr. John Palastro for many interesting discussions. I'm indebted to Edd Cole for teaching me how to machine, and to Jay Pyle for his expert technical assistance. I also thank all of the other professors, post-docs, staff, graduate and undergraduate students I've worked with while at the University of Maryland.

Finally, I'd like to thank my family, without whom I would never have been able to start this process, much less finish it.

Table of Contents

List of Tables	vi
List of Figures	vii
1 Introduction to laser-cluster interactions	1
1.1 Pulsed lasers and intensity regimes	1
1.2 Nonlinear laser-matter interaction	5
1.2.1 Ionization of gases	6
1.2.2 Ionization of solids	7
1.3 Van der Waals aggregate formation	9
1.3.1 Cluster formation	9
1.3.2 Cluster characterization	11
1.3.3 Droplet formation	13
1.4 Laser-cluster interaction models	14
1.4.1 Nanoplasma model	16
1.4.2 Particle models	20
1.5 EUV and x-ray emission from nanoplasmas	21
1.5.1 Collisional excitation and spontaneous decay	22
1.5.2 Radiative recombination (2-body)	23
1.5.3 Collisional recombination (3-body)	23
1.6 Dissertation outline	25
2 Experimental apparatus	27
2.1 Overview	27
2.2 Cryogenic cluster source	28
2.2.1 Cluster source operational procedures	34
2.3 10 gigawatt 100 picosecond Nd:YAG laser	35
2.4 2 terawatt 60 femtosecond Ti:sapphire laser	38
2.5 25 terawatt 36 femtosecond Ti:sapphire laser	39
2.5.1 Coherent Micra oscillator	40
2.5.2 Coherent Legend kHz regenerative amplifier (RGA)	41
2.5.3 Multi-pass amplifier	42
3 Review of high-intensity guiding and applications	44
3.1 Overview	44
3.2 Guiding in hollow capillaries	45
3.3 Self-guided propagation	47
3.3.1 Ponderomotively driven charge displacement	47
3.3.2 Relativistic electron motion	48
3.4 Preformed plasma channels	49
3.4.1 Laser-ionized preformed plasma channels	50
3.4.2 Electrical discharge ionized preformed plasma channels	54
3.5 Guiding using cluster plasmas	55

3.5.1	Self-guided propagation	55
3.5.2	Prefomed waveguide formation	56
3.6	Applications of plasma waveguides	60
3.6.1	High harmonic generation (HHG)	60
3.6.1.1	Phase-matching	62
3.6.1.2	Quasi-phase matching	63
3.6.2	Direct acceleration of charged particles (DLA)	65
3.6.2.1	Slow waves	69
4	Modulated Plasma Waveguides	72
4.1	Experimental setup	72
4.1.1	Waveguide stability	76
4.2	Ring grating (RG) modulations	77
4.2.1	‘Beating’ of an odd number of diffracted orders	82
4.2.2	Ring grating imaging	86
4.2.3	Range of generated modulation periods	88
4.2.4	Hydrogen plasma RG modulated waveguides	93
4.2.5	Argon plasma RG modulated waveguides	94
4.3	Wire obstruction modulations	98
4.3.1	Single wire obstructions	101
4.3.2	Arrays of wire obstructions	102
5	Nitrogen cluster plasma EUV generation	106
5.1	Experimental setup	112
5.2	Neutral gas density measurements	117
5.3	Electron density measurements	120
5.4	Cluster size measurements	123
5.5	Laser energy absorption measurements	128
5.6	Spectral Data	133
5.6.1	EUV emission scaling with laser intensity	138
5.6.2	EUV emission scaling with cluster radius	142
5.7	Electron temperature extraction from EUV spectra	150
5.8	Simulations and analysis	152
5.8.1	Ionization fraction vs cluster size	155
5.8.2	Energy deposition and plasma temperature	156
5.8.3	Comparison with x-ray laser theory	160
6	Conclusion	162
6.1	Summary	162
6.2	Future work	163
6.2.1	Laser-based particle acceleration	163
6.2.2	Coherent EUV generation	164
A	Vacuum System	166

B Flat-field EUV spectrometer	170
Bibliography	176

List of Tables

1.1	Examples of condensation constants for gases commonly used in the creation of laser-produced plasmas [37].	10
-----	--	----

List of Figures

1.1	Mechanisms by which an electron within an atom can undergo field ionization by a laser. Multiphoton ionization (<i>a</i>) occurs when multiple photons strike the atom simultaneously, providing sufficient intensity to escape the Coulomb potential (solid red line). Tunnel ionization (<i>b</i>) occurs when the instantaneous laser potential (dashed blue line) is sufficient to modify the Coulomb potential and allow tunneling through the barrier on the timescale of a laser field oscillation. Over-the-barrier ionization (<i>c</i>) occurs when the laser field causes a large enough modification to the Coulomb potential that the electron can ‘fall out’.	3
1.2	Representations and photographs of the gas valve nozzle configurations used in these experiments. The nozzles were attached to commercial gas valves sealed with copper gaskets (Parker Hannifin, General Valve Division series 99). Two conical nozzle configurations were used, with a throat diameter d of 0.5 or 1 mm and an expansion half-angle α of 10° or 5° , respectively. Elongated nozzles with an orifice diameter d ranging from 0.5 to 1 mm and an exit length l of 15 mm were used.	12
1.3	Schematic representation of the 1D nanoplasma expansion model of Milchberg <i>et al.</i> [62]. The initial state of the neutral cluster is shown at the far left. Initial ionization by an intense laser pulse creates a dense, super-critical plasma that expands layer-by-layer, resonantly coupling to the plasma in the region with resonant density $-\xi E_{int}/4\pi$, where E is the electric field in the cluster and $\xi = (1 + \nu^2/\omega^2)^{-1} N_e/N_{cr}$.	18
1.4	Radiative (2-body) and collisional (3-body) recombination pathways and scaling with electron temperature and density in a plasma. These processes are the inverse processes of photoionization and collisional ionization, respectively.	24
2.1	Photograph of the cryogenic cluster source used in these experiments, shown with an 15 mm elongated nozzle installed on the solenoid valve and a plasma column created by an axicon-focused Nd:YAG laser pulse.	29
2.2	Cross-sectional drawing of a Parker Hannifin Corporation, General Valve Division, Series 99 solenoid valve with no nozzle attached.	31
2.3	The topology of the 1064 nm Nd:YAG laser system used in the plasma waveguide experiments presented in Chapter 4. The oscillator, RGA and both amplifier stages are pumped with flashlamps.	36
2.4	The topology of the 2 terawatt peak power 800 nm Ti:sapphire laser system used in the plasma waveguide experiments presented in Chapter 4.	38
2.5	The topology of the Coherent 25 TW Ti:sapphire laser system used for the nitrogen EUV experiments presented in Chapter 5.	40

2.6	3rd order autocorrelation trace showing that the ps contrast of the 25 terawatt laser system is $> 10^5$ within ± 200 ps of the main pulse.	43
3.1	Schematic of the experimental setup first used to create a preformed waveguide. A 100 ps Nd:YAG laser pulse with up to 300 mJ was brought to a line focus with an axicon, ionizing ambient gas. As the plasma column radially expands, a hydrodynamic shock wave forms a transient structure with an local on-axis electron density minimum, allowing the guiding of high intensity pulses that are synchronized to the channel-generating pulse with a delay of several nanoseconds. The $J_0(k_{\perp}r)$ Bessel beam axicon focal profile is shown.	51
3.2	Experimental radial electron density profiles reproduced from Reference [102], showing the hydrodynamic expansion of a radial shock wave in an argon cluster jet driven by a Gaussian 100 ps FWHM 1064 nm laser pulse with 150 mJ (<i>a</i>) and 230 mJ (<i>b</i>) of laser energy.	52
3.3	Schematic of the experimental setup used to create preformed plasma waveguides using a self-guided femtosecond laser pulse in an elongated cluster jet [101].	57
3.4	Photograph of the experimental setup used to create plasma waveguides in elongated cluster jets using axicon-focused 100 ps pulses.	59
3.5	Representation of the multi-stage ionization process. First, the electron is ionized (<i>a</i>) at the peak of the laser field, then it is accelerated away from the nucleus (<i>b</i>), then it recollides (<i>c</i>) emitting an EUV photon.	62
3.6	Overview of the direct laser acceleration scheme. When a relativistic seed electron bunch and a radially polarized laser pulse are injected into a modulated plasma waveguide with proper phasing, there is an axial component of the laser field that causes the electron bunch to feel net acceleration over many cycles of the laser field.	65
3.7	Schematic illustration of how a radially polarized laser pulse has an on-axis electric field component in the propagation direction of the laser when focused.	67
3.8	Schematic drawing illustrating how radially polarized light within a modulated waveguide can do work on co-propagating electrons in spite of the oscillatory nature of the electric field. When the modulation period is $L_c/2$, the electron bunch experiences one cycle of the laser field with each waveguide period, feeling a backwards push when the mode is wider and a forwards push when the mode is narrower and more intense, leading to a net gain in energy with each modulation period.	68

4.1	Experimental layout for generation of channels using the hydrodynamic shock method. An axicon-focused Nd:YAG laser pulse (200 – 800 mJ, 100 ps, 1064 nm), which overfills an elongated cluster jet target making a 15 mm plasma channel. Modulations can be imposed upon the plasma waveguide by either spatially modulating the Nd:YAG pulse with a ring grating or obstructing the cluster jet at periodic intervals with wires. Ti:sapphire laser pulses (70 mJ, 60 fs, 800 nm) were guided after being focused to the entrance of the channel entrance through a hole in the axis of the axicon.	73
4.2	Detail of the interaction region for generation of channels using the hydrodynamic shock method. First, an axicon-focused Nd:YAG laser pulse (200 – 500 mJ, 100 ps, 1064 nm) that has been radially modulated by transmission through a ring grating (<i>d</i>) creates a modulated plasma channel in an elongated cluster jet. A Ti:sapphire laser pulse (70 mJ, 60 fs, 800 nm) arrives 1 – 3 ns later and is then focused to the entrance of the guide through a hole in the axis of the axicon. The radial plasma density of the channel (<i>c</i>) was directly measured by Abel inverting the extracted phase from an interferogram (<i>b</i>) taken with a 60 fs probe pulse.	75
4.3	A sequence of 12 consecutive end mode images of guided Ti:sapphire pulses (20 mJ, 60 fs, 800 nm) in unmodulated hydrogen plasma waveguides with a relative delay of 1 ns. The channels were generated by Nd:YAG laser pulses (500 mJ, 100 ps, 1064 nm) focused in a jet of hydrogen clusters released by a source that was held at a temperature of –150° Celsius with 800 psi backing pressure. The set of images from which this sequence was taken has an RMS jitter of 2.6 μm and mean FWHM of 15.4 μm . The main source of jitter in these images pointing of the femtosecond laser prior to coupling into the waveguide, the plasma structure itself is extremely consistent.	78
4.4	Sectional diagrams showing the radius vs propagation direction as a beam travels through a ring grating and then an axicon, demonstrating how periodic modulations are imposed. The lithographic etch depth of the grating was chosen to maximize the efficiency of the $n = \pm 1$ diffracted orders, so only those are shown. The $n = -1(+1)$ diffracted order of the ring grating is an inwardly (outwardly) traveling Bessel beam which converges towards the line focus of the axicon at a sharper (shallower) angle than the $n = 0$ order beam, as shown in the first (second) row. When both are focused together as shown in the third row, they interfere on-axis, resulting in a time-averaged intensity profile with periodic axial modulations.	79

4.5	Diagram showing agreement between experimentally generated plasma profiles and a calculated intensity profile for a 40 μm ring grating, for which $\theta_{\pm 1} = 1.524^\circ$. When used in conjunction with a $\theta_{base} = 28^\circ$ base angle fused silica axicon, this corresponds to γ_1, γ_0 and γ_{-1} values of $16.742^\circ, 14.886^\circ$ and 13.067° , respectively. Plot (a) and photograph (b) predict and demonstrate a ~ 1.1 mm beat period, and plot (c) and shadowgram (d) predict and show a modulation period of ~ 130 μm . The plasma shown in (b) and (d) was generated in atmosphere.	83
4.6	Diagram showing agreement between experimentally generated plasmas and a calculated intensity profile for the focal intensity of a 100 μm ring grating, for which $\theta_{\pm 1} = 0.610^\circ$. When used in conjunction with a $\theta_{base} = 28^\circ$ base angle fused silica axicon, this corresponds to γ_1, γ_0 and γ_{-1} values of $15.624^\circ, 14.886^\circ$ and 14.155° , respectively. Plot (a) and photograph (b) of a plasma generated in atmosphere show agreement with a ~ 5.5 mm beat period, and plot (c) and probe phase image (d) (of a plasma created in an argon cluster jet) show a modulation period of ~ 330 μm	84
4.7	Transverse images of plasma channels with a 35 μm modulation period imposed using a ring grating a 10 μm radial ruling period. An axicon-focused Nd:YAG laser pulse (500 mJ, 100 ps, 1064 nm) was brought to focus in atmosphere (a) and in a uniform elongated argon cluster jet (b). Both images were taken using a transverse 60 fs Ti:sapphire probe pulse, where (a) is a raw shadowgram and (b) is the extracted phase from an interferogram.	89
4.8	Photographs of channels with a ~ 2 mm modulation period, generated in atmosphere (a) and an axially uniform elongated argon cluster jet (b). The modulations were imposed upon the channel using a ring grating with a ~ 0.6 mm radial period in the path of the axicon-focused Nd:YAG laser pulse (500 mJ, 100 ps, 1064 nm).	90
4.9	Abel-inverted radial electron density images of corrugated plasma channels made with a ring grating imaged to a hydrogen cluster jet (800 psi backing, -145° Celsius). 3 mm section of channel with (bottom panel (b)) and without (top panel (b)) a right-to-left propagating guided femtosecond pulse (70 mJ, 60 fs, 800 nm) injected 1 ns after channel formation. Exit mode from the bottom panel of (a) inset, 30 μm FWHM (c).	91
4.10	Abel-inverted radial electron density images of corrugated plasma channels made with a ring grating imaged to a hydrogen cluster jet (800 psi backing, -145° Celsius). Detail images of two periods of hydrogen plasma channels, for using 100 ps Nd:YAG laser pulse energies of (a) 200 mJ, (b) 300 mJ and (c) 500 mJ (with slight RG misalignment with respect to axicon), with interferometer probe delays, top to bottom, of 0.5 (i), 1.0 (ii) and 2.0 ns (iii).	92

4.11	Extended Abel-inverted radial electron density images of corrugated plasma channels made with a ring grating imaged to an argon cluster jet with a 330 μm axial period (800 psi backing, 22° Celsius). 3 mm section of channel with (bottom panel (b)) and without (top panel (a)) a right-to-left propagating guided Ti:sapphire pulse (70 mJ, 60 fs, 800 nm) injected 1.5 ns after channel formation. (c) Lowest order exit mode from (b), with an average FWHM of 28 μm (c). The vertical FWHM of (c) is 26 μm and the horizontal FWHM is 30 μm	95
4.12	Plasma channels modulated by a ring grating in an argon cluster jet at 800 psi backing pressure and room temperature. Magnified images at 2 ns delay of beaded (300 mJ pump, (a)) and more continuous (500 mJ pump, (b)) modulations. Left and right columns: (i) density profile of uninjected waveguide, (ii) density profile of injected waveguide, raw (iii) and Abel-inverted (iv) scattering image at 800 nm corresponding to (ii).	96
4.13	Experimental setup for waveguides modulated with cluster jet obstructions. A Nd:YAG laser pulse (200 – 500 mJ, 100 ps, 1064 nm) is brought to a line focus with an axicon, overfilling an elongated cluster jet target with periodic obstructions, making a 15 mm corrugated plasma channel. A Ti:sapphire laser pulse (70 mJ, 60 fs, 800 nm) is focused to the entrance of the guide through a hole in the axis of the axicon, guiding with electronically adjustable delay. A < 1 mJ portion of this fs pulse was used to probe the channel transversely, then sent through a folded wavefront Michelson interferometer. (b) Photograph of channel with an array of 250 μm wires with 1 mm spacing and (c) an extracted phase image of channel with 25 μm wires at a 200 μm modulation period, both in room temperature argon cluster targets.	99
4.14	Abel-inverted radial electron density images of a single break in a plasma waveguide as a function of delay, produced with a Nd:YAG pulse (1064 nm, 500 mJ, 100 ps) in 800 psi nitrogen (a – d) and argon (e – h) cluster jets at –145° and 22° Celsius, respectively. The gap in the channel was caused by a 25 μm diameter wire across the exit of the elongated nozzle. The wire is in contact with the nozzle, ~ 2 mm below the channel.	100
4.15	Waveguides with multiple wire obstructions at the nozzle exit. Abel-inverted radial electron density profile 2 ns after channel generation in (a) a nitrogen cluster jet (800 psi, –145° Celsius) and (b) an argon cluster jet (800 psi, –85° Celsius), both with 25 μm diameter wire obstructions at a 200 μm period. (c) shows a channel made using the same parameters as (b) but with a Ti:sapphire laser pulse (70 mJ, 60 fs, 800 nm) guided from right to left. In (d) Rayleigh scattering of the guided pulse in (c) is imaged by blocking the probe pulse and placing an 800 nm interference filter in the imaging setup.	103

5.1	Figures reproduced from reference [147] showing calculated maximum transient local gain coefficients G_{max} for the $2p_{3/2} \rightarrow 1s_{1/2}$ transition in uniform, fully ionized nitrogen plasmas as a function of electron density and temperature.	108
5.2	Plots of average ionization (<i>a</i>) and peak electron temperature (<i>b</i>) from a 1D hydrodynamic simulation [62] of the explosion of a 25 nm radius nitrogen cluster irradiated by a Ti:sapphire laser with peak intensity of 5×10^{17} W/cm ² and pulsewidth of 35 fs.	110
5.3	Experimental layout for the generation of laser-produced plasmas in a nitrogen cluster jet. A Ti:sapphire laser pulse (up to 830 mJ, 36 fs, 800 nm) is focused using a dielectric concave spherical mirror ($f = 1$ m) in a retro-reflecting geometry through a 4 mm diameter hole in a 45° turning mirror. Transverse profiles of the plasma and cluster jet (interferograms and shadowgrams) were gathered by sending a frequency-doubled probe pulse through an interferometer into a CCD camera. Energy throughput measurements were collected by moving a pickoff mirror on a motorized stage into the beam path of the laser after the focus. A flat-field spectrometer collected EUV spectra (1.5 – 20 nm, see Appendix B)	113
5.4	Focal spot profile of the Ti:sapphire laser focused with the $f = 1$ m concave mirror in the setup shown in Figure 5.3. This profile was directly obtained using a CCD camera and 10× magnification microscope objective, and displayed using a (<i>a</i>) standard and (<i>b</i>) logarithmic intensity colormap. Plots (<i>c</i>) and (<i>d</i>) show Y (23.4 μm FWHM) and X (34.6 μm FWHM) lineouts through the focus, respectively. 69% of the beam energy is contained within the central Gaussian profile.	115
5.5	Example image (<i>a</i>) of N ₂ molecule density extracted from a transverse interferogram when the gas valve is held at -100° Celsius with a backing pressure of 425 PSI. This cluster jet shown emerged from the 1 mm by 15 mm rectangular nozzle positioned 0.5 mm below the frame, and is flowing in the Y direction. To collect this image the probe was oriented end-on, such that it propagated through 15 mm of jet material. The inset plot (<i>b</i>) is a lineout of (<i>a</i>) at Y=1.5 mm, the height at which the pump beam strikes the jet.	118
5.6	Plot demonstrating our ability to maintain reasonably constant N ₂ molecule density over a wide range of gas valve temperatures. This effectively allows independent control of the mean cluster size and molecule density of the jet. Each data point is extracted from an image of the neutral N ₂ molecule density similar to the one shown in Figure 5.5(<i>a</i>).	119

5.7	Plots showing radial lineouts (top of each frame) from electron density profile images (bottom of each frame) measured ~ 10 ps after the arrival and passage of the pump laser (100 mJ, 36 fs, 800 nm) for gas valve temperatures of (a) -40° , (b) -70° , (c) -100° and (d) -130° Celsius. The N_2 molecule density in all four cases is $\sim 1.85 \times 10^{18}$ molecules/cm ³ , measured in Figure 5.6. In each plot, the electron density gridlines occur at multiples of the nitrogen atom density. On the right-hand side of each plot, ‘steps’ in the electron density appear to correspond to the different ionization stages of nitrogen plasma in the wings of the focal spot (Figure 5.4).	121
5.8	Layout of the auxiliary vacuum chamber used to measure the mean cluster size within the jet. In both the neutral gas density (b) and Rayleigh scattering (b) measurements, the probe beam propagated end-on through the jet, experiencing 15 mm of jet material. Taken together, these measurements allow us to calculate the mean cluster radius \bar{a} and mean cluster density n_{cl} in the jet.	125
5.9	Sample raw images of 1064 nm light scattered from (a) a cluster jet (-120° Celsius gas valve temperature, mean radius $\bar{a} = 94$ nm) and (b) a droplet jet (-165° Celsius gas valve temperature). Also shown are central lineouts for various gas valve temperatures at a constant nitrogen atom density of 1.5×10^{18} cm ⁻³	126
5.10	Plot showing average cluster radius \bar{a} and mean cluster density n_{cl} as a function of temperature for a constant nitrogen atom density of 1.5×10^{18} cm ⁻³ , extracted from the data shown in Figure 5.9. The data point at -140° Celsius corresponds to the onset of the droplet regime in which the aggregate diameter is of the order of the probe wavelength ($\lambda = 1064$ nm), where an accurate measurement of cluster size would require the incorporation of Mie terms.	127
5.11	Plot showing the region within pressure-temperature phase space accessible to the gas valve overlaid upon the vapor pressure curve of nitrogen. At backing pressures below 33 bar to the left of the vapor pressure curve, the gas valve produces a stream of liquid that fragments into droplets instead of a jet of gas in which cluster nucleation occurs.	129
5.12	Plot showing the fraction of laser pulse energy absorbed (36 fs, 800 nm) by a 1 mm thick cluster jet as a function of laser energy for select gas valve temperatures. Nitrogen atom density is $\sim 1.5 \times 10^{18}$ cm ⁻³ for all conditions. Rayleigh scattering measurements (Figure 5.10) showed that jets with larger mean cluster radii were released from lower temperature gas valves, as predicted by the Hagena parameter scaling.	131
5.13	Plot showing laser pulse energy fraction absorption as a function of laser energy when the pump laser experienced a 15 mm thick cluster jet for several nitrogen atom densities, all with the gas valve held at a temperature of -145° Celsius.	132

5.14	Example of a raw nitrogen spectrum recorded with the flat-field spectrometer using the 2400 line/mm grating. A 36 fs Ti:sapphire laser pulse with peak intensity of 4×10^{17} W/cm ² (200 mJ/pulse) irradiated a cluster jet with an average atom density of $\sim 3 \times 10^{18}$ cm ⁻³ (solenoid valve at -100° Celsius, backed by 475 PSI N ₂). A thin nickel filter prevented laser light from entering the spectrometer. He-like and H-like nitrogen emission lines are visible.	134
5.15	Example of a raw nitrogen spectrum recorded with the flat-field spectrometer using the 1200 line/mm grating. A 36 fs Ti:sapphire laser pulse with a peak intensity of 3.5×10^{17} W/cm ² (175 mJ/pulse) irradiated a cluster jet with an average atom density of $\sim 2 \times 10^{18}$ cm ⁻³ (solenoid valve at -150° Celsius, backed by 550 PSI N ₂). A thin zirconium filter prevented laser light from entering the spectrometer. Li-like, He-like and H-like nitrogen emission lines are visible in first order, and some H-like and He-like lines are visible in higher orders. Here, select first-order H-like and He-like emission lines have been labeled. In the H-like emission series shown, the 2p-Xd and 2s-Xp line pairs are not separately resolved.	135
5.16	The same spectrum shown in Figure 5.15, with a different group of emission lines labeled. Li-like emission lines and continuum are observed in the first order above at wavelengths above 125 Å. He-like and H-like emission with wavelength < 30 Å is observed in higher orders.	136
5.17	A 36 fs FWHM Ti:sapphire laser pulse energy vs valve temperature scan showing (a) H-like, (b) He-like and (c) Li-like intensity measured by summing emission lines. The H-like intensity shown is the sum of the 2p-3d, 2s-3p, 2p-5d and 2s-5p lines, He-like is the sum of 1s2p-1s4d and 1s2p-1s5d, and Li-like is the sum of 2s-6p and 2s-9p. The emission from each species grows steadily as the laser energy rises and the solenoid valve temperature drops (which increases the mean cluster size). In this data set, the nitrogen atom density was not measured, but likely increased as the temperature was decreased. . . .	139
5.18	The relative ratios of the line emission intensities from species shown in Figure 5.17. The ratio of H-like to He-like reveals that the H-like EUV emission begins at higher laser intensities than the He-like, and that the H-like to He-like emission ratio stabilizes above ~ 50 mJ (a peak intensity of 1×10^{17} W/cm ²). The H-like to Li-like (b) and He-like to Li-like (c) ratios are similar, peaking at ~ 40 mJ (8×10^{16} W/cm ²), which can be explained by the fact that the Li-like ionization threshold (97 eV) is much lower than the similar He-like (552 eV) and H-like (667 eV) thresholds.	140

5.19	Plot showing that the ratio of 1s-2p to 1s-3p H-like nitrogen emission remains constant as a function of gas valve temperature for three different mean target densities, indicating that no amplification is taking place. These two H-like nitrogen emission lines are components of the signal shown in Figure 5.20(a).	143
5.20	Trends in H-like (a) and He-like (b) nitrogen EUV emission as a function of gas valve temperature for three target density/ laser energy pairs. The intensities displayed are the sum of all emission lines within each species labeled in Figure 5.14. The sharp drop in H-like and He-like emission intensity as the temperature drops below -160° Celsius corresponds to the onset of droplet formation. The H-like to He-like nitrogen EUV emission ratio (c) is relatively stable as a function of temperature, with the exception of a sharp jump as the temperature drops below -90° Celsius, when the mean cluster radius increases from 30 to 100 nm (Figure 5.10).	145
5.21	Electron densities measured using transverse interferometry for the experimental parameters used in Figures 5.20 and 5.19. At lower temperatures, the mass output of the gas valve was unstable as a function of backing pressure and difficult to control precisely.	146
5.22	Detail of a raw spectrum from Figure 5.14 showing the He-like and H-like series recombination continuum edges from which the electron temperature could be estimated.	151
5.23	Plots of the simulated ion species populations as a function of time when 20 nm (a) and 100 nm (b) radius nitrogen clusters were irradiated with a 36 fs FWHM Ti:sapphire laser pulse with a peak intensity of 6.25×10^{17} W/cm ² . Maximum average ionization $\langle Z \rangle_{avg}$ occurs at $t = 105$ fs and 225 fs for the 20 and 100 nm clusters, which are 30% and 69% fully stripped at those times, respectively.	153
5.24	Simulation results showing the absolute (a) and relative (b) ionization fraction of the ensemble of nitrogen atoms within 20, 40, 60, 80 and 100 nm radius nitrogen clusters irradiated with a 36 fs FWHM Ti:sapphire laser pulse with a peak intensity of 6.25×10^{17} W/cm ² . Plot (b) is the ratio of the two lines plotted in (a). The relative ratio of EUV emission from H-like and He-like ion species should follow the trend in (b), ignoring any collisional re-excitation events after recombination has occurred.	154
5.25	Results for a simulation of the irradiation of a 20 nm radius nitrogen cluster with a 36 fs FWHM Ti:sapphire laser pulse with a peak intensity of 6.25×10^{17} W/cm ² showing the average thermal (a – c) and kinetic (d – f) energy per particle as a function of time for electrons (a, d), ions (b, e) and in total (c, f). Initially, the deposited laser energy is primarily in electron thermal motion (a), but as the cluster expands the energy is transferred almost entirely to radial ion kinetic energy (e). The clusters merge into a uniform plasma after < 5 ps, at which time the ion kinetic energy re-thermalizes.	158

A.1	Topology of the vacuum system used to run experiments with the 25 TW Ti:sapphire laser.	167
B.1	Optical schematic of the flat-field spectrometer (<i>a</i>) and the focal planes of the 1200 (<i>b</i>) and 2400 (<i>c</i>) line/mm gratings as a function of incidence angle. Reproduced from Reference [156].	171
B.2	Schematic of the vacuum enclosure for the flat-field spectrometer. . .	174

Chapter 1

Introduction to laser-cluster interactions

The interaction between light and matter is one of the most basic and important issues in physics. The invention of the laser in the early 1960's [1] enabled the production of light with levels of brightness and coherence that were previously impossible, resulting in the birth of the field of nonlinear optics. It has since found applications in almost every aspect of modern life, including communications, entertainment, industrial manufacturing, metrology, and medicine. As the laser has evolved into a tool capable of high average power ($> 10^5$ W) [2], ultrahigh intensities ($> 10^{22}$ W/cm²) [3] and generating ultrashort pulses (< 5 fs) [4] it has remained a driver of cutting edge scientific research, capable of stimulating extreme nonlinear responses in molecular, ionic and nuclear systems [5] and enabling the direct observation of ultrafast atomic dynamics.

1.1 Pulsed lasers and intensity regimes

The first lasers were capable of kilowatt level peak power outputs and focused peak intensities on the order of gigawatts per square centimeter (10^9 W/cm²) [6]. Modern continuous wave (CW) lasers are capable of megawatt order average powers with peak intensities $\sim 10^{12}$ W/cm² [2]. Although these high average power CW systems are required for some applications such as industrial welding, cutting, and

military weaponry, the linear relationship between CW intensity and average power output imposes a fundamental limitation on intensity by the electrical or chemical input energy available. This makes them unattractive and inefficient for applications that require high peak intensities but are indifferent to average power. For comparison, the output of a nuclear power plant is ~ 1 gigawatt, and the current rate of electrical power consumption on earth is ~ 15 terawatts.

The use of pulsed lasers breaks this limitation, decoupling the average and peak power output of a system by allowing optical energy to be squeezed into short, high-intensity bursts instead of being spread evenly in time over a continuous wave. Improvements in pulsed laser systems have allowed the maximum attainable peak intensity to be raised by more than 10 orders of magnitude in the last 50 years. Q-switched [7] and mode-locked [8] lasers allowed the creation of nanosecond and picosecond pulses, respectively, and chirped pulse amplification (CPA) [9], raised the attainable intensities of femtosecond pulses by several more orders of magnitude.

This has enabled basic research and the development of applications in previously inaccessible regimes of light-matter interaction, the so-called *strong field* or *high intensity* regime ($\geq 10^{13}$ W/cm²) [10] and the *relativistic* or *ultra-high intensity* regime ($\geq 10^{18}$ W/cm²) [11].

Direct field ionization of an atom in the high intensity regime can occur through one of three mechanisms, determined by the relative strength of the laser and Coulomb potential. As the laser intensity first reaches the high intensity regime, high-order multiphoton ionization [12] can occur (Figure 1.1(a)). This occurs when N photons of wavelength ω are absorbed by a bound electron simultaneously, provid-

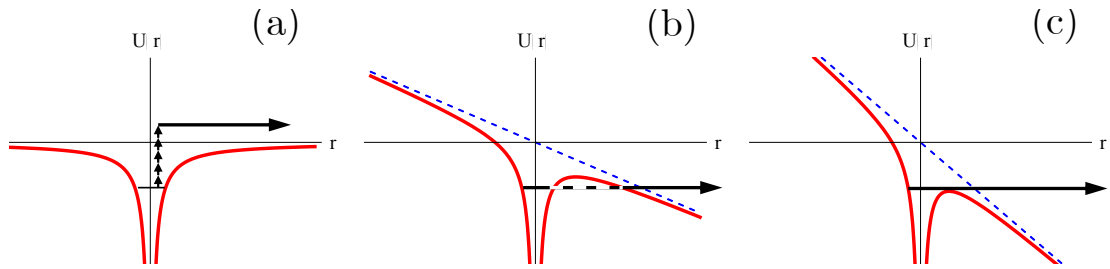


Figure 1.1: Mechanisms by which an electron within an atom can undergo field ionization by a laser. Multiphoton ionization (*a*) occurs when multiple photons strike the atom simultaneously, providing sufficient intensity to escape the Coulomb potential (solid red line). Tunnel ionization (*b*) occurs when the instantaneous laser potential (dashed blue line) is sufficient to modify the Coulomb potential and allow tunneling through the barrier on the timescale of a laser field oscillation. Over-the-barrier ionization (*c*) occurs when the laser field causes a large enough modification to the Coulomb potential that the electron can ‘fall out’.

ing sufficient energy $E_0 = N\hbar\omega$ to liberate an electron from the Coulomb potential of the atomic nucleus. As the laser field intensity is increased further, the potential comprised of the instantaneous sum of the oscillating field and Coulomb potential can allow a bound electron to ‘tunnel’ through the potential barrier [12] (Figure 1.1(b)). In even larger fields, the potential barrier can be suppressed enough that an electron can simply ‘fall out’ of the potential (over-the-barrier ionization) [12] (Figure 1.1(c)). These interactions have been used to generate bright, tabletop EUV sources via high-order harmonic generation [13] and used for applications such as microscopy [14], protein crystallography [15], probing dense plasmas [16] and lithography [17].

Once the reduced vector potential $a_0 = \frac{eE}{m_e\omega} \frac{1}{c}$ is greater than 0.1, the laser-*plasma* interaction becomes relativistically nonlinear. For a laser wavelength of $\lambda = 800$ nm, this corresponds to an intensity $I_0 > 2 \times 10^{16}$ W/cm². Electrons quivering in the laser field can oscillate close to the speed of light, relativistically increasing in mass and oscillating with modified trajectories, leading to corrections in the plasma index of refraction [18]. Additionally, pressure from the ponderomotive force can exceed gigabars [19] and drive highly nonlinear plasma waves [18]. At these intensities applications such as plasma-wave driven tabletop particle accelerators [20], inertial confinement fusion [21] and hard x-ray sources [22] become possible.

1.2 Nonlinear laser-matter interaction

The intense pulses produced by modern lasers can exhibit a wide range of nonlinear effects as they interact with matter. The type and strength of the nonlinearity depends primarily on the laser parameters (intensity, pulsewidth and wavelength) and atom density of the target. Changing any one of these four parameters can change which nonlinear effect is dominant; the specifics of all parameters must be carefully considered in each experimental scenario to make an estimate of the nonlinear dynamics that will occur.

In practice, intense laser-matter interactions usually take place in gaseous targets [23] (jets or static cells) at atomic densities $< 10^{19}$ atoms/cm³ or on the surface of bulk solids [24] at $\sim 10^{23}$ atoms/cm³ within a vacuum chamber, to stop ionization-induced defocusing from preventing the laser from reaching the highest focused intensities. More recently, mass-limited targets such as thin foils [25], nanostructured surfaces on bulk solids [26] and cluster/droplet jets [27] have been used as well. This dissertation is primarily focused on nonlinear ionization processes in jets of atomic clusters and how they can be harnessed to generate extreme ultraviolet light (EUV, approximately 1 – 100 nm wavelength) and modulated plasma waveguides. However, to understand the benefits of clusters as a target medium, it is helpful to first consider the dominant processes by which gaseous and bulk solid targets undergo ionization.

1.2.1 Ionization of gases

When a high intensity laser pulse irradiates a gaseous target, the ionization process is usually dominated by the isolated response of each atom or molecule to the field through multiphoton ionization, tunnel ionization or above threshold ionization, depending on the laser intensity and ionization potential. The ionization process in a gas is usually quite inefficient, resulting in little laser energy deposition ($< 5\%$) [28] and plasmas with an electron temperature of < 50 eV [28], incapable of producing high energy x-ray photons.

Electron-ion collisional ionization can also occur after field ionization has created a population of free electrons. This mostly occurs during the laser pulse, while free electrons are quivering in the laser field. Additionally, elastic electron-ion collisions can thermalize the momentum of electrons quivering in the laser field, resulting in energy transfer from the laser and efficiently heating the plasma after ionization has occurred. However, very little collisional ionization or heating usually occurs [28], because at the gas densities present in most jets ($\leq 10^{19}$ atoms/cm³), the electron-ion collision rates are small compared to the pulsewidths of most lasers with sufficient intensity to cause initial field ionization (≤ 1 ps). These low collisional ionization rates can be beneficial in applications such as high harmonic generation [13] where high intensities are required but collisional ionization is undesirable, but when dense, deeply ionized plasmas are needed for applications such as in plasma waveguide generation [29], they can be problematic.

1.2.2 Ionization of solids

In contrast with gases, the high local atomic densities present in bulk solids ($\sim 10^{23}$ atoms/cm³) facilitate high electron-ion collision rates, resulting in a laser-matter interaction that is almost always dominated by collisional processes [28]. This leads to much more efficient ionization and heating than is possible in low-density gas targets, but rapid conductive cooling by the adjacent bulk material can prevent the creation of the extremely hot ($> \text{keV}$), deeply ionized plasmas required for many applications [30].

Unfortunately, the high densities that allow solids to efficiently absorb laser energy also impose extremely demanding temporal contrast requirements upon the laser, requiring a prepulse to main pulse intensity ratio of better than 10^{-10} on a nanosecond timescale for the most intense petawatt-class systems [31]. Otherwise a prepulse with peak intensity as low as 10^{12} W/cm² can be efficiently absorbed by the surface of the solid, creating a low-density sheath of plasma that can reflect and absorb the main pulse of the laser, preventing it from interacting through collisional processes with a solid-density plasma [31].

The nanosecond-scale prepulses that are the source of this issue can be caused by amplified spontaneous emission (ASE) from amplifiers throughout the laser amplifier chain or by leakage through polarization-based fast electro-optical switches [31]. They can be eliminated by using laser systems without regenerative amplifiers (which emit a more intense nanosecond plateau of ASE than multipass amplifiers) and a combination of techniques such as plasma mirrors [32] and cross-

polarized wave (XPW) filters [33]. These methods can prevent the formation of preplasmas, but increase the complexity and cost of the laser system while reducing the overall efficiency.

Target damage and ejected debris are also problems resulting from the use of bulk solids as laser targets. Compared to gases, laser-solid interactions throw off a large amount of material that can coat surfaces within the vacuum in which it takes place, including laser optics, severely reducing their lifetime and efficiency. They are also usually not renewable, resulting in single-shot experiments or requiring a rastered target. As a result, experiments and applications using bulk solid targets can be more time-consuming and expensive than those using gaseous targets.

However, conductive cooling of the newly formed plasma by the bulk material is by far the most restrictive problem associated with solid targets for most applications, as it puts a ceiling on the electron temperature and limits the energy density of the interaction. This issue can be circumvented by using mass-limited solid targets in a number of configurations, including thin foils [25], nanostructured surfaces on bulk solids [26], and jets of clusters or droplets [27]. These methods retain the high local atomic densities present in bulk solids that enable high collision rates, but limit conductive cooling of the plasma by reducing the spatial degrees of freedom through which it can occur. However, thin foils and nanostructured solids can be difficult to prepare and still eject a large amount of debris. They must also be rastered to expose an undamaged section of the surface, unlike jets of clusters or droplets, which are renewed with each subsequent puff. The interaction between intense laser pulses and jets of clusters is a topic rich in physics and applications

and are the focus of this dissertation.

1.3 Van der Waals aggregate formation

1.3.1 Cluster formation

When high-pressure gas (> 50 PSI) is expelled into vacuum through the nozzle of a solenoid-actuated valve, the random thermal momentum of atoms or molecules becomes kinetically directed as it adiabatically expands, so cooling occurs. In cases where the initial thermodynamic state of the pre-expansion gas is such that expansion along an isentrope brings it to the gas-liquid phase transition, condensation can occur. After the vapor pressure curve is crossed, interparticle attractions due to the van der Waals forces are able to overcome the reduced thermal momentum of the cooled gas, forming nanometer scale solid-density aggregates henceforth referred to as ‘clusters’. This process was first observed when jets containing clusters of 2 to 10^4 atoms were created more than 60 years ago [34]. Jets of clusters can be thought of as a hybrid medium, with low average densities similar to those usually found in gases ($\leq 10^{19}$ atoms/cm³) and the high local densities of solids ($\sim 10^{23}$ atoms/cm³) [35].

Qualitatively, the cluster formation process occurs more efficiently when the pre-expansion gas is held at colder temperatures and higher pressures, bringing the gas closer to the vapor pressure curve [36]. Nozzle geometry and gas species are also important; increasing the cross-sectional area of the nozzle adjacent to the gas reservoir (henceforth referred to as the ‘orifice’, detailed in Figure 1.2) leads to more efficient cluster formation [36], as does the use of gases with larger polarizabilities [36]

Table 1.1: Examples of condensation constants for gases commonly used in the creation of laser-produced plasmas [37].

Gas species	He	D ₂	H ₂	Ne	N ₂	Ar	Kr	Xe
Condensation constant k	3.85	181	184	185	528	1650	2890	5500

(in atomic or molecular gases) or larger permanent dipole moments (only possible in molecular gases) because interparticle dipole attractions are the basis of the van der Waals force. The resulting mean cluster diameter within the jet depends on this combination of parameters, and can range from a few Å at the onset of cluster formation to ~ 1000 Å, when the pre-expansion gas liquefies in the valve and droplet formation occurs, resulting in different dynamics that will be described shortly.

The cluster formation process is not sufficiently well understood from a purely theoretical standpoint to allow prediction from first principles of the size distribution within a cluster jet given only the nozzle geometry and thermodynamic state of the pre-expansion gas [38]. However, the scaling and relative strength the clustering process has been empirically quantified, first by Hagena [39], who introduced the dimensionless parameter:

$$\Gamma^* = k \frac{d^{0.85} p_0}{T_0^{2.29}} \quad (1.1)$$

where Γ^* is the Hagena parameter, T_0 is the pre-expansion gas temperature (K), p_0 is the gas valve backing pressure (mbar), d is the diameter of the nozzle orifice for sonic nozzles (μm) and k is a constant that quantifies the relative strength of the condensation process for different gases. Some examples of condensation constants

with these units for gases commonly used in the creation of laser-produced plasmas are shown in Table 1.1. Conical nozzles are known to aid the clustering process, and this effect is described by replacing the throat diameter d in the Hagen parameter with an equivalent diameter $d_{eq} = 0.74d/\tan(\alpha)$ [39], where d is the orifice diameter of the conical nozzle and α is the half angle at which the nozzle expands (Figure 1.2).

The Hagen parameter is related to the mean number of atoms per cluster $\langle n_{cluster} \rangle$ via the expression:

$$\langle n_{cluster} \rangle = 33 \left(\frac{\Gamma^*}{1000} \right)^{2.35} \quad (1.2)$$

A number of techniques have been used to experimentally verify this scaling for Hagen parameter values spanning $10^2 < \Gamma^* < 10^6$ [40, 41], which corresponds to the onset of cluster formation through the generation of clusters containing up to $\sim 10^7$ particles [42].

1.3.2 Cluster characterization

The limitations imposed by diffraction make it impossible to directly image the size distribution within a jet of nanoscale clusters using the visible or infrared frequencies at which most lasers operate. However, a variety of indirect experimental techniques have been successfully used to measure the scaling of Γ^* and $\langle n_{cluster} \rangle$ with temperature, pressure, gas species and nozzle parameters. These methods include Rayleigh scattering [37, 42] or Mie scattering (for large clusters) [43] in conjunction with neutral gas density measurements, Rayleigh scattering or absorption of

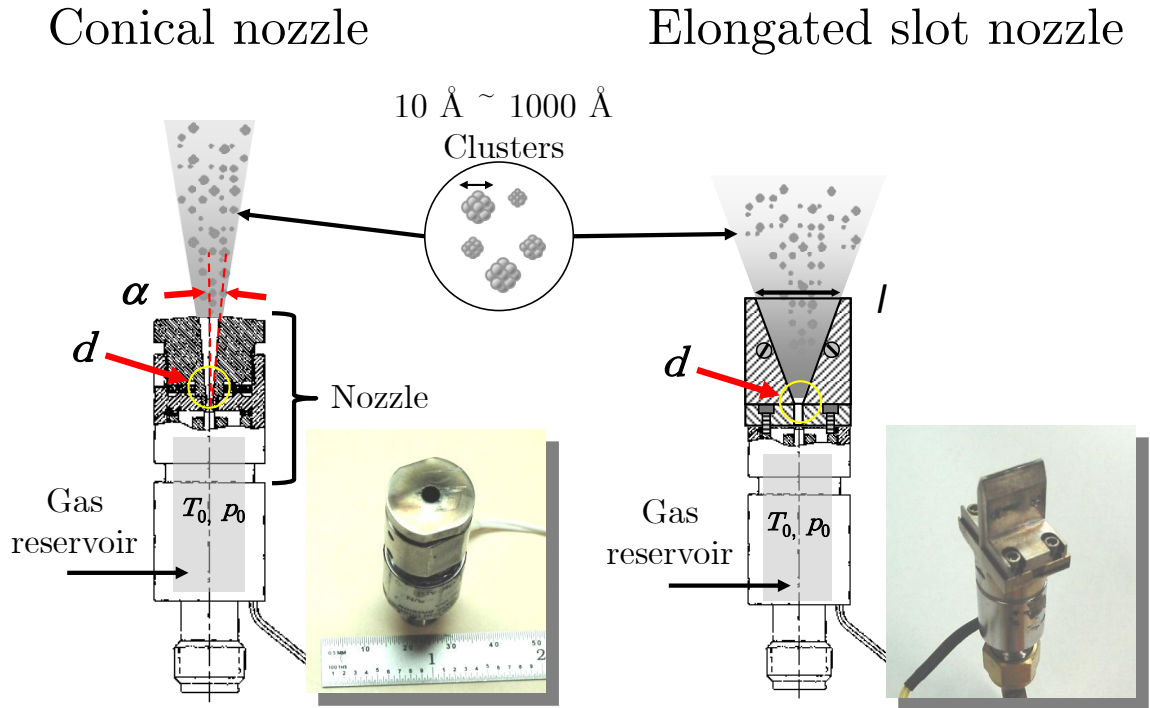


Figure 1.2: Representations and photographs of the gas valve nozzle configurations used in these experiments. The nozzles were attached to commercial gas valves sealed with copper gaskets (Parker Hannifin, General Valve Division series 99). Two conical nozzle configurations were used, with a throat diameter d of 0.5 or 1 mm and an expansion half-angle α of 10° or 5° , respectively. Elongated nozzles with an orifice diameter d ranging from 0.5 to 1 mm and an exit length l of 15 mm were used.

EUV [44], time-of-flight mass spectroscopy (TOF-MS) of ions from Coulomb exploding laser-irradiated clusters [45], diffraction of high-energy electrons [41, 46], atom scattering [47] and fluorescence spectroscopy of small clusters [48]. More recently, the percentage of condensed mass within a cluster jet was measured by observing the time-dependent index of refraction of laser-irradiated exploding clusters [49]. A measurement of the mean cluster size within the jet produced by the solenoid valves used in this experiment was performed using the Rayleigh scattering technique in conjunction with clustered gas interferograms [42]. This will be described in detail in Chapter 2 (Experimental apparatus).

1.3.3 Droplet formation

Jets of droplets are formed when liquid instead of gas is ejected from a solenoid valve into vacuum. While clusters and droplets are both van der Waals bonded aggregates of near solid density, the difference between them lies in the dynamics by which they are formed. Clusters are formed when a gas cools and condenses after ejection into vacuum, while droplets are formed as a stream of liquid undergoes fragmentation. In practice, clusters can be anywhere from a few Angstroms to 25 nm in diameter, while droplets are almost always $> 1 \mu\text{m}$ [50]. The detailed behavior of this fragmentation can be described by the Weber number We [51], an expression of the ratio of kinetic energy of the liquid being ejected from an orifice to the potential energy of its surface tension, expressed as:

$$We = v^2 \frac{d\rho}{\sigma} \quad (1.3)$$

where v is the velocity of the liquid flow as it leaves the nozzle (m/s), d is the diameter of the nozzle orifice (m), ρ is the density of the liquid (kg/m³) and σ is the surface tension (N/m).

In all cases where droplets are encountered in this experiment, the jet is in what is known as the *atomization regime*, when the Weber number is $\geq 10^5$ [52]. This is known because our setup is similar to one used by our group in the past that was characterized in detail [50]. There are several other breakup regimes encountered in lower Weber number droplet jets [52], but they are beyond the scope of this dissertation. This regime is characterized by the immediate breakup of the liquid stream into a jet of droplets much smaller than the nozzle diameter as it leaves the nozzle. However, the aggregate sizes in atomized jets of droplets are still much larger than those that can be produced in cluster jets, with a mean diameter $> 1\mu\text{m}$.

1.4 Laser-cluster interaction models

Cluster jets first drew attention as a mass-limited target medium for intense lasers almost 20 years ago, when McPherson *et al.* irradiated krypton clusters with short (< 1 ps) high intensity (10^{16} to 10^{18} W/cm²) laser pulses and observed anomalous emission of x-rays with photon energies higher than predicted by multiphoton or tunneling gas ionization theory [53]. The authors attributed this emission to high ion charge states arising due to collisions with Z coherently driven electrons, behaving as a single quasiparticle with charge Ze and mass Zm_e , where e and m_e are the charge and mass of an electron, respectively. This model predicts multiple

ionization of inner shell electrons while the outer shells are still occupied. Although there has been much debate about this ‘coherent electron motion model’ [54] in the literature, these experiments brought clusters to the attention of the high intensity physics community.

Since these initial studies there has been a large body of experimental, theoretical and computational research investigating intense laser-cluster interactions. Experiments have shown that irradiating clusters containing up to 10^7 particles with intensities of 10^{13} to 10^{19} W/cm² results in strong absorption ($> 95\%$) [55], hot electrons with $>$ keV energies [56], bright x-rays [27, 55, 57], ions with $>$ MeV kinetic energies [58, 59], neutrons [60] and can allow control of beam propagation [61]. These are properties usually associated with the high energy density plasmas created in laser-solid interactions, indicating that the locally high densities found within individual clusters ($\sim 10^{23}$ particles/cm³) allow them to behave as an ensemble of mass-limited solid targets.

These clusters explode on an extremely rapid timescale of order 100 – 400 fs, depending on the size [28, 62, 63], similar to the pulsewidth of the intense lasers typically used to drive these interactions. Therefore, the details of how the laser couples to the cluster crucially depends upon the time-dependent density and temperature of the plasma, requiring a detailed understanding of the cluster explosion dynamics. The expansion of these clusters is driven by a combination of two mechanisms; hydrodynamic expansion via hot electron pressure and electrostatic repulsion between ions that can occur as electrons escape the neighborhood of the cluster, leading to a buildup of positive charge. Understanding how the relative importance of these two

mechanisms is affected by the laser intensity, laser pulsewidth and cluster size is critical for optimization of the interaction for applications such as nuclear fusion [60], high harmonic generation [13] and x-ray sources [27, 55, 57] for lithography [17] and microscopy [14].

Theoretical approaches investigating the detailed underlying dynamics of the laser-cluster interaction in the high-intensity ($> 10^{13}$ W/cm²), large cluster ($N > 10^2$ particles) regime can be divided into two categories — rate equation models that use averaged global variables, treating the particles as a fluid [28, 62] and classical molecular dynamics (MD)/ Particle-in-cell (PIC) models that treat particles individually [64–69]. The range of applicability of each particular calculation depends on the details of the model used, but roughly speaking, fluid models are valid with larger clusters ($N > 10^4$ particles) and lower intensities ($< 10^{16}$ W/cm²) when the explosion of a cluster plasma is primarily driven by hydrodynamic forces, and MD simulations are required when more intense lasers ($> 10^{16}$ W/cm²) irradiate smaller clusters ($N < 10^5$ particles), resulting in expansion driven primarily by interionic Coulomb repulsion [58, 59].

1.4.1 Nanoplasma model

The first hydrodynamic model of how cluster plasmas undergo ionization and expansion when irradiated by short (< 1 ps) intense ($> 10^{14}$ W/cm²) laser pulses was the ‘nanoplasma’ model developed by Ditmire *et al.* [28]. The results of simulations using this model [28] indicated that initial ionization of the cluster takes place in

the far leading edge of the laser pulse via multiphoton or optical field ionization, followed by a rapid avalanche of electron-ion collisional ionization enabled by the locally solid densities found in clusters.

This model assumes that as the cluster expands, the radial plasma density profile remains uniform. This assumption results in each cluster responding to the laser field as a uniform dielectric sphere, given by:

$$\mathbf{p} = \gamma \mathbf{E} = a^3 \left(\frac{\varepsilon - 1}{\varepsilon + 2} \right) \mathbf{E}, \quad (1.4)$$

where \mathbf{p} is the dipole moment induced in the cluster, γ is the polarizability, \mathbf{E} is the electric field of the laser, a is the cluster radius and $\varepsilon(\omega)$ is the complex dielectric function, which for a plasma is given by

$$\varepsilon(\omega) = 1 - \frac{1}{1 + i \frac{\nu}{\omega}} \frac{N_e}{N_{cr}} = 1 - \xi \left(1 - i \frac{\nu}{\omega} \right), \quad (1.5)$$

where ν is the electron-ion collision frequency, ω is the laser frequency and

$$\xi = \frac{1}{1 + \frac{\nu^2}{\omega^2}} \frac{N_e}{N_{cr}}. \quad (1.6)$$

Here N_e is the electron density, the critical density $N_{cr} = m_e \omega^2 / 4\pi e^2$, m_e is the electron mass and e is the electron charge. Once the cluster has expanded enough that the electron density N_e drops to $\sim 3 \cdot N_{cr}$, a resonant enhancement of the laser field occurs within the entire volume of the cluster because $\varepsilon + 2 = 0$. The spherical geometry of the cluster is the physical reason that this prediction differs from the $N_e = N_{cr}$ resonance typically found in a bulk plasma. The predicted duration of this resonance is

$$\delta t_{res} \approx \frac{2\nu}{3\omega} \left(\frac{N_{e0}}{3N_{cr}} \right)^{\frac{1}{3}} \frac{a_0}{c_s} \quad (1.7)$$

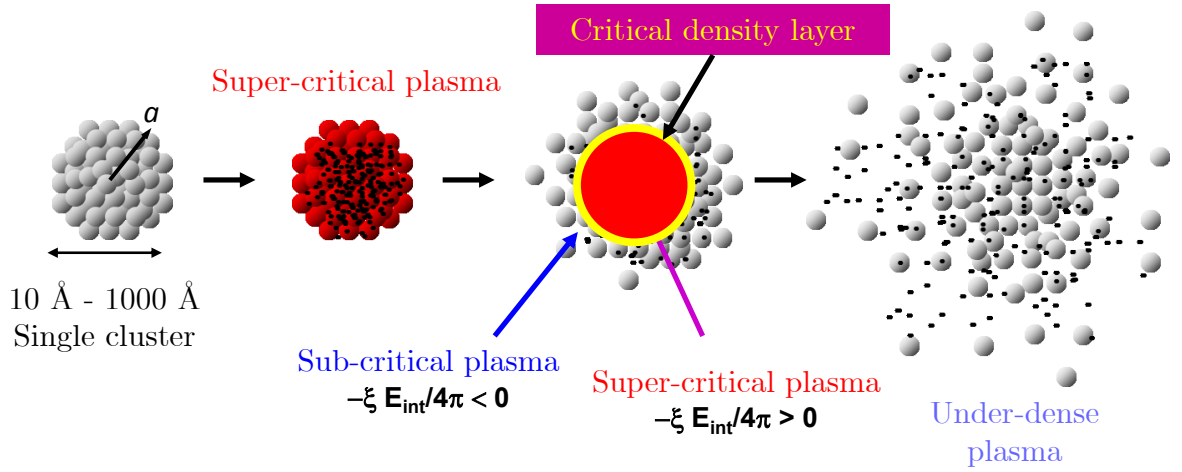


Figure 1.3: Schematic representation of the 1D nanoplasma expansion model of Milchberg *et al.* [62]. The initial state of the neutral cluster is shown at the far left. Initial ionization by an intense laser pulse creates a dense, super-critical plasma that expands layer-by-layer, resonantly coupling to the plasma in the region with resonant density $-\xi E_{int}/4\pi$, where E is the electric field in the cluster and $\xi = (1 + \nu^2/\omega^2)^{-1} N_e/N_{cr}$.

where a_0 is the initial cluster radius, c_s is the speed of sound and N_{e0} is the initial electron density [62]. For the clusters with initial radii a_0 from 10 – 60 nm this model predicts δt_{res} values from 6 – 40 fs, in disagreement with experimentally observed resonant durations of hundreds of femtoseconds [63].

In an effort to achieve a more accurate quantitative understanding of the hydrodynamic laser-cluster interaction, Milchberg *et al.* [62] developed a model that relaxes the assumption of uniform expansion by using a one-dimensional (1D) hydrodynamic laser-cluster interaction model. As was the case with the uniform density

model of Ditmire *et al.* [28], this code self-consistently models the interaction of a single cluster with a laser field in the near-field limit, requiring $ka \ll 1$, where k is the wavenumber of the laser and a is the radius of the cluster.

This model provided additional physical insight to the cluster explosion process and improved the quantitative agreement between theory and experiment. Whereas the uniform density model predicts brief δt_{res} resonant enhancement of the laser field once a nanosphere of uniform density has expanded sufficiently to drop the electron density N_e to $\sim 3 \cdot N_{cr}$, the 1D model predicts that the cluster nonuniformly expands ‘layer-by-layer’, with resonant coupling occurring in a critical density region where $N_e = N_{cr} = m_e \omega^2 / 4\pi e^2$ that decreases in radius as the cluster expands (Figure 1.3). Thus the 1D model predicts longer-lived resonant coupling that persists until the critical density layer has receded to the core and the entire cluster is of subcritical density. Depending on the initial size of the cluster this expansion time τ_{cr} is usually 100 – 400 fs [63]. The expansion timescales of this model were later experimentally verified [63], and it was shown that coupling between the laser pulse and plasma is more efficient when the pulsewidth of the laser is matched to this critical cluster expansion time [63].

While these hydrodynamic models have been critical to the development of a physical understanding of laser-cluster coupling dynamics, treating the ensemble of electrons as a fluid neglects the escape of hot laser-heated electrons from the neighborhood of the cluster. When this occurs, a buildup of positive charge drives expansion via electrostatic repulsion between ions. In extreme cases this can lead to a Coulomb explosion in which the majority of the electrons have been removed

from the cluster before any hydrodynamic expansion has a chance to take place, and Coulomb repulsion between the ions violently drives them apart. This process can result in ions with $> \text{MeV}$ kinetic energies [59]. Milchberg *et al.* calculated that the explosion of argon clusters with radii larger than 25 \AA is dominated by hydrodynamic pressure until the intensity exceeds 10^{15} W/cm^2 [62]. To investigate the dynamics of exploding clusters in regimes where electrostatic forces are important, particle-based models must be used.

1.4.2 Particle models

The first particle-based simulations of laser-irradiated clusters were molecular dynamics (MD) simulations using a classical Monte Carlo method performed by Rose-Petruck *et al.* [64], but computational limitations prevented them from studying systems of more than 55 atoms. Based on these results, they proposed the ‘ionization ignition’ model of the laser cluster interaction, which theorized that a combination of the laser field and DC Coulomb fields from inertially confined ions were responsible for the deep charge states and absorption properties of clusters [64, 70]. Simulations that explicitly treated particle-particle electric forces were done soon afterwards [65, 66], but a computational cost that scales $\propto N_p^2$ limited these simulations to clusters containing less than 60 atoms.

Since these initial studies, there has been a large body of work using particle-based models to study the laser-cluster interaction, including classical MD simulations with full interparticle treatment similar to the initial studies [64–66], MD

models implementing a fast-tree algorithm with a less severe computational scaling $\propto N_p \log N_p$ [71] and 3-dimensional particle-in-cell (PIC) simulations that use a grid to calculate the electric fields that drive particle dynamics [67].

3D PIC simulations by Taguchi *et al.* [68] corroborated the major features of the 1D nonuniform nanoplasma model [62], and verified when expansion due to electrostatic Coulomb repulsion could be neglected. These PIC simulations were appropriate for interactions in the near field limit when $ka \ll 1$ at intensities $< 5 \times 10^{17}$ W/cm², when the trajectories of quivering electrons begin to experience modifications due to relativistic mass corrections and the Lorentz force.

More recently, MD simulations by Last and Jortner [69] applying a fully relativistic electromagnetic treatment have shown that laser pulses with extreme intensities ($I_0 > 10^{20}$ W/cm²) can drive Coulomb explosions in larger clusters ($N_p > 10^8$), resulting in ion kinetic energies in the range of 1 – 10 MeV.

1.5 EUV and x-ray emission from nanoplasmas

The hot, deeply ionized plasmas created by laser-irradiated clusters and droplets are bright sources of x-ray and EUV radiation. For example, strong K alpha emission from argon clusters was observed using laser intensities several orders of magnitude lower than the single-atom OFI threshold [72]. Previous experiments have also studied x-ray and EUV emission from laser-irradiated clusters containing xenon [73], krypton [27, 57], argon [57, 72], neon [28] and nitrogen [74].

These sources can be ultrafast — sub-picosecond x-ray [27, 75, 76] and nanosec-

ond scale EUV pulses [27, 74, 76, 77] from cluster plasmas have been observed by several groups using x-ray streak cameras. This x-ray and EUV emission can occur through several channels over the wide range of plasma temperatures and densities present throughout the process of nanoplasma generation and evolution, including collisional excitation, collisional recombination (3-body), and radiative recombination (2-body).

1.5.1 Collisional excitation and spontaneous decay

One channel through which x-ray or EUV emission that can occur in cluster plasmas is the spontaneous decay that follows collisional excitation of an ion that has already experienced multiple previous collisional ionization events that resulted in a tightly bound valence electron that is vulnerable to excitation but can resist ionization. This process primarily occurs during and immediately following the laser pulse, when electron temperatures (often $> \text{keV}$) and densities ($> 10^{22} \text{ atoms/cm}^3$) are highest. After the departure of the laser pulse, nanoplasma expansion sharply reduces the electron temperature and density, reducing both the electron-ion collision rate and the population of electrons with sufficient kinetic energy to collisionally excite electrons that could emit EUV. These energetic excited states of multiply ionized atoms can have very short lifetimes $< 1 \text{ ps}$, resulting in prompt emission following excitation.

Subpicosecond x-ray emission with photon energies greater than 1 keV has been observed from laser-irradiated krypton [27], xenon [76] and argon clusters [75].

This ultrafast x-ray emission has been attributed to collisional excitation as the near solid-density nanoplasma is heated by the laser pulse, followed by spontaneous emission.

1.5.2 Radiative recombination (2-body)

Radiative recombination occurs when a single free electron encounters an ion and is captured, emitting a photon of energy equal to the potential energy of the newly occupied bound state of the electron plus the kinetic energy of the newly captured electron (Figure 1.4). As the inverse of the photoionization process, radiative recombination has the same electron-ion interaction cross section, which dictates that electrons are preferentially captured directly into the innermost unoccupied energy levels of the ion, which in a deeply ionized plasma can result in the immediate emission of an EUV or x-ray photon. The overall 2-body recombination rate scales $\propto n_e T_e^{-2/3}$, where n_e and T_e are the electron density and temperature, respectively.

1.5.3 Collisional recombination (3-body)

Collisional recombination occurs when two electrons collide with an ion simultaneously, one is captured by the ion and the second departs with the excess kinetic and ionic potential energy released as the first recombined, thereby conserving the energy of the 3-body system without the emission of any photons (Figure 1.4). The 3-body recombination process preferentially captures electrons to outer excited

Recombination pathways- 2-body (Radiative) or 3-body (Collisional)

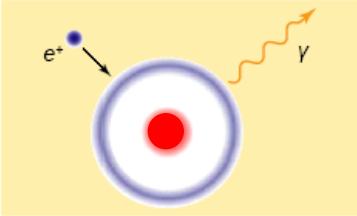
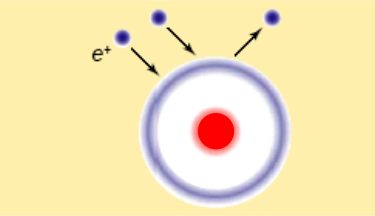
	Radiative Recombination	Three-Body Recombination
Principle		
Temperature depend.	$\propto T^{-2/3}$	$\propto T^{-9/2}$
e ⁻ density dependence	$\propto n_e$	$\propto n_e^2$
Recombines to	Inner shell states	Outer shell states ($\sim n^4$)

Figure 1.4: Radiative (2-body) and collisional (3-body) recombination pathways and scaling with electron temperature and density in a plasma. These processes are the inverse processes of photoionization and collisional ionization, respectively.

states of the ion (with a rate $\propto n^4$, where n is the principal quantum number), which can then decay via spontaneous emission, eventually reaching the ground state. 3-body recombination favors excited states because they occupy a larger fraction of the phase space of possible electron angular momentum configurations, as is the case with the inverse process, electron collisional ionization. If the pre-recombination ion had a sufficiently deep ground state vacancy, this eventually results in the emission of an EUV or x-ray photon. This rate scales $\propto n_e^2 T_e^{-9/2}$, so it is clear that while the 2 and 3 body rates both increase with higher densities and colder temperatures, in dense, cold plasmas 3-body recombination will dominate, but as the density drops and temperature rises the relative importance of the 2-body recombination mechanism increases.

After the individual clusters have dropped below critical density (100 – 400 fs) and merged (1 – 5 ps) to form a uniform plasma column, EUV attributed to recombination has been observed as the uniform column undergoes further expansion and cooling. Experiments in nitrogen clusters observed this EUV emission between 1 and 1.8 nanoseconds using an x-ray streak camera [74]. Other groups have also observed nanosecond-scale pulses of EUV from xenon [76], krypton [27] and nitrogen [77] clusters.

1.6 Dissertation outline

The unifying theme of this dissertation is the use of laser-cluster interactions to facilitate the production of modulated plasma waveguides and EUV from plasmas produced in laser-irradiated clusters. Having introduced the basics of the laser-cluster interaction in Chapter 1, Chapter 2 provides a thorough description of the experimental apparatus, starting with the specifications of our cryogenic cluster source, followed by our 10 gigawatt Nd:YAG system and our 1 and 25 terawatt Ti:sapphire laser systems. The vacuum system in which the interactions take place is described in Appendix A.

Chapter 3 provides background on the generation of preformed plasma waveguides, then Chapter 4 presents the results of experiments in which modulated plasma waveguides were generated using ‘ring gratings’ and a wire obstruction technique. The ring grating technique works by focusing a periodically *modulated beam* on a *uniform*, elongated jet of clusters, resulting in periodic variations in heating that

lead to modulations in diameter. The wire obstruction method works by focusing a *uniform beam* on a target that has been periodically *modulated* by the placement of thin wire ($< 50\mu\text{m}$ diameter) obstructions in the flow of clusters, resulting in clean vacuum gaps in the target.

The Chapter 5 describes experiments in which nitrogen clusters were irradiated with intense ($I_0 > 10^{16}$ W/cm²) femtosecond laser pulses, creating a fully stripped plasma. Emission lines from H-like, He-like and Li-like nitrogen in the 1.5 to 15 nm spectral range were collected using a single-shot flat-field spectrometer (Appendix B). Trends in this emission were investigated as a function of incident laser energy and nitrogen cluster radius. These experiments were originally conceived in an attempt to make a transient x-ray laser [78] on the $2p_{3/2} \rightarrow 1s_{1/2}$ and $2p_{1/2} \rightarrow 1s_{1/2}$ transitions in H-like nitrogen, but no amplification was observed.

Finally, in Chapter 6, the experimental results are briefly summarized and future experiments are discussed.

Chapter 2

Experimental apparatus

2.1 Overview

In this dissertation, a cryogenically cooled solenoid-actuated gas valve creates a jet of clusters within a vacuum chamber to be used as a target for laser-cluster interaction experiments. Different conical or elongated nozzle configurations were used to control the geometry of this target, and changing the temperature and backing pressure of the valve allowed control of the mean cluster size and average atomic density.

Two distinct laser setups were used to perform laser-cluster interaction experiments. In the first, a pair of custom laser systems are used together — in Chapter 4, a 10 gigawatt peak power Nd:YAG (Neodymium doped Yttrium Aluminum Garnet)-based pulsed laser is synchronized with a 1 terawatt peak power Ti:sapphire (Titanium doped Sapphire) system. The Nd:YAG is focused with an axicon to generate a preformed, periodically modulated plasma waveguide in which the Ti:sapphire pulse can be guided. In the second setup, a commercial (Coherent) 25 terawatt peak power Ti:sapphire system is focused upon a jet of nitrogen clusters in vacuum to generate EUV. Details of this experiment can be found in Chapter 5. Additionally, a custom flat-field EUV spectrometer (Appendix B) was constructed to measure light emitted from the nitrogen plasma created by the 25 terawatt laser

in the 1.5 – 20 nm spectral range.

2.2 Cryogenic cluster source

The cluster source used in all experiments presented in this dissertation is capable of making jets of clusters with a mean diameter from 1 – 1000 Å [42] and mean atomic density ranging from 10^{16} – 10^{21} atoms/cm³. This is accomplished by precisely controlling the temperature and backing pressure of the gas reservoir within a solenoid valve that expels a variety of gases into vacuum, including argon, nitrogen, and hydrogen (Figure 2.1). By changing the operating point of the jet in pressure-temperature phase space, the source can also be operated in regimes in which it emits jets of unclustered monomers or a stream of liquid droplets with mean diameter greater than 1 μm [50].

The core of this cluster source is a commercial stainless steel solenoid valve (Parker Hannifin, General Valve Division series 99, Figure 2.2) capable of high pressure cryogenic operation in vacuum. These valves use copper gaskets that are capable of remaining sealed over a broad range of temperatures (–180° to 45° Celsius) while backed at high pressure (up to 1000 PSI). In contrast, valves sealed with elastomers (such as the General Valve Division Series 9) tend to develop leaks below –100° Celsius. Additionally, leaks can result from the deep groove that is eventually worn in the poppet where it seats and seals on the inner surface of the orifice in the valve body, after many hundreds of thousands of opening cycles. To extend the lifetime of the valve, a Kel-F poppet is used instead of the softer Teflon

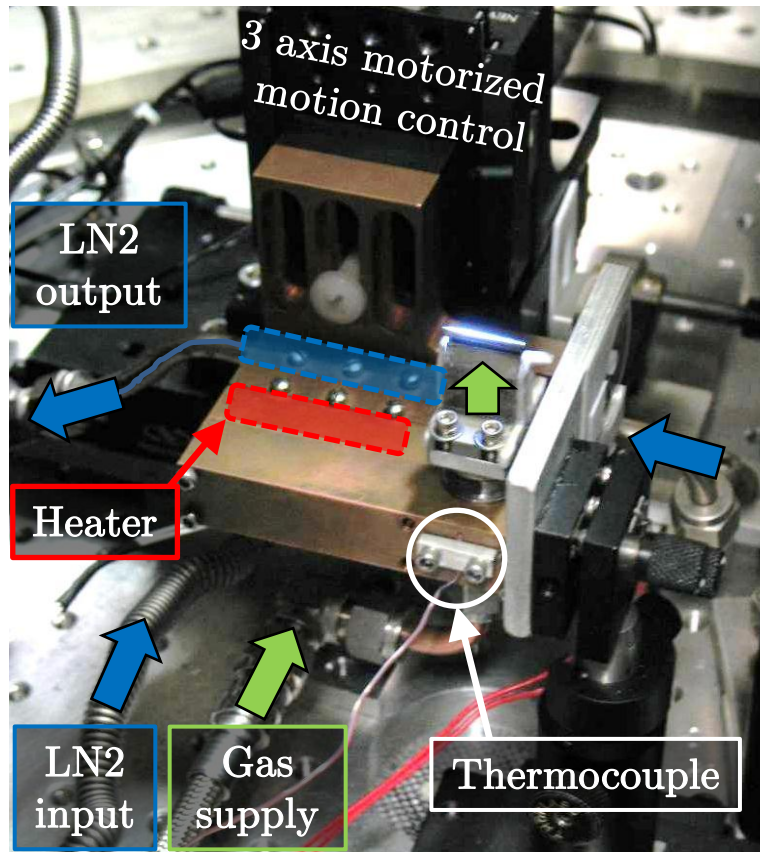


Figure 2.1: Photograph of the cryogenic cluster source used in these experiments, shown with an 15 mm elongated nozzle installed on the solenoid valve and a plasma column created by an axicon-focused Nd:YAG laser pulse.

poppet that is standard. Eliminating leaks from the gas valve reduces the ambient background pressure in the vacuum chamber, which is important for minimizing the re-absorption of EUV generated in the laser-cluster interaction [79] and protecting high voltage components such as photomultiplier tubes.

The solenoid in the valve was driven with a short-pulse high-voltage controller (General Valve IOTA ONE) capable of opening the valve in as little as 200 microseconds. The controller uses a 300 V high-voltage pulse to quickly open the valve, then uses a 28 V holding pulse to keep it open. The pulsewidth and voltage of the opening pulse as well as the voltage of the holding pulse can be modified using jumpers in the IOTA ONE controller. If the background pressure in the chamber becomes too high, the voltage intended for the solenoid can short at the electrical feedthrough in the vacuum chamber, preventing the valve from operating.

Elongated or conical nozzles shape the flow after the gas passes the poppet, optimizing the geometry of the jet for the application at hand. For example, elongated cluster jets are ideal for waveguide formation, and shorter jets were used to study EUV generation from clusters without obfuscation by propagation effects. Additionally, when the gas flow is supersonic, there is a sharp boundary between the jet and vacuum that helps minimize ionization-induced defocusing.

Releasing a jet of clusters with a duration of less than one millisecond from the solenoid valve required careful initial assembly of the valve. If the stroke of the poppet was too large or too short by even a few thousandths of an inch, the valve did not fully open, resulting in sharply reduced mass output and diminished cluster formation. The stroke could be coarsely modified by choosing different copper gasket

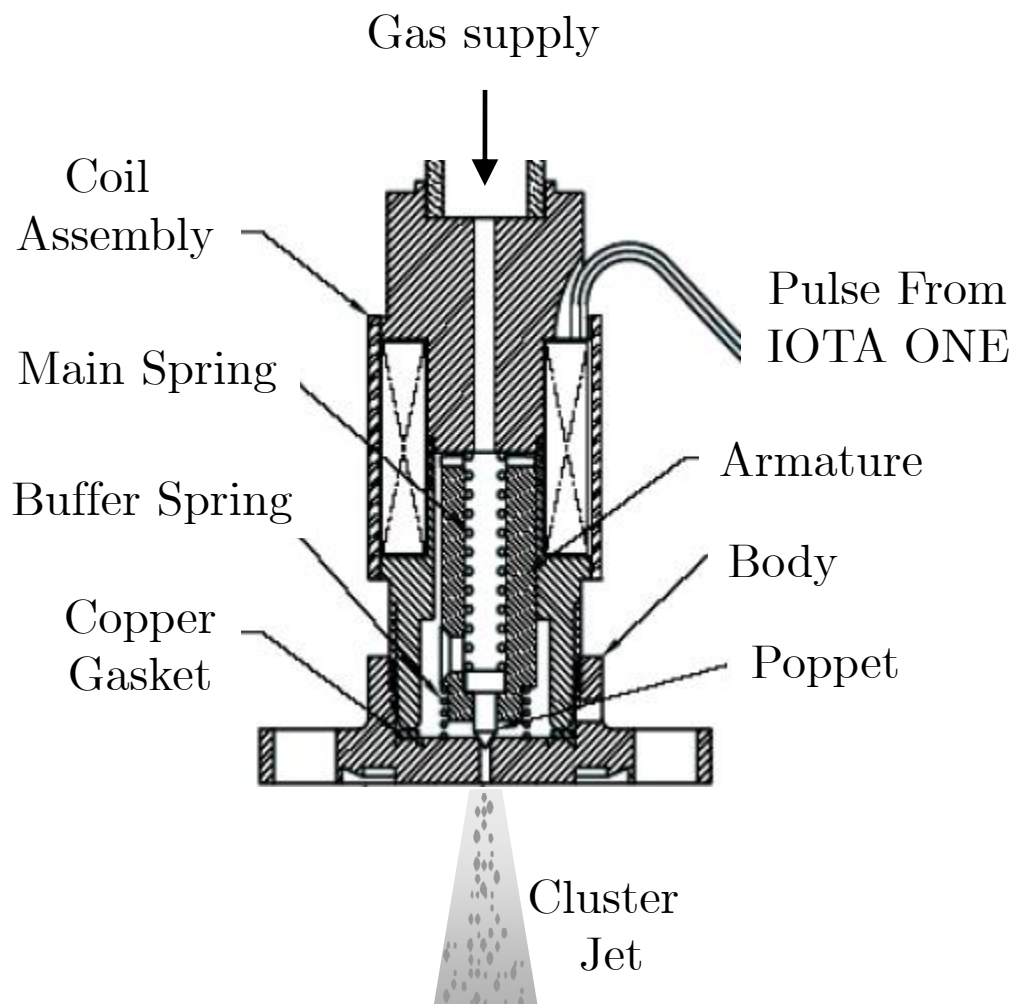


Figure 2.2: Cross-sectional drawing of a Parker Hannifin Corporation, General Valve Division, Series 99 solenoid valve with no nozzle attached.

thicknesses (0.015" – 0.050" available in increments of 0.005") and finely controlled by the amount of compression applied to the gasket by the tightness of the valve coil assembly with respect to the valve body (valve components labeled in Figure 2.2). This allowed the solenoid to apply sufficient force to the armature to be able to quickly overcome the opposing forces of the spring and pressurized gas within the reservoir. In practice, the stroke was optimized by listening to the sound made by the gas jet as the valve body was slowly tightened while operating at 10 Hz in atmosphere and optimal performance was then verified by monitoring the pressure as it was run in vacuum. After the gas jet has been cycled many thousands of times while backed at high pressure, a groove develops in the poppet and it is necessary to re-tighten the valve body, slightly reducing the effective copper gasket thickness to compensate for the lengthening of the armature stroke by the depth of the poppet groove.

The degree of clustering that occurs within the jet of gas expelled from the nozzle was controlled by regulating the pre-expansion pressure and temperature of the gas within the solenoid valve reservoir. Reservoir pressure (50 – 800 PSI) was controlled by simply using a commercial gas regulator. To adjust the temperature, the solenoid valve was mounted in a copper block that also contained a liquid nitrogen line and heating element (Figure 2.1).

The solenoid valve was cryogenically cooled by forcing liquid nitrogen through a stainless steel tube clamped into the same copper block in which the solenoid valve was mounted. The cooling rate was controlled by partially restricting the flow of liquid nitrogen to the copper block with a manually operated plug valve between

the liquid nitrogen Dewar and insulated feedthrough on the vacuum chamber. The liquid nitrogen flow rate could be held stable for many hours by maintaining a constant internal pressure within the Dewar with a gas regulator fed by an external supply of dry nitrogen gas at a chosen pressure between 5 and 8 PSI.

An electric cartridge heater (Omega Engineering CSS-10150, up to 55 watts) was clamped in the copper block adjacent to the liquid nitrogen line, because control of the liquid nitrogen flow rate alone was not sufficient to obtain the desired level of temperature stability. The temperature was monitored by a type T thermocouple in the copper block and digitally displayed by an electronic controller (Omega Engineering CN77324) which switched the heater on or off based upon whether the temperature was below or above the chosen set point (-180° to 45° Celsius). Thus the coil assembly of the solenoid valve was actively temperature-stabilized with $\pm 0.5^{\circ}$ Celsius stability [50] for the duration of experimental runs, in some cases > 8 hours.

To allow control of the cluster jet position with respect to the laser focus, the copper cooling block was mounted on a 3-axis translational positioning stage with encoded, USB-controlled motorized actuators. The copper block was thermally insulated from the translation stage with a Delrin spacer and attached with nylon screws. The liquid nitrogen supply and return as well as the high pressure gas supply were both connected to the cluster source with flexible stainless steel bellows to allow the translation stages freedom of motion.

2.2.1 Cluster source operational procedures

The goal motivating control of the pressure and temperature in the cluster source gas reservoir is independent control of the mean cluster size and mean atomic density in the target. Roughly speaking, for a given gas species the pre-expansion reservoir pressure is the main factor that influences the mean atomic density of the jet and the mean cluster size is primarily determined by the temperature, as can be seen in the Hagen parameter scaling [39].

Nonetheless, the degrees of freedom are coupled — changing the temperature affects the mean jet density as well, and the reservoir pressure also affects the mean cluster size. Although the underlying dynamics of cluster jet formation are extremely complicated, the scaling of the mean cluster diameter is well described by the empirical Hagen parameter discussed in Chapter 1, $\propto T^{-5.38}$ and $\propto P_0^{2.35}$. Additionally, the impedance of the solenoid in the valve changes significantly (from 75Ω to $\sim 25 \Omega$) as it is cooled from room temperature to cryogenic temperatures, affecting how the solenoid responds to a given electrical pulse from the IOTA ONE. To compensate for this modified response, the settings can be changed on the IOTA ONE to reduce the electrical pulsewidth as the jet is cooled, and the relative delay between the laser and IOTA ONE trigger must then be decreased as well.

To scan the cluster size while holding the average atomic density of the jet constant, temperature was used to change the cluster size, and the backing pressure of the jet was then changed to compensate for any changes in mass output. The average atomic density of the jet could be directly monitored by measuring the

phase shift imparted on a probe pulse via neutral gas interferometry. However, the procedure for acquiring and processing interferometric data is time-consuming and disrupts the process of acquiring EUV spectral data.

It was found that the pressure in the vacuum chamber read using a baratron with a digital readout (MKS Instruments Model 626A, 0 – 10 Torr with 0.001 Torr resolution) scales linearly with the mass output of the cluster source. Therefore, by calibrating chamber pressure readings with interferometric measurements of the gas jet density, we were able to use the vacuum chamber pressure to measure neutral gas density. This pressure measurement was the primary means used for determining the cluster jet density during these experiments because the instant digital readout of this pressure measurement was more practical and less time-consuming than the neutral gas measurement.

2.3 10 gigawatt 100 picosecond Nd:YAG laser

The custom Nd:YAG-based laser system used in the experiments in Chapter 4 to create plasma waveguides generates 100 ps pulses containing of up to 800 mJ of energy per pulse at a center wavelength of 1064 nm, at a repetition rate of 10 Hz. This level of energy is achieved by amplifying pulses from a mode-locked Nd:YAG oscillator with three sequential stages of amplification. The first amplification stage is a flashlamp-pumped regenerative amplifier (RGA), followed by a two pass amplifier in a ring configuration (Power Amplifier 1, or ‘PA1’) and then a final single pass amplifier (Power Amplifier 2, or ‘PA2’). This system is described in detail

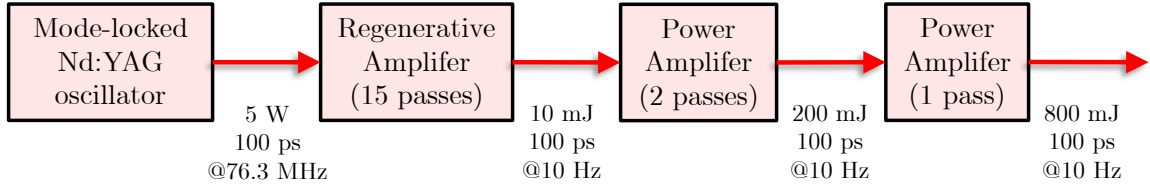


Figure 2.3: The topology of the 1064 nm Nd:YAG laser system used in the plasma waveguide experiments presented in Chapter 4. The oscillator, RGA and both amplifier stages are pumped with flashlamps.

in Chapter 2 of the University of Maryland, College Park Ph.D. Thesis of Tom Clark [80].

The commercial Nd:YAG oscillator (Coherent Antares) is mode-locked with an acousto-optic modulator that produces a train of 100 ps pulses at a rate of 76.3 MHz with an average power of up to 20 watts. However, because a 5 watt pulsetrain is all that is required to seed the RGA, a half-wave plate (HWP) and thin-film polarizer (TFP) are used to attenuate the beam to this level. The pulsetrain is then directed into a pulse slicer composed of a Pockels cell and polarizing beamsplit cube that selects 10 pulses per second by attenuating the majority of the pulses by a factor of $\sim 10^3$. This pulsetrain is reflected into the RGA, which is thus seeded with ~ 50 nJ pulses at a rate of 10 Hz.

The regenerative amplifier (RGA) in this system consists of a flashlamp-pumped Nd:YAG rod in a self-filtering unstable resonator configuration [81]. The seed pulse from the oscillator is coupled into and out of the resonator by a two-step Pockels cell (Thales Medox) and polarizing beamsplit cube, usually requiring ~ 15

round trips to saturate the amplifier. The pulse self-filtered twice on each round trip by a ~ 1 mm diameter aluminum pinhole at the common focus of the two concave cavity mirrors. This amplifies the ~ 50 nJ seed pulses from the oscillator to ~ 10 mJ.

After the amplified pulse is switched out of the RGA, it makes two passes through the first power amplifier (PA1), after which it contains up to ~ 200 mJ. The beam travels through the rod in the same direction on both passes in a ring configuration, which prevents feedback into the RGA. However, the beam clips on the edge of the PA1 rod as it makes the second pass, so a vacuum spatial filter (VSF) is needed to smooth out the beam profile. The VSF consists of a pair of convex lenses on either side of a vacuum tube containing a pinhole with diameter ~ 100 μm positioned at the focus of the first lens. This smooths out the beam profile because the focal mode is the spatial Fourier transform of the input beam profile; variations in the beam profile are contained in the wings of the focal spot, which are blocked by the pinhole [80]. The VSF is necessary prior to passage into PA2, which brings the pulse energy as high as ~ 800 mJ with an intensity close to the threshold for nonlinear self-focusing. Thus nonuniformities in the beam profile could cause nonlinear self-focusing, damaging any optics encountered. After leaving PA2, the beam is relay imaged to a vacuum chamber in which experiments take place.

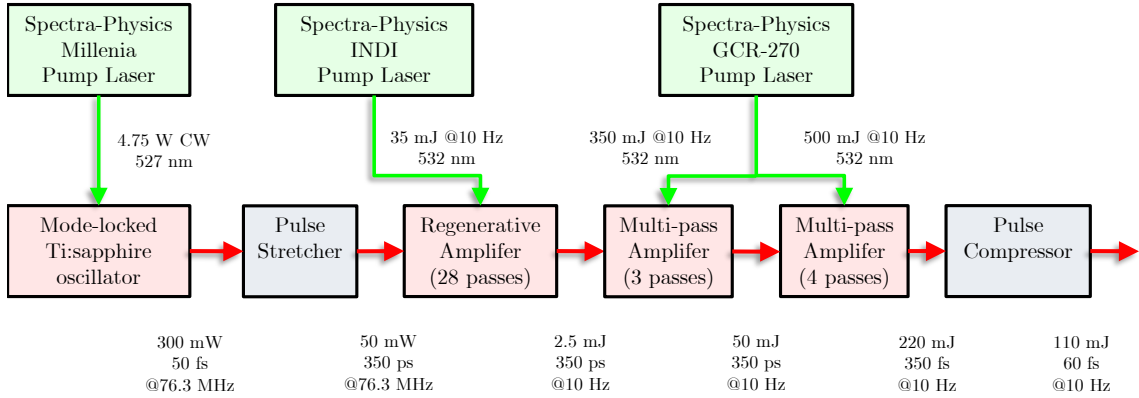


Figure 2.4: The topology of the 2 terawatt peak power 800 nm Ti:sapphire laser system used in the plasma waveguide experiments presented in Chapter 4.

2.4 2 terawatt 60 femtosecond Ti:sapphire laser

To verify the properties of modulated plasma waveguides, a custom Ti:sapphire-based laser system was used. It emits 60 fs pulses at a repetition rate of 10 Hz, capable of up to 100 mJ of energy per pulse at a center wavelength of 800 nm, achieved using the chirped pulse amplification (CPA) technique [82,83] to temporarily reduce the intensity of the pulse while it undergoes amplification by temporally stretching it beforehand and recompressing it to the original pulsewidth afterwards. A detailed description of this laser system can be found in Chapter 3 of the dissertation of Ki-Yong Kim [84].

First, a passively Kerr-lens mode-locked Ti:sapphire oscillator produces a 50 fs pulsetrain with a 76.3 MHz repetition rate and ~ 4 nJ per pulse. The pulsetrain is then stretched into a series of chirped pulses with a width of ~ 300 ps by the pulse stretcher, which uses a single diffraction grating design. 10 pulses per second then

make ~ 28 passes in a regenerative amplifier, increasing the energy to ~ 2.5 mJ. A pair of multi-pass amplifiers then increase the energy of each 2.5 mJ chirped pulse to 50, then 220 mJ. Finally, a dual-grating compressor re-compresses the pulse to nearly the original duration produced by the oscillator, resulting in a 60 fs, 100 mJ, 10 Hz pulsetrain. The phase and frequency of the optical pulsetrain was synchronized to that of the Nd:YAG system described in the previous section using a piezo-driven mirror in the Ti:sapphire oscillator, as described in Appendix H of Reference [84].

2.5 25 terawatt 36 femtosecond Ti:sapphire laser

A commercial (Coherent) Ti:sapphire laser system capable of a 25 terawatt peak power output was used for the EUV generation experiments presented in Chapter 6 (Figure 2.5). This peak power level is attained with 36 fs pulses containing up to 800 mJ of energy, at a center wavelength of 800 nm and a repetition rate of 10 Hz. The first component of this system is a commercial (Coherent Micra) mode-locked Ti:sapphire oscillator that emits out a pulsetrain of < 20 fs, ~ 6 nJ pulses with a 76.3 MHz repetition rate. These pulses are then stretched to ~ 200 ps with a pulse stretcher containing a single grating, then are directed into a commercial (Coherent Legend) regenerative amplifier that generates a 1 kHz pulsetrain with 800 μ J per pulse. A pockels cell then reduces the repetition rate to 10 Hz, and the remaining pulses are amplified by a multipass amplifier to ~ 1150 mJ. Finally, the pulses are temporally compressed to a 36 fs pulsewidth containing as much as ~ 800 mJ by a grating pair in a vacuum chamber.

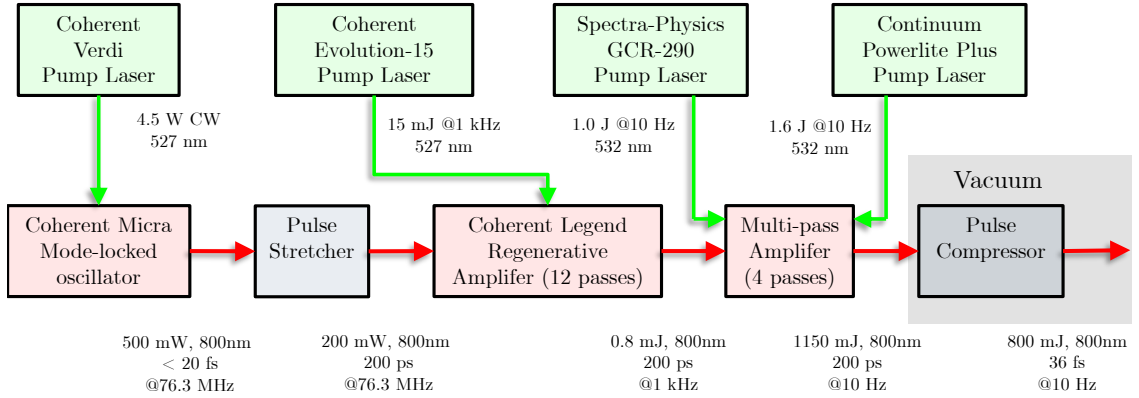


Figure 2.5: The topology of the Coherent 25 TW Ti:sapphire laser system used for the nitrogen EUV experiments presented in Chapter 5.

2.5.1 Coherent Micra oscillator

The Ti:sapphire oscillator used in this laser system is a passively Kerr-lens modelocked Coherent Micra that emits a train of < 20 fs pulses at a repetition rate of 76.3 MHz. These pulses have a center wavelength of 800 nm and > 65 nm of bandwidth at FWHM. The phase and repetition rate of the pulsetrain are actively stabilized to an RF reference by a Coherent Synchrolock via a mirror mounted to a piezo-electric transducer (PZT) in the oscillator cavity. The cavity length can be coarsely adjusted using a cavity mirror mounted on a translation stage controlled by a motorized micrometer. To compensate for the group velocity dispersion (GVD) and self-phase modulation experienced by laser pulses within the cavity, a pair of prisms are mounted on positioning stages fitted with micrometers.

The Ti:sapphire crystal in the oscillator is pumped by a Coherent Verdi, which uses a diode-pumped Nd:YVO₄ (neodymium doped yttrium orthovanadate or ‘vanadate’) gain medium that is frequency-doubled with an intracavity LBO (lithium

triborate) crystal to generate up to a 532 nm CW beam with an average power of up to 5 watts. The Verdi is enclosed within the Micra laser head, and the pump beam is directed to the Ti:sapphire crystal within the oscillator with a PZT controlled mirror, which allows the Verdi output beam pointing to be actively stabilized. To maintain thermal stability, the Micra laser head uses a Coherent Super-InvarTM baseplate with a coefficient of thermal expansion of zero at room temperature, which is actively maintained with closed-loop chiller.

2.5.2 Coherent Legend kHz regenerative amplifier (RGA)

The 76.3 MHz oscillator output is steered directly into the Coherent Legend KHz RGA enclosure. There, it first encounters the pulse stretcher that imparts a positive chirp on the beam, stretching the pulsewidth to ~ 200 ps in preparation for amplification by the RGA and multipass amplifier. The pulse stretcher uses a single concave gold grating which is struck four times by the beam as it is stretched.

The chirped 76.3 MHz pulsetrain is then coupled into the Legend kHz RGA by reflection off the laser rod. The RGA cavity contains two Pockels cells, one which actuates to trap a pulse within the cavity and another to expel the pulse after $\sim 10 - 15$ passes when it has saturated at an energy of ~ 800 mJ. The RGA is pumped by a Coherent Evolution-15, which uses a diode-pumped Nd:YLF (neodymium doped yttrium lithium fluoride) gain medium that is frequency-doubled to 527 nm by an intracavity LBO crystal. The cavity is acousto-optically Q-switched, emitting ~ 15 mJ pulses a rate of 1 kHz.

2.5.3 Multi-pass amplifier

After expulsion from the RGA cavity, the pulsetrain enters the multi-pass amplifier enclosure. Here it first encounters Pockels cell and polarizer, which allow pulses 10 per second through while attenuating all others by a factor of 10^3 . The pulses then make 4 passes through the final amplifier in a bow-tie configuration, increasing in energy from $\sim 800 \mu\text{J}$ to $\sim 1150 \text{ mJ}$. This stage is pumped by a pair of commercial q-switched frequency-doubled Nd:YAG lasers that emit 532 nm pulses with $< 10 \text{ ns}$ pulsewidth at 10 Hz, a Spectra-Physics GCR PRO-290 (1000 mJ per pulse) and a Continuum Powerlite Plus (1600 mJ per pulse). The fully amplified pulse is then transmitted through a HWP and TFP, which allows control of the amount of energy being sent into the pulse compressor (with 70% efficiency), in which a pair of gratings in vacuum compress the pulsewidth to $\sim 36 \text{ fs}$ with up to 800 mJ of energy. The 10 Hz output has a nanosecond prepulse contrast ratio of $\sim 2 \times 10^6$ (measured with a photodiode) resulting from leakage of other pulses from the oscillator $\sim 10 \text{ ns}$ prior to the main peak and a picosecond prepulse contrast ratio of $> 10^5$ (measured with a 3rd order autocorrelator, Figure 2.6), restricted by a prepulse 4 ps prior to the main pulse resulting from spectral phase modulation of the chirped pulse during amplification.

3rd Order Autocorrelation Trace

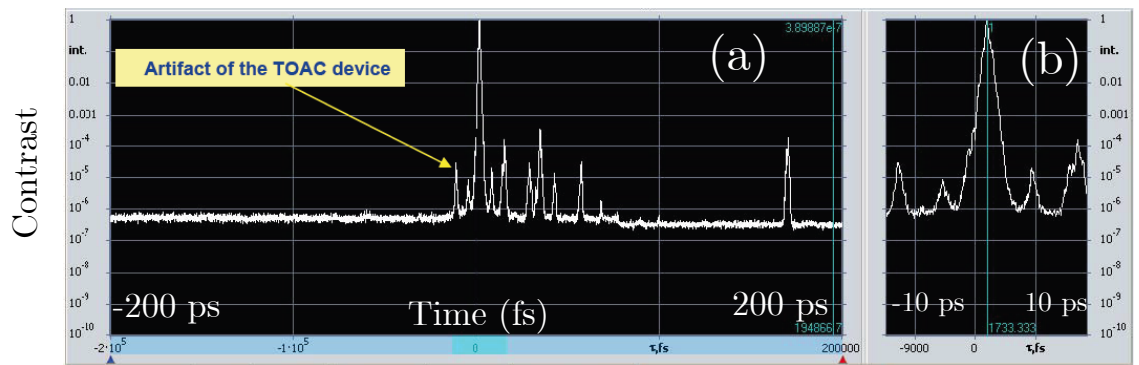


Figure 2.6: 3rd order autocorrelation trace showing that the ps contrast of the 25 terawatt laser system is $> 10^5$ within ± 200 ps of the main pulse.

Chapter 3

Review of high-intensity guiding and applications

3.1 Overview

Modern ultra-short pulse lasers attain extreme focused intensities by squeezing a modest amount of energy into an extremely small temporal and spatial region, enabling applications such as particle acceleration [20,85] and generation of coherent electromagnetic radiation at frequencies ranging from the terahertz [86] to X-ray region [87–92]. However, diffraction imposes a trade-off between the peak intensity and focal volume of a beam in free space — focusing the laser more tightly causes more rapid divergence to a larger beam of weaker intensity. This is a major practical obstacle, as the simultaneous achievement of ultrahigh intensities and large focal volumes is necessary for the most efficient and useful realization of these applications.

By definition, waveguides are the solution to this problem. However, ultra-short pulsed laser systems now routinely exceed focused intensities of 10^{18} W/cm², far greater than the 10^{12} W/cm² damage thresholds of even the most durable solids. This limits the usefulness of standard metal or dielectric waveguides, since the damage threshold of a solid is fundamentally determined by the ionization threshold of its constituent atoms. Dielectric hollow core waveguides can make it possible to guide intensities of up to 10^{17} W/cm² [93] while containing sparse concentrations of gas ($\leq 10^{15}$ atoms/cm³), but at relativistic intensities ($\geq 10^{18}$ W/cm²) only plasma

can survive. At these intensities, nonlinear laser-plasma interactions such as ponderomotive charge separation [94] and changes in electron oscillation trajectory due to relativistic mass increases [95] can make self-guiding possible, but this has proven a less practical method for extending propagation distance at ultra-high intensities than the generation of preformed plasma waveguides [29].

Over the last 20 years, many groups have developed and demonstrated plasma micro-optics capable of guiding ultra-intense laser pulses with an effectively unlimited damage threshold. This was first achieved using the radial hydrodynamic shock expansion of gas plasma heated with an axicon-focused picosecond laser pulse [29], and later demonstrated in capillaries using an electrical discharge [96–98], in other variations of the hydrodynamic shock technique [99, 100], and most recently using laser-driven hydrodynamic shocks in cluster jet targets, both end-pumped [101] and side-pumped [102]. The optical mode structure and dispersion properties of plasma waveguides has been discussed in detail [103]. Additionally, self-guiding has been demonstrated using ponderomotive charge displacement [94], relativistic nonlinearities [94, 95], and the transient nonlinear phase shift from exploding cluster nanoplasmas [61].

3.2 Guiding in hollow capillaries

While low damage thresholds render solid-core fiber optics useless for this application, hollow core-fibers can partially circumvent this limit by directly exposing the fiber to only the less intense ‘wings’ of the guided laser pulse. This has been

successfully used for single- [104] or multi-mode [105] guiding. When seeking to guide the highest possible intensities, single-mode operation is preferable, because all higher-order transverse modes confine the guided mode less tightly to the waveguide center and expose the fiber to higher intensities for a given beam energy. Linear modal analysis of single-mode propagation in a hollow-core fiber [104] predicts that during matched single-mode propagation within a 100 μm inner diameter fiber, the intensity experienced at the wall will be 10^{-4} times that of the peak intensity. Therefore, the $10^{12} - 10^{13}$ W/cm^2 damage threshold of the fiber wall for femtosecond pulses implies a maximum guided intensity $< 10^{17}$ W/cm^2 . Successfully attaining this theoretical maximum intensity within a given fiber requires high mode purity and extremely precise alignment.

However, the presence of matter in the focus is required for all applications considered in this dissertation. This can be accomplished by filling the fiber with gas, but ionization-induced refraction limits the densities that can be used to less than 10^{15} atoms/cm^3 . At higher densities, pulse energy can be refracted into the capillary walls, causing breakdown and destruction of the fiber [104].

Ionization-induced refraction occurs when the transverse intensity gradient of a beam drives different levels of ionization in a medium. In the case of a lowest-order mode propagating within a gas-filled hollow-core fiber, the central intensity peak can create plasma with a radial density gradient and an on-axis peak. This functions as a concave lens that refracts any subsequent trailing section of the pulse due to the larger negative index contribution of denser plasmas, as given by the

plasma index

$$n = \sqrt{1 - \frac{\omega_p^2}{\omega^2}} \quad (3.1)$$

where n is the index of refraction, ω is the laser frequency, $\omega_p = 4\pi n_e/m_e$ is the plasma frequency and n_e and m_e are the electron density and mass, respectively. Thus hollow-core fibers severely restrict both the peak intensity of the guided pulse and the density of the medium in which the interaction takes place, limiting their usefulness for applications.

3.3 Self-guided propagation

Once the reduced vector potential $a_0 > 0.1$, relativistic [106] and ponderomotive [19] nonlinearities within plasmas can affect beam propagation. For the 800 nm Ti:sapphire laser used in these experiments, this corresponds to an intensity $> 2 \times 10^{16}$ W/cm². These effects can have a sufficiently substantial positive index contribution to counterbalance the effects of ionization-induced refraction, allowing self-focused propagation [94].

3.3.1 Ponderomotively driven charge displacement

The ponderomotive force [19] is a cycle-averaged effect experienced by charged particles in an oscillating electromagnetic potential gradient $U(\mathbf{r})$, described by

$$\mathbf{F} = -\nabla U(\mathbf{r}) \equiv -\frac{q^2}{4m_q\omega^2} \nabla |\mathbf{E}(\mathbf{r})|^2 \quad (3.2)$$

where q and m_q are the mass and charge of the particle, $\mathbf{E}(\mathbf{r})$ is the electric field and ω is the laser frequency. This effective force is felt because electrons quivering

in the laser experience different field amplitudes in different regions of the intensity gradient, and can ‘walk away’ from regions of higher intensity over many optical cycles. This can reduce the electron density in regions of the highest intensity, decreasing the phase front velocity and self-focusing the pulse [94, 107].

3.3.2 Relativistic electron motion

The relativistic nonlinearity is due to a mass increase that occurs as the peak quiver velocity v_{osc} of free electrons in a laser field approaches the speed of light, modifying their oscillation trajectory. This effect was first predicted almost 40 years ago [106], and is described by the addition of the Lorentz factor $\gamma = (1 - v_{osc}^2/c^2)^{-1/2}$ to the plasma index of refraction n :

$$n = \sqrt{1 - \frac{\omega_p^2}{\gamma\omega^2}} \quad (3.3)$$

which has the effect upon the laser phase fronts in regions of higher γ as decreasing the plasma density would.

Theoretical studies predicted that this index modification would be strong enough to cause self-focusing above a critical power P [108, 109], later achieved experimentally in jets of gas in vacuum [95].

While Raman instabilities [110, 111], self-modulation [112] and ionization-induced refraction [113] are obstacles to relativistically self-guided propagation, they can be overcome in the highly nonlinear ‘bubble regime’ [114], and self-guiding for $> 1\text{cm}$ has been demonstrated [115, 116].

However, the high intensity onset of this effect means that this method of

self-guiding cannot be used in applications where higher intensities are unnecessary or undesired, such as high harmonic generation or X-ray lasers.

3.4 Preformed plasma channels

A different approach that can avoid the problems associated with self-guiding processes is linear propagation within a preformed plasma waveguide. For any structure to counter the spreading of a beam due to diffraction, it must have a higher on- than off-axis index of refraction, which in a plasma structure corresponds to an on-axis electron density minimum. Two mechanisms have been demonstrated for production of plasma structures fitting this description — the conductive cooling of a plasma in a capillary structure and a radial shock wave within a hydrodynamically expanding plasma column.

Assuming a plasma structure with an azimuthally symmetric, radially parabolic electron density profile $N_e(r)$, matched guiding of a lowest-order Gaussian mode is supported when the difference in electron density ΔN_e between the axis of the waveguide and the $1/e^2$ radius of the guided mode w_{ch} is

$$\Delta N_e = N_e(r = w_{ch}) - N_e(r = 0) \geq \frac{1}{\pi r_e w_{ch}^2} \quad (3.4)$$

where $r_e = 2.82 \times 10^{-15}$ m is the classical electron radius [117]. Thus guiding a lowest-order Gaussian spot with $w_{ch} = 10 \mu\text{m}$ requires $\Delta N_e \simeq 10^{18}$ electrons/cm³ [117]. Modes with smaller radii need ‘deeper’ channels with a larger ΔN_e , which can conflict with the ideal electron densities for applications such as wakefield acceleration. It should be noted that this condition is independent of the guided wavelength,

which is especially beneficial for applications such as x-ray lasers and high-order harmonic generation.

3.4.1 Laser-ionized preformed plasma channels

Guiding of high-intensity ($\geq 10^{13}$ W/cm²) laser pulses was first demonstrated by Durfee *et al.* [29] using an axicon-focused laser pulse in a chamber with < 1 ATM of gas backfill (Figure 3.1). An axicon is a conical lens with a $J_0(k_{\perp}r)$ Bessel beam focal intensity profile (shown in Figure 3.1), where k_{\perp} is the component of the wavenumber perpendicular to the beam axis as the axicon-focused beam converges.

A line-focused 100 ps pulse creates a plasma waveguide via a multi-stage ionization process followed by radial hydrodynamic expansion that creates an on-axis density minimum. First, multi-photon ionization of neutral atoms by the laser creates ‘seed’ electrons which then rapidly oscillate, or ‘quiver’ at the frequency of the laser field. These quivering electrons then collide with ions, resulting in heating (inverse bremsstrahlung) and an avalanche of ionization, because at gaseous densities the duration of the 100 ps pulse is much longer than the mean electron-ion collision time [117]. This plasma column is then hollowed out by a radial shock wave as it undergoes hydrodynamic expansion over the course of several nanoseconds (Figure 3.2) [118]. This results in an electron density profile with an on-axis electron density minimum sufficiently deep to enable the guiding of high-intensity pulses. The mode structure of these waveguides has been characterized [103] and can be controlled by varying the relative delay between the channel-creating and guided pulses.

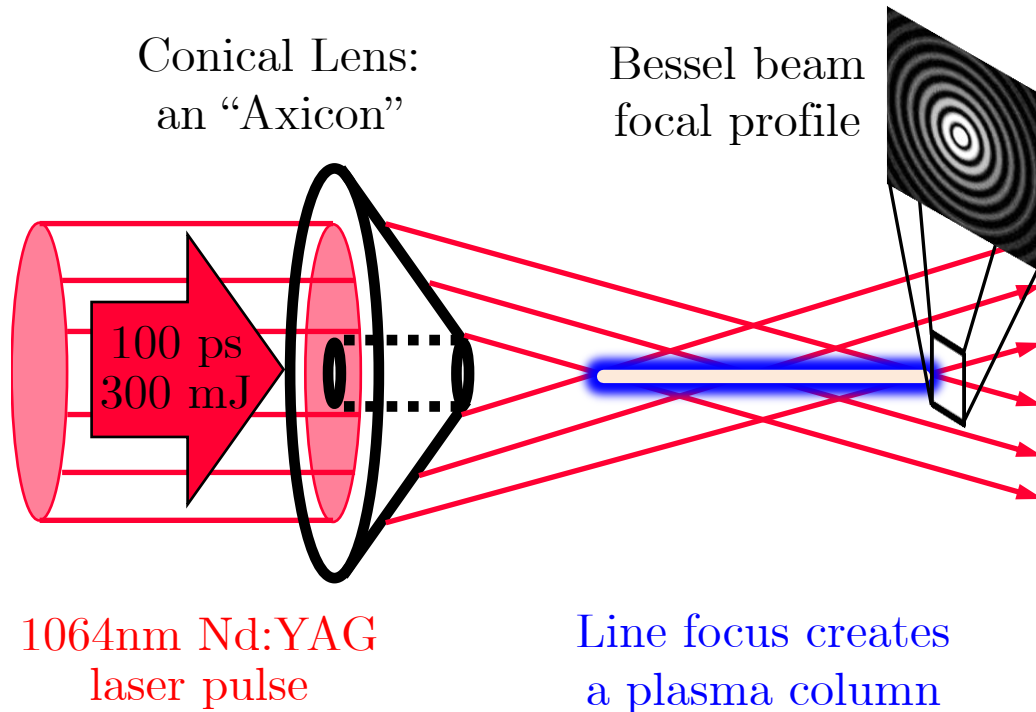


Figure 3.1: Schematic of the experimental setup first used to create a preformed waveguide. A 100 ps Nd:YAG laser pulse with up to 300 mJ was brought to a line focus with an axicon, ionizing ambient gas. As the plasma column radially expands, a hydrodynamic shock wave forms a transient structure with an local on-axis electron density minimum, allowing the guiding of high intensity pulses that are synchronized to the channel-generating pulse with a delay of several nanoseconds. The $J_0(k_{\perp}r)$ Bessel beam axicon focal profile is shown.

Temporal Evolution of Radial Electron Density

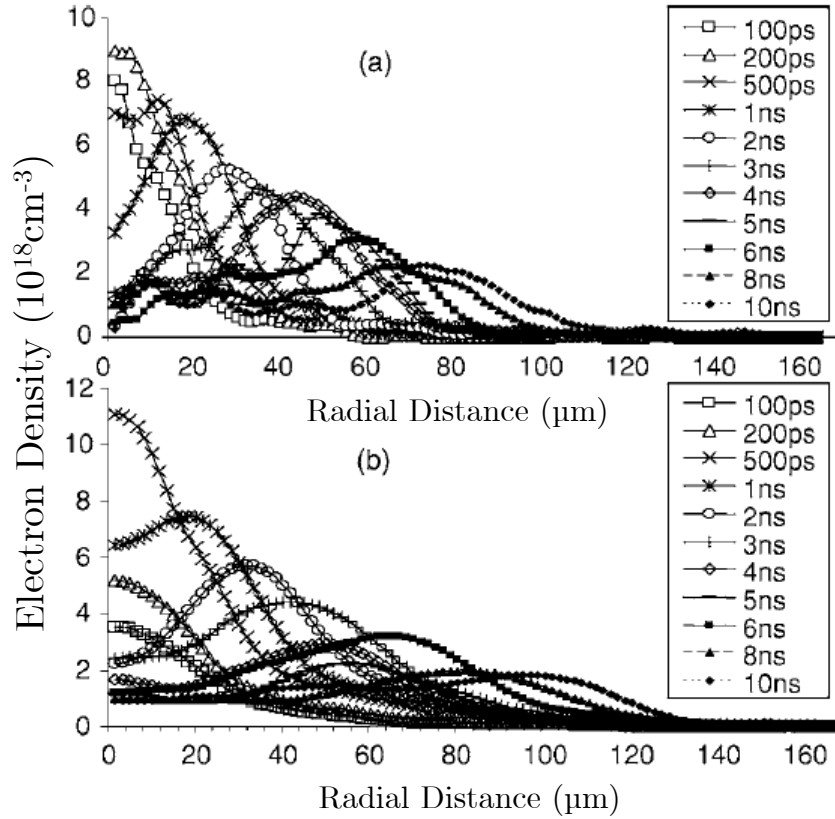


Figure 3.2: Experimental radial electron density profiles reproduced from Reference [102], showing the hydrodynamic expansion of a radial shock wave in an argon cluster jet driven by a Gaussian 100 ps FWHM 1064 nm laser pulse with 150 mJ (a) and 230 mJ (b) of laser energy.

However, ionization-induced defocusing at the waveguide entrance prevents the efficient coupling of high-intensity laser pulses into plasma waveguides produced in a gas backfill. To avoid this problem, plasma waveguides were subsequently demonstrated using 1 cm long jets of gas in a vacuum, produced by a solenoid-actuated gas valve with an elongated nozzle [119]. Guiding of high-intensity femtosecond Ti:sapphire pulses with intensities $> 10^{17}$ W/cm² was successfully demonstrated in this arrangement [120].

Since these initial experiments, other variations of this technique have been developed. Volfbeyn *et al.* [99] used a similar configuration, but with the addition of an axicon-focused femtosecond pulse prior to the picosecond pulse to aid the generation of initial seed electrons via optical field ionization (OFI). Additionally, plasma channels have been generated using pulses focused by cylindrical lenses onto the side of an elongated gas jet [99], which eases constraints in the experimental setup by allowing the guided pulse to approach the channel from a different direction than the channel-generating pulse. However, these channels usually have oval modes that are less tightly confined than the axicon-generated channels capable of single-mode guiding. The plasma columns created by self-guided laser pulses have also been used to generate shorter preformed plasma waveguides [121, 122].

However, laser-driven waveguides generated in laser-ionized gas have significant constraints, including high plasma densities ($> 10^{19}$ electrons/cm³) and inefficient channel heating efficiency, which usually does not exceed 10 – 15%. This is due to the initial electron density growth rate of $N_e(t) = N_{e0} \exp(SN_0t)$, where N_{e0} is the initial electron density, N_0 is the gas density and S is the collisional ionization

rate. The on-axis waveguide electron density lower limit cannot be circumvented by auxiliary pre-ionization schemes, because increasing N_{e0} does not increase the rate of exponential ionization growth SN_0 .

3.4.2 Electrical discharge ionized preformed plasma channels

Preformed plasma waveguides have also been produced within capillaries, first by Ehrlich *et al.* [96], who created a column of plasma by ablating the wall within an initially evacuated polypropylene $[(C_3H_6)_N]$ capillary (350 μm inner diameter) with a slow electrical discharge ($\sim 1 \mu\text{s}$). Cooling of the plasma by the bulk capillary wall material causes a radial electron temperature gradient, resulting in an approximately parabolic radial electron density profile appropriate for guiding, in this case with a matched beam spot $1/e^2$ radius of $w_0 \simeq 28 \mu\text{m}$. However, damage from the ablation process results in a capillary lifetime on the order of several hundred shots. Additionally, although the plasma is composed primarily of hydrogen that can be fully ionized by the electrical discharge, the carbon portion can not, leaving a sufficiently intense guided pulse vulnerable to ionization-induced defocusing [123].

To avoid these problems, gas-filled capillaries have been used. First, waveguide formation by the imploding phase of a fast Z-pinch discharge within a He-filled capillary was demonstrated [97]. Later, an electrical discharge was used to ionize hydrogen gas within alumina capillaries [98, 124], with a capillary lifetime of $> 10^6$ shots. This method also removes the potential complication of ionization-induced defocusing by carbon ions from the capillary wall that was present in the ablation

scheme. This configuration was used to extend the length of a laser wakefield driven by a 40 TW laser pulse to 3 cm, generating a GeV electron beam [125].

3.5 Guiding using cluster plasmas

More recently, the propagation of intense pulses has been extended beyond the diffraction limit with several techniques that take advantage of different aspects of the nonlinear laser-cluster interaction. Self-guided propagation has been demonstrated in jets of exploding clusters [61], which also creates a plasma waveguide after several nanoseconds of radial hydrodynamic expansion [101]. Additionally, by placing jets of clustered gas in the line focus of a picosecond laser, the average gas density can be decoupled from the initial electron density growth rate, enabling the creation of waveguides with lower on-axis electron density and heating that is up to an order of magnitude more efficient than is possible in unclustered gaseous targets [102].

3.5.1 Self-guided propagation

As discussed in Chapter 1, when atomic clusters are irradiated with an intense laser pulse, the real polarizability can be initially positive due to the super-critical plasma density at the core of the exploding nanoplasma, shielding and excluding the laser field. The magnitude of the net positive contribution to the index of refraction is strongly nonlinear in the laser intensity, with a larger transient positive value for larger intensities. As a result, a laser with a beam profile that peaks on-

axis can experience self-focusing due to the transiently concave index of refraction profile [61]. Additionally, during the expansion of the super-critical density region in the cluster, there is a critical density layer in which the imaginary part of the polarizability has peaked, resulting in efficient absorption. This effect has been used to achieve self-guided propagation of up to 8 mm with only 25 mJ of laser energy (Figure 3.3) [101].

As was the case with the plasma column left in the wake of relativistically self-guided pulses, hydrodynamic expansion of this 8 mm column results in waveguide formation after ~ 1 ns of radial hydrodynamic expansion, and preformed guides created in this fashion were used to guide pulses with a peak intensity of 3×10^{17} W/cm², limited by the available laser energy [101].

3.5.2 Preformed waveguide formation

Clusters have proven a useful alternative medium to unclustered gases for the generation of axicon-pumped preformed plasma channels, allowing lower density, higher stability and more efficient laser-heating than is possible in gases of comparable average density. When using a 100 ps laser pulse brought to a line focus within an elongated jet of clusters, absorption efficiencies were shown to be $> 35\%$ [102], compared to $\sim 10\%$ in gas, despite the fact that clusters expand and drop below the plasma critical density in less than a picosecond [63]. To explain the disparity between the laser pulsewidth and nanoplasma expansion timescale, it is helpful to view the laser-cluster interaction as two-stage process. First, the far leading edge of the

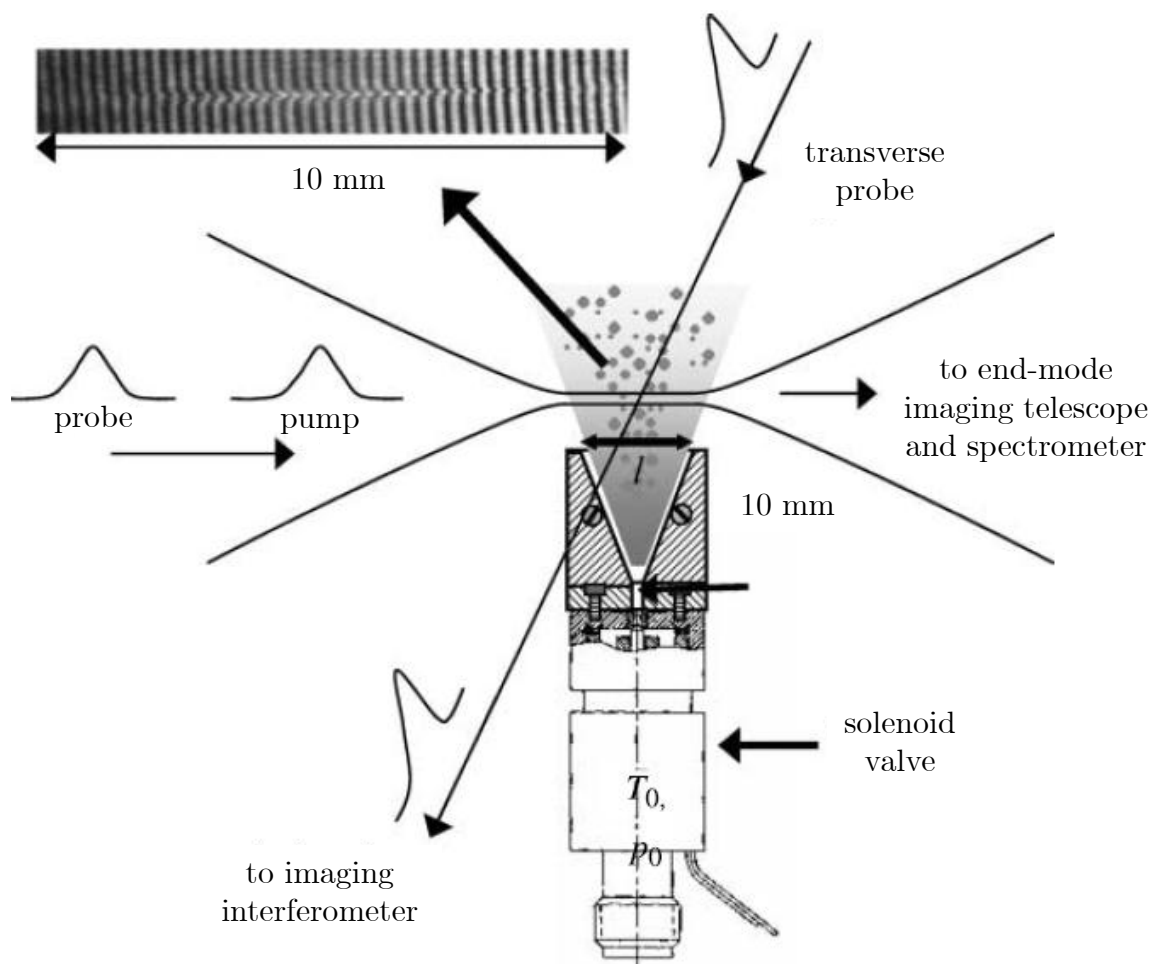


Figure 3.3: Schematic of the experimental setup used to create preformed plasma waveguides using a self-guided femtosecond laser pulse in an elongated cluster jet [101].

100 ps pulse encounters clusters at near solid density, which are ionized extremely efficiently through electron collisional ionization prior to the arrival of the majority of the pulse energy. These dense, deeply ionized nanoplasmas then expand, cool and merge over several picoseconds to form a uniform plasma that is then efficiently heated by the majority of the pulse energy that then follows [102].

In a gas, the early initial ionization grows at an exponential rate $\propto N_{e0} \exp(SN_0t)$, where S is the collisional ionization rate, N_{e0} is the initial electron density and N_0 is the gas density. In most cases $N_{e0} \ll N_0$, the ‘memory’ of N_{e0} does not persist once the initial exponential growth phase of ionization ends and the final plasma density is determined by the gas density N_0 . If the gas density is too low insufficient ionization occurs for plasma channel formation. As a result, most preionization schemes (such as those using femtosecond OFI [99]) which increase N_{e0} but leave the initial effective ionization $Z_{\text{eff}} \ll 1$ are still incapable of producing waveguides with on-axis plasma densities $< 5 \times 10^{18} \text{ cm}^{-3}$.

Clusters, on the other hand, can allow the creation of waveguides with on-axis plasma densities $\sim 10^{18} \text{ cm}^{-3}$ because the high initial local densities within the clusters allow the far leading edge of a 100 ps pulse to create plasma with a large average degree of ionization $Z_{\text{eff}} \gg 1$ [102]. The remainder of the pulse, which is much shorter than the timescale for recombination, can then efficiently heat the merged cluster plasma [102].

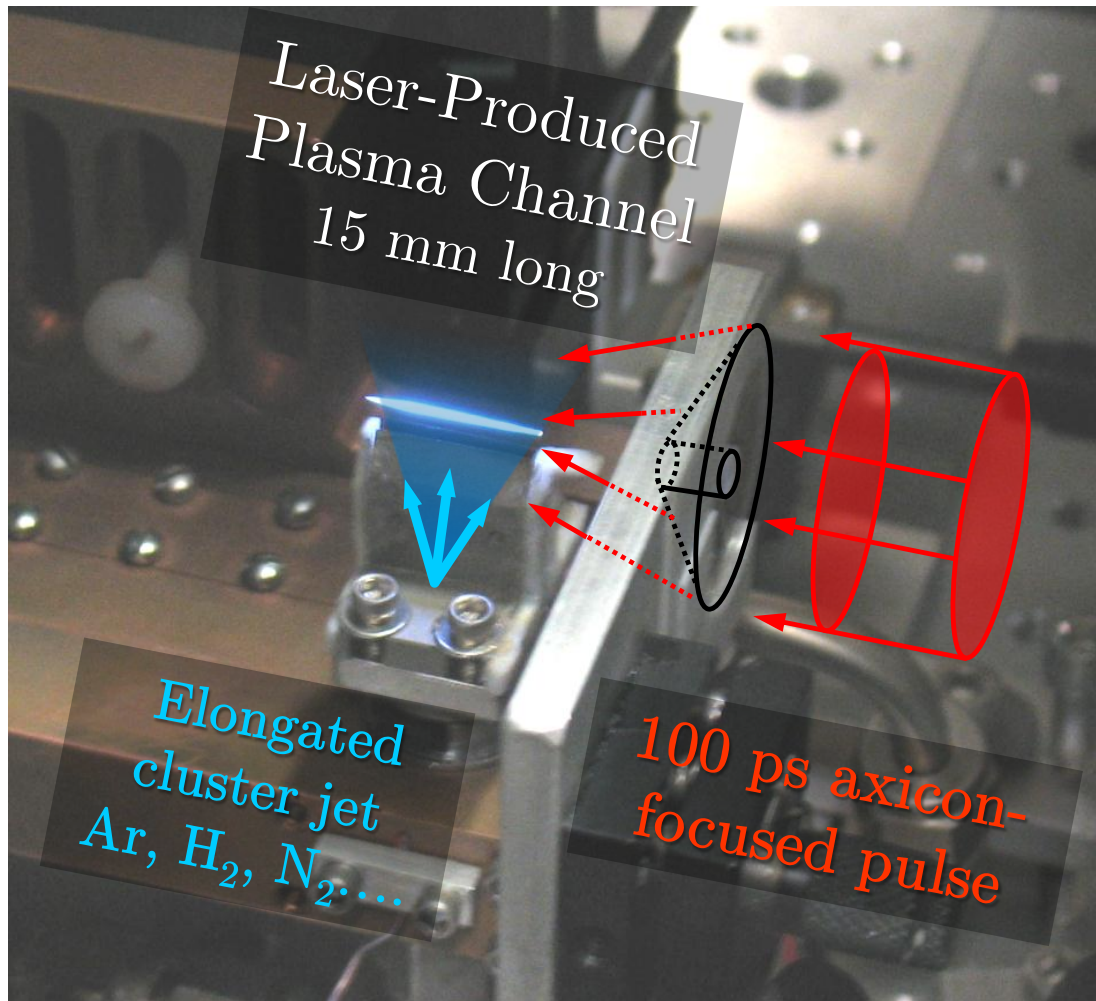


Figure 3.4: Photograph of the experimental setup used to create plasma waveguides in elongated cluster jets using axicon-focused 100 ps pulses.

3.6 Applications of plasma waveguides

Plasma waveguides can extend the interaction volume between high-intensity focused laser pulses and matter, removing the diffraction-imposed trade-off between focal intensity and volume. However, after guiding has maintained focused propagation for many vacuum Rayleigh lengths, phase-matching between the laser pulse and process can become a dominant limitation for applications such as acceleration of charged particles [126–128] and the generation of coherent EUV [129] and terahertz radiation [86]. Depending on the application, ‘phase matching’ refers to the mismatch between either the phase or group velocity of the driving laser pulse and the velocity of a relativistic particle beam or the phase velocity of newly generated electromagnetic radiation.

3.6.1 High harmonic generation (HHG)

High-harmonic generation (HHG) is a prominent example of an application in which phase matching is critical. HHG can produce bright, coherent EUV or x-ray emission from the interaction between an intense laser pulse and an ensemble of atoms or ions. The modulated waveguides developed in this dissertation could be used to quasi-phase match this interaction in cases where phase matching is not possible, such as in the presence of deeply ionized plasmas.

HHG is an extreme extension of low-order harmonic generation, which occurs when a laser field of frequency ω with intensity $> 10^7$ W/cm² drives anharmonic oscillations of bound electrons about the nucleus of an atom or ion, leading to the

emission of light at harmonics of the laser frequency (2ω , 3ω , etc.). Low-order harmonic generation can be understood by perturbatively expanding the polarizability \mathbf{P} as a power series in the electric field \mathbf{E} :

$$\mathbf{P}(t) = \chi^{(1)}\mathbf{E}(t) + \chi^{(2)}\mathbf{E}^2(t) + \chi^{(3)}\mathbf{E}^3(t) + \dots \quad (3.5)$$

where the strength of n th order processes, including $n\omega$ harmonic generation, is determined by the n th order susceptibility of the material $\chi^{(n)}$.

However, once strength of the laser field becomes of the same order as the atomic electric field in the ‘strong field’ regime ($I_0 \geq 10^{13}$ W/cm²), the atomic potential is severely distorted and perturbation theory is no longer valid. The high harmonic generation that has been observed in this regime (greater than 700th order [130]) can instead be understood using the semiclassical model developed by Corkum [131], in which a laser pulse of frequency ω temporarily liberates an electron from the nucleus of an atom, accelerates it away and then back over a half-cycle of the laser field, where it re-collides with the nucleus, releasing the potential and kinetic energy as a single photon with frequency $q\omega$. The maximum possible photon energy that can be attained with this process, the so-called ‘cut off’ energy, is:

$$\hbar\omega_c = I_p + 3.17U_p \quad (3.6)$$

where ω_c is the ‘cutoff frequency’, I_p is the ionization potential of the electron and U_p is the ponderomotive potential of the electron within the laser field, given by

$$U_p = \frac{e^2 E^2}{4m_e \omega^2} \propto I \lambda^2 \quad (3.7)$$

where e is the charge of an electron, m_e is the electron mass, and E and ω are the

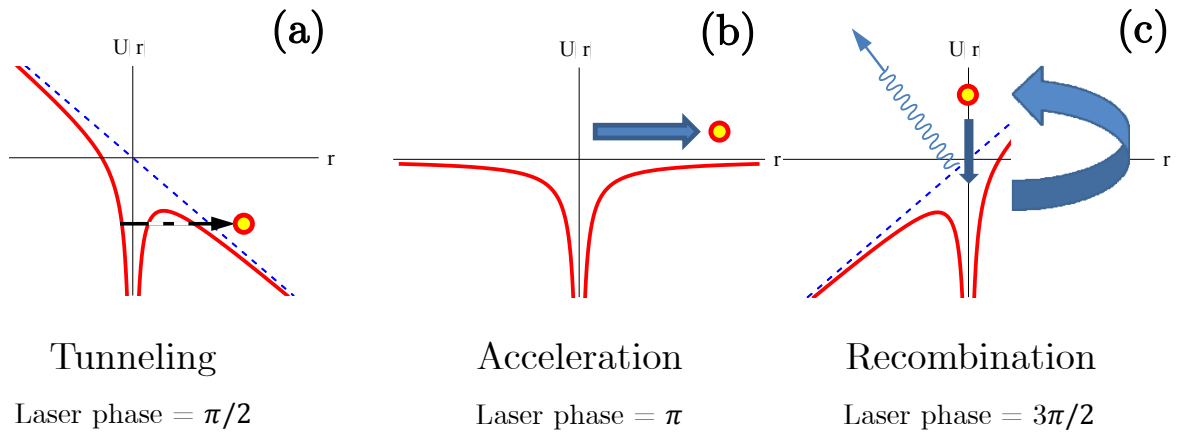


Figure 3.5: Representation of the multi-stage ionization process. First, the electron is ionized (a) at the peak of the laser field, then it is accelerated away from the nucleus (b), then it recollides (c) emitting an EUV photon.

the amplitude and frequency of the driving laser electric field, respectively. This semiclassical picture of the HHG process was corroborated soon afterwards using fully quantum mechanical theory [90].

3.6.1.1 Phase-matching

To generate harmonics sufficiently bright for use in applications, a large ensemble of atoms is required at the focus of the driving laser, in which macroscopic factors, especially phase-matching, can have a large effect on conversion efficiency. Phase matching refers to the relative difference in phase velocity between the fundamental and harmonic waves in the nonlinear medium, usually expressed as the difference in propagation constant $\Delta k = qk_0 - k_q$, where k_0 is the fundamental

wavenumber and k_q is the wavenumber of the q th harmonic. When there is a phase mismatch $\Delta k \neq 0$, newly generated harmonics will be perfectly out of phase with those previously generated after a coherence length $L_c = \pi/\Delta k$ of propagation within the medium. This harmonic intensity then sinusoidally oscillates with propagation distance, at a period of $2L_c$. Thus when the goal is maximizing the brightness of generated harmonics, extending the interaction length beyond L_c is pointless and can even be counterproductive.

3.6.1.2 Quasi-phase matching

When an adequate phase matching is not possible, quasi-phase matching (QPM) of the interaction then becomes necessary. QPM periodically modifies the index mismatch as the pulse propagates to partially compensate for imperfect matching. Quasi-phase matching has been most successfully implemented in low-order harmonic generation, by using crystals with a periodically poled structure that reverses after each coherence length, allowing extremely high efficiencies. This polarization flip reverses the relative phase between the fundamental and harmonic fields just as they have completely slipped out of phase, causing the pre-saturation harmonic intensity to grow at a rate reduced by $\pi/4$ compared to what would be achieved with perfect phase matching.

In HHG, quasi-phase matching cannot be implemented in periodically poled crystals due to the lower damage threshold and high absorption of EUV in solids. However, several other means for periodically correcting the phase mismatch in

HHG have been successfully implemented by suppressing the HHG process every other coherence length L_c , eliminating the out of phase harmonic production that would otherwise cause destructive interference. Mathematically, this process can be understood as adding an extra term $\Delta k_{QPM} = \pi/L_c$ to the wavenumber mismatch that compensates for the dispersion experienced in the un-matched HHG.

In waveguides, this was first achieved by adding diameter modulations to gas-filled capillaries with an axial periodicity of [132, 133], and later via mode-beating in straight pre-ionized plasma waveguide within a capillary [134]. These methods modulate the intensity of the guided pulse, periodically reducing the efficiency of the HHG process. Additionally, counterpropagating pulse trains [135] or a counter-propagating infrared beam [136] were used to periodically interfere with the HHG process in a capillary. In free space, evenly spaced jets of gas separated the coherence length in vacuum [137] and specially designed gas jets with alternating zones of different gas species [138] have also been demonstrated.

In this dissertation, we present a pair of techniques for generating periodically modulated plasma waveguides that could allow implementation of quasi-phase matched HHG without the driving pulse intensity limitations of previous techniques. In addition, these newly developed structured plasma waveguides could be used to quasi-phase match the direct acceleration of charged particles [126].

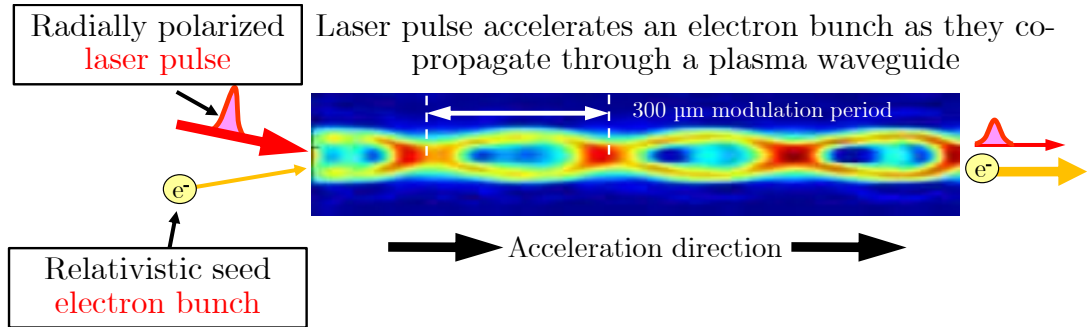


Figure 3.6: Overview of the direct laser acceleration scheme. When a relativistic seed electron bunch and a radially polarized laser pulse are injected into a modulated plasma waveguide with proper phasing, there is an axial component of the laser field that causes the electron bunch to feel net acceleration over many cycles of the laser field.

3.6.2 Direct acceleration of charged particles (DLA)

There is currently great interest in Laser Wakefield Acceleration (LWFA), a laser-based particle acceleration scheme that may lead to a new generation of compact, energetic and cost effective particle accelerators. LWFA uses an intense ultrashort laser pulse to drive a plasma wave in its wake. The charge separation in this plasma wave results in extremely strong electric fields $> 10^{11}$ V/m, capable of accelerating a co-propagating electron bunch [20]. This method has been successfully implemented in a 3 cm long plasma waveguide to produce a GeV electron beam, driven by a 40 TW peak power laser pulse [125].

However, while the multi-TW laser systems capable of ponderomotively driving the highly nonlinear plasma waves required for LWFA are smaller and less expen-

sive than a conventional accelerator with similar capabilities, these systems begin to approach the limits of what a smaller, university-scale lab can accommodate. Additionally, the nonlinearity of the plasma wave used to couple energy from the laser pulse to the electron bunch makes it difficult to attain the necessary pointing and emittance stability required for the staging of several accelerators.

Direct acceleration of charged particles (DLA) [126] is currently being developed as an alternative laser-based particle acceleration scheme. The acceleration gradient of this method scales linearly with the laser field intensity, and can therefore be used with smaller lasers that cannot attain the intensities required to drive wakefields. The primary obstacles to directly accelerating charged particles with laser light are the transverse and oscillatory nature of the laser electric field, and DLA solves those problems with a radially polarized driving pulse and modulated plasma waveguides presented in this dissertation, respectively. Simulations have shown that relatively modest laser pulses from few-mJ femtosecond kHz regenerative amplifiers could directly accelerate electrons with a gradient of ~ 100 MV/cm [126].

The most obvious obstacle to using electromagnetic waves for direct particle acceleration is the fact that the electric fields at the focus of the linearly polarized output of most lasers is transverse, and the interaction between charged particles and a laser in a cross-propagating geometry is too brief to facilitate efficient energy transfer. Thus in an ideal scenario the electric field and wave vector of the laser would point in the same direction, to allow an extended interaction between an axially directed electric field component and a co-propagating electron bunch. This can be accomplished using a radially polarized laser pulse, for these beams have an

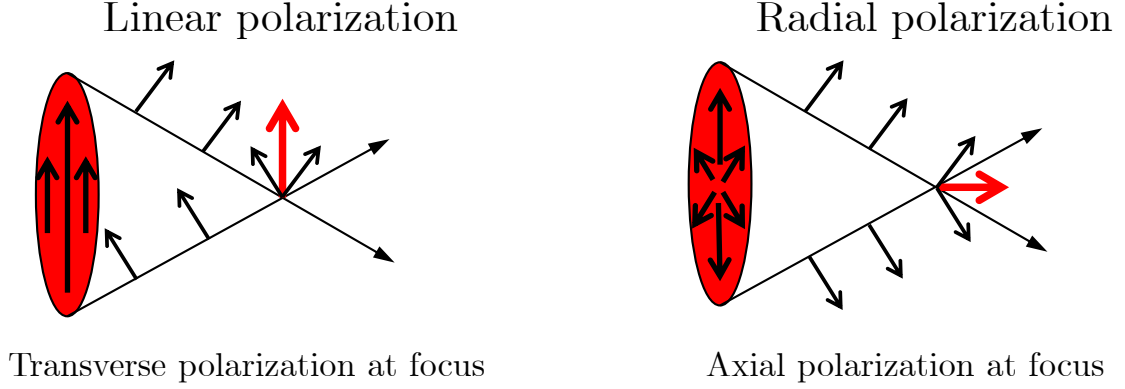


Figure 3.7: Schematic illustration of how a radially polarized laser pulse has an on-axis electric field component in the propagation direction of the laser when focused.

axial component when focused (Figure 3.7). This can be seen because $\nabla \cdot \mathbf{E} = 0$, where

$$\nabla \cdot \mathbf{E} = \frac{\partial E_r}{\partial r} + \frac{1}{r} \frac{\partial E_\theta}{\partial \theta} + \frac{\partial E_z}{\partial z} = 0 \quad (3.8)$$

and since $\partial E_\theta / \partial \theta = 0$ for a radially polarized beam, $\partial E_r / \partial r = -\partial E_z / \partial z$ and $E_z \neq 0$. However, like every component of any electromagnetic wave, E_z is oscillatory and when focused in free space will give an equal and opposite backwards push for each forwards push, with no net acceleration over many optical cycles.

To achieve perfectly phase-matched direct laser acceleration, the phase velocity of the axial component of the laser field must be the same as the velocity of the charged particle bunch. The Woodward-Lawson theorem [139] states that the net energy gain of a relativistic electron interacting with an electromagnetic field in vacuum is zero, because the strictly subluminal electron velocity can never match the speed of light at which the laser phase travels. However, placing a gas in the laser focus violates the assumption of vacuum in this theorem, slows the laser phase

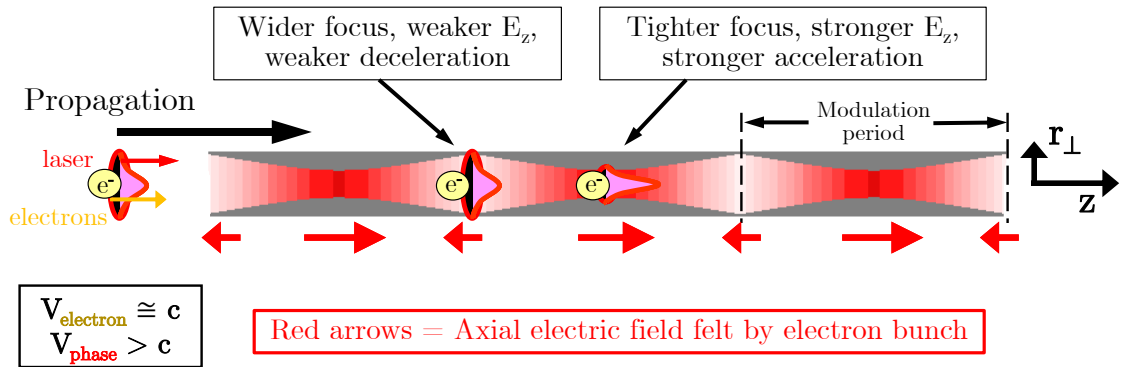


Figure 3.8: Schematic drawing illustrating how radially polarized light within a modulated waveguide can do work on co-propagating electrons in spite of the oscillatory nature of the electric field. When the modulation period is $L_c/2$, the electron bunch experiences one cycle of the laser field with each waveguide period, feeling a backwards push when the mode is wider and a forwards push when the mode is narrower and more intense, leading to a net gain in energy with each modulation period.

velocity and makes it possible to achieve phase-matching by tuning the pressure of the gas. This was demonstrated by Kimura *et al.* in an inverse Cherenkov geometry, yielding an acceleration gradient of 310 keV/cm [140].

As was the situation with pressure-tuned phase matching in HHG, the ionization threshold of the gas restricts the laser intensity due to the strictly superluminal plasma phase velocity which cannot be matched with the subluminal particle velocity. Thus at higher intensities, quasi-phase matching becomes necessary. The modulated plasma waveguides presented in this dissertation [141, 142] could accomplish this with a modulation period of $2L_d$, emphasizing the in-phase accelerating forces and de-emphasizing the out of phase decelerating forces in a structure with an effectively unlimited damage threshold [126–128].

3.6.2.1 Slow waves

In addition to discussing the effects of channel modulations upon laser propagation in the terminology of quasi-phase matching, we can view the modulated plasma channel as a 'slow wave' structure. This is especially relevant to DLA, as this language is usually used to discuss the structured copper cavities used in RF based particle accelerators. The direct laser acceleration scheme is analogous to these conventional accelerators, using plasma structures instead of copper, driven by infrared optical radiation instead of microwaves.

The phase velocity of a Gaussian beam in an unmodulated plasma channel is

$$\frac{v_p}{c} = 1 + \frac{\bar{N}_e}{2N_{cr}} + \frac{\lambda_0^2}{2\pi^2 w_{ch}^2} \quad (3.9)$$

where w_{ch} is the $1/e$ field radius of the guided mode, \bar{N}_e is the average electron density on axis, N_{cr} is the critical density and $\lambda_0 = 2\pi/k_0$ is the laser vacuum wavelength [126,127]. For the deeply ionized plasmas required in waveguides capable of withstanding the propagation of ultra-high intensity pulses, the phase velocity in a straight channel is strictly superluminal.

However, a modulated plasma waveguide adds a negative term to the right hand side of the phase velocity equation,

$$\frac{v_{p.mod}}{c} = \frac{v_p}{c} - \frac{m\lambda_0}{d} = 1 + \frac{\bar{N}_e}{2N_{cr}} + \frac{\lambda_0^2}{2\pi^2 w_{ch}^2} - \frac{m\lambda_0}{d} \quad (3.10)$$

where m is an integer and d is the axial modulation period of the waveguide. This term from the modulation can balance the positive contribution of the plasma, creating ‘slow wave’ components of the propagating beam at values of m that yield a subluminal phase velocity. This occurs because the corrugations add additional ‘branches’ to the ω versus k dispersion diagram, where $k = k(\omega)$ is the axial wave number of the guide and ω is the angular frequency. More specifically, adding axial modulations allows a new set of solutions to satisfy Maxwell’s equations within the waveguide, given by $u(\mathbf{r}_\perp, z, \omega) \exp(ikz)$, where $u(\mathbf{r}_\perp, z + d, \omega) = u(\mathbf{r}_\perp, z, \omega)$ and $k = k_c(\omega) + 2\pi m/d$ (from the Floquet-Bloch theorem), u is an electromagnetic field component, \mathbf{r}_\perp is transverse position and k_c is the fundamental axial wave number [143]. Direct acceleration becomes possible when the subluminal phase velocity of one of the slow waves components m matches the velocity of co-propagating relativistic charged particles.

For the experimentally measured parameters presented in Chapter 4, of $w_{ch} =$

$15 \mu\text{m}$, $\bar{N}_e/N_{cr} = 4 \times 10^3$ and $l/d = 2.7 \times 10^3$, $m \geq 1$ is required for a sub-luminal phase velocity. If the dominant contribution to the generation of slow spatial harmonics comes from the variation of the wave phase ϕ from sinusoidal density modulations of relative amplitude δ , then $d\phi/dz = -k_0\alpha \cos(2\pi z/d)$, where $\alpha = \delta\bar{N}_e/(2N_{cr})$ and the ratio of the amplitude of the m th spatial harmonic to the local field amplitude is $E_m/|E| = J_m(\alpha d/\lambda)$, where J_m is the ordinary Bessel function. The magnitude of a given spatial harmonic can thus be maximized by the appropriate choice of the density modulations and their period. In the case of Figure 4.12(b)(ii), $\delta = 0.43$ gives $\alpha d/\lambda = 0.32$. Thus, the relative amplitude of the first slow-wave harmonic is $J_1(0.32) \simeq 0.16$, for which $(1 - v_p/c) = 5.2 \times 10^{-4}$ and relativistic $\gamma \simeq 30$.

Chapter 4

Modulated Plasma Waveguides

Here we present two newly developed methods that add periodic modulations to plasma waveguides generated using the hydrodynamic shock technique in a cluster jet [141, 142]. These structures enable the pursuit of several exciting lines of research which require quasi-phase matching, including direct acceleration of charged particles driven by guided, radially polarized femtosecond pulses [126–128], high harmonic generation [132, 133] and the creation of high-power terahertz pulses [86].

4.1 Experimental setup

Modulated waveguides were demonstrated using two methods, both of which are modified versions of the setup used to make laser-produced unmodulated waveguides in cluster jets described in Chapter 3. In the first, a laser pulse with a radially periodic intensity distribution is brought to a line focus on a uniform clustered target using an axicon [141]. This creates and nonuniformly heats a plasma column, leading to axially periodic diameter modulations in what we refer to as a ‘corrugated’ structure. The second uses a uniform laser pulse and a nonuniform clustered target with sharp discontinuous gaps at periodic intervals imposed by placing wire obstructions in the cluster flow [142]. These two techniques lead to periodically modulated channels with distinct characteristics that are optimal for different applications.

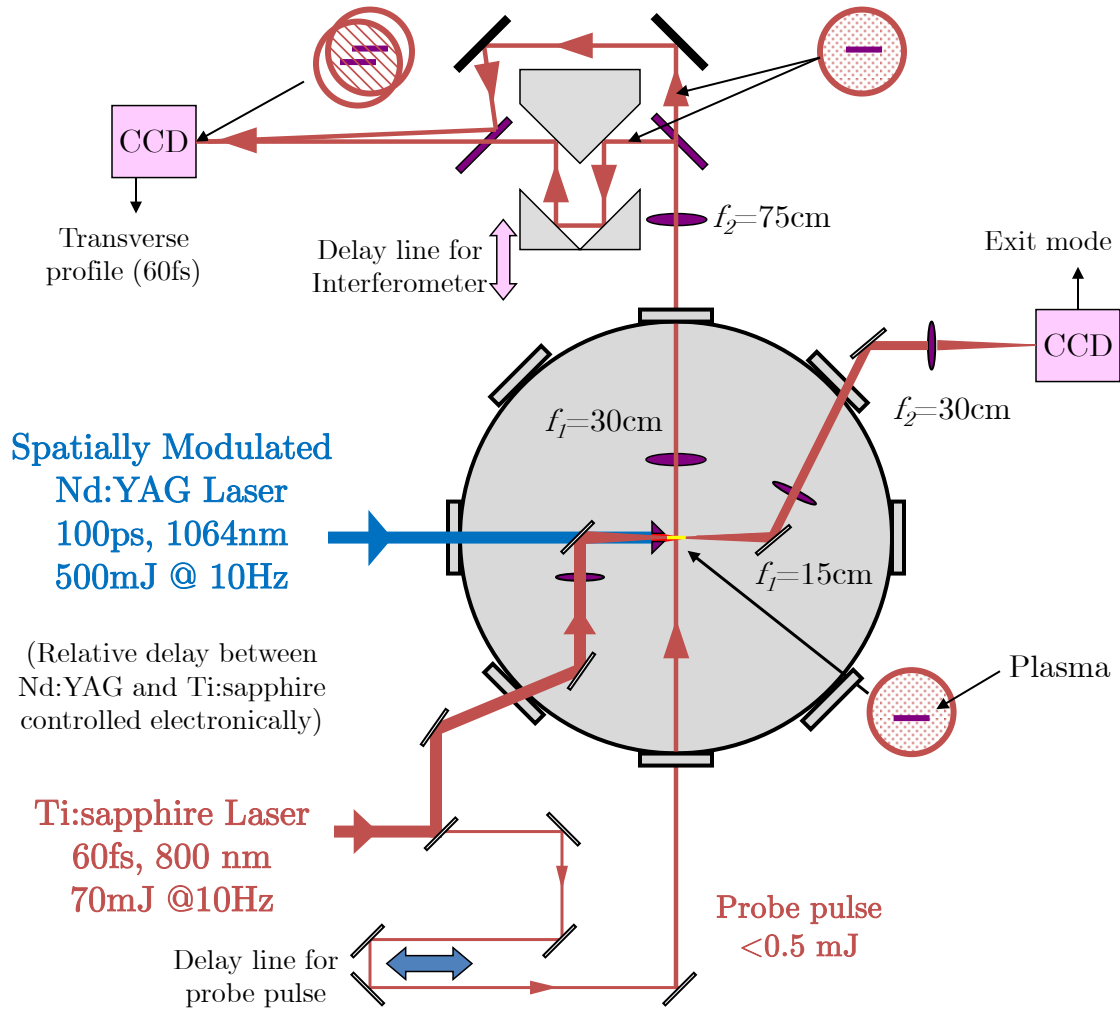


Figure 4.1: Experimental layout for generation of channels using the hydrodynamic shock method. An axicon-focused Nd:YAG laser pulse (200 – 800 mJ, 100 ps, 1064 nm), which overfills an elongated cluster jet target making a 15 mm plasma channel. Modulations can be imposed upon the plasma waveguide by either spatially modulating the Nd:YAG pulse with a ring grating or obstructing the cluster jet at periodic intervals with wires. Ti:sapphire laser pulses (70 mJ, 60 fs, 800 nm) were guided after being focused to the entrance of the channel entrance through a hole in the axis of the axicon.

In both modulation methods, a 100 ps Nd:YAG laser pulse (10 Hz, 1064 nm, up to 800 mJ) is focused by an axicon to a 25 mm line-focus positioned 2 to 3 mm above a 15mm long elongated jet of clusters. The cluster jet is generated by the cryogenically cooled source described in Chapter 2, using a solenoid actuated gas valve with a 1 mm diameter orifice connected to an elongated nozzle with a 15 mm long, 1 mm wide exit geometry. The mean cluster size and average atomic density within the jet was controlled using valve temperature, backing pressure, gas species and nozzle geometry as described in detail in Chapter 2. This line focus overfills the length of the cluster jet, resulting in a 15 mm long plasma column (Figure 4.2). After the arrival of the Nd:YAG laser pulse at time $\tau = 0$, a radial hydrodynamic shock wave in the plasma column drives expansion, resulting in a tubular plasma profile with an on-axis electron density minimum when $0.1 \lesssim \tau \lesssim 10$ ns. This profile supports guiding of low-order modes with reasonable coupling efficiency when $1 \lesssim \tau \lesssim 3$ ns. A Ti:sapphire laser pulse (70 mJ, 60 fs, 800 nm) then arrives and is focused through a hole in the axis of the axicon and coupled into the entrance of the waveguide.

The channel length can be extended by increasing the length of the cluster jet and/or decreasing the base angle of the axicon. The use of a clustered target in conjunction with an axicon-focused 100 ps pulse allows decoupling of the average gas density from the degree of ionization within the plasma channel as discussed in Chapter 1. This setup is used to generate both types of modulated plasma channels, with the addition of either a transmissive diffractive optic (a ‘Ring Grating’, Figure 4.2(d)) to periodically modulate the laser intensity, or the addition of an array of

Ring Grating Modulated Waveguide Layout

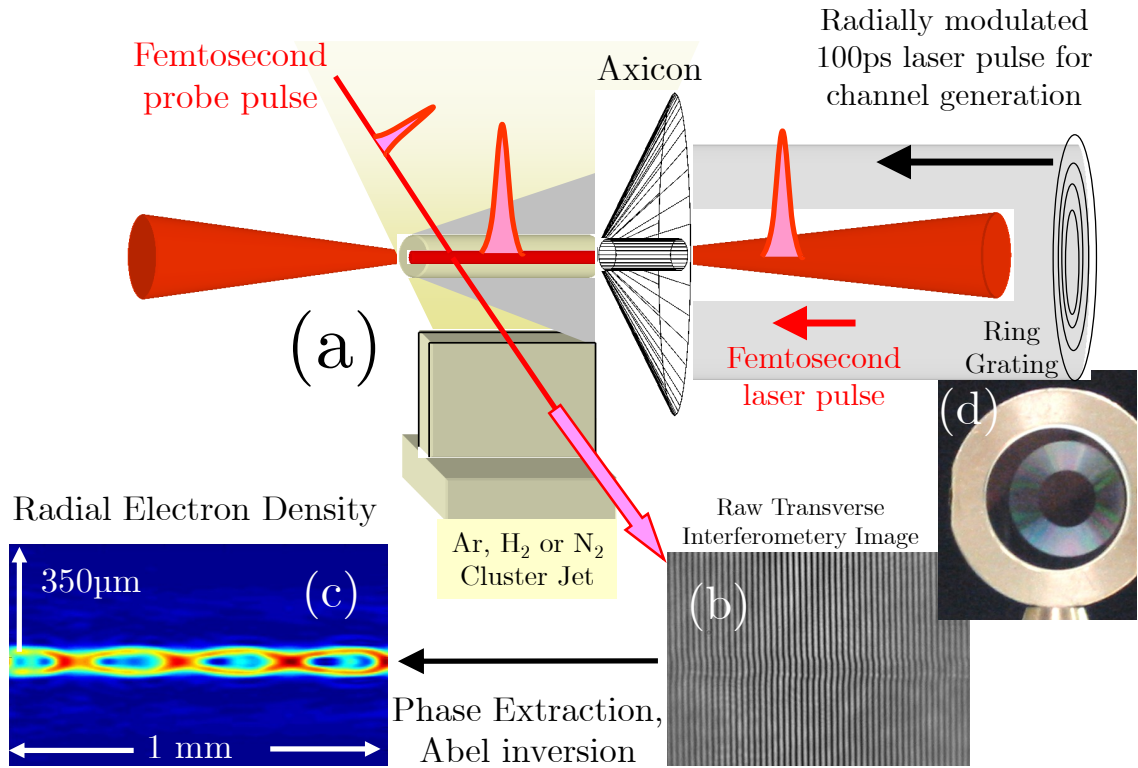


Figure 4.2: Detail of the interaction region for generation of channels using the hydrodynamic shock method. First, an axicon-focused Nd:YAG laser pulse (200 – 500 mJ, 100 ps, 1064 nm) that has been radially modulated by transmission through a ring grating (*d*) creates a modulated plasma channel in an elongated cluster jet. A Ti:sapphire laser pulse (70 mJ, 60 fs, 800 nm) arrives 1 – 3 ns later and is then focused to the entrance of the guide through a hole in the axis of the axicon. The radial plasma density of the channel (*c*) was directly measured by Abel inverting the extracted phase from an interferogram (*b*) taken with a 60 fs probe pulse.

wire obstructions to modulate the cluster jet.

Radial and axial profiles of the plasma density were obtained with the optical interferometry setup shown in Figure 4.1. A small portion of the femtosecond pulse (~ 1 mJ) is sent transversely through the plasma column (Figure 4.2(a)), which imparts a phase shift on a section of the probe. The probe pulse is then split, spatially offset, and recombined in a folded wavefront interferometer. By using the flat phase front at the edge of the beam as a reference, the phase shift imparted by the plasma is encoded in the spatial phase of the fringes of an interferogram collected by a CCD camera (Figure 4.2(b)). This image is processed by extracting the phase and Abel-inverting the image about the axis to obtain radial density profiles (Figure 4.2(c)). A detailed description of the algorithm used to implement the Abel inversion integral can be found in a prior dissertation from our group [144]. In addition, this imaging system can collect ‘shadowgrams’ when an arm of the interferometer is blocked, producing an image that shows how the probe pulse is refracted by the plasma, used primarily as an alignment diagnostic.

4.1.1 Waveguide stability

Cluster-based plasma waveguides were generated at a repetition rate of 10 Hz with extremely high stability, exhibited in the exit modes of the guided femtosecond pulses. In sequences of 100 consecutive end mode images of guided femtosecond pulses in hydrogen (argon) cluster plasmas, we observed RMS centroid jitter of 2.6 (3.5) μm with a mean FWHM of 15.4 (18.9) μm , as determined by a Gaussian

fit to each spot profile [141]. The primary source of jitter is the pointing of the femtosecond laser prior to coupling into the waveguide. By tuning the relative delay between the channel generating 100 ps laser pulse and the guided femtosecond pulse, we can achieve consistent single mode guiding. A sequence of 12 consecutive guided end mode images from an unmodulated hydrogen plasma waveguide are shown in Figure 4.3. The waveguide acts as a spatial filter for the guided pulse. Neither of the modulation techniques presented here negatively affects waveguide stability.

4.2 Ring grating (RG) modulations

Our first method for imposing axial modulations upon a plasma channel relies upon the use of a ‘ring grating’ (RG), a transmissive diffraction grating with azimuthally symmetric rulings (shown in Figure 4.2(d)), which we fabricate by lithographically etching concentric grooves on the surface of a 1” diameter, laser-grade fused silica disc. By centering a RG in the path of the channel-generating 100 ps laser pulse, the transmitted beam acquires radial intensity modulations as a result of interference between multiple diffracted orders from the grating. Upon subsequent refraction and focusing by the axicon, the radial intensity modulations result in axial intensity modulations in the $J_0(k_{\perp}r)$ focal intensity profile at the line focus (bottom right panel in Figure 4.4), leading to periodic variations in plasma heating at the central on-axis intensity maximum. By carefully choosing the groove period, depth and duty cycle (ratio etched to unetched area) of this pattern we can control the properties of the waveguide modulations.

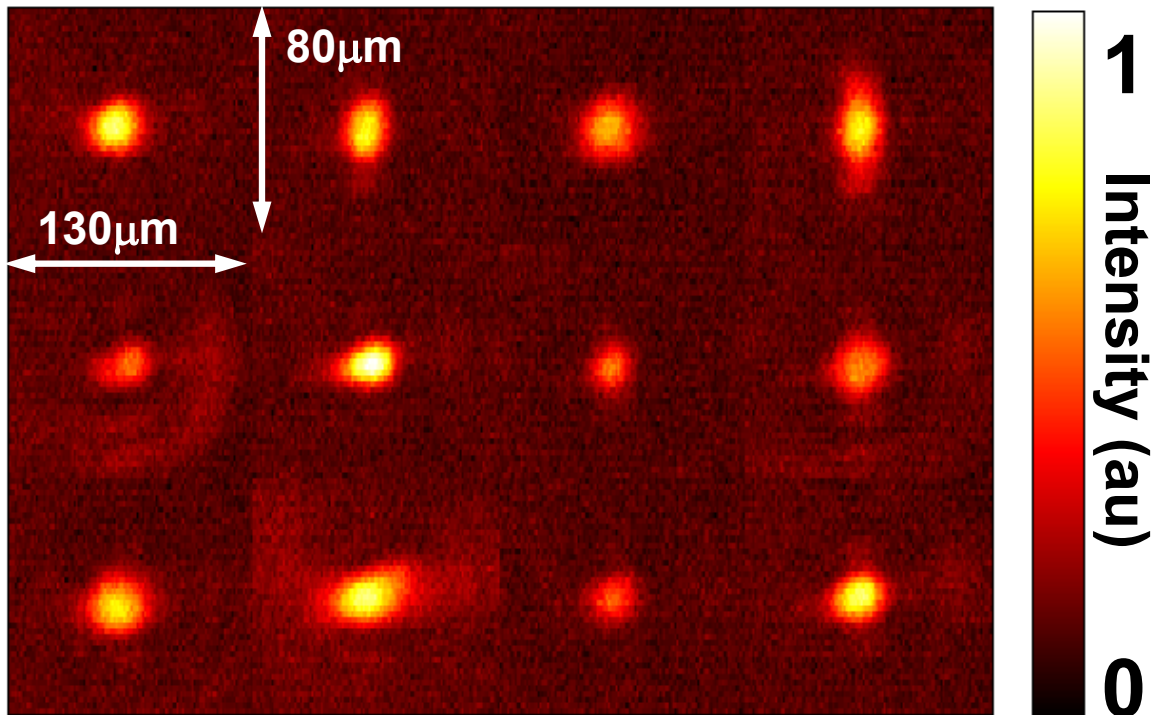


Figure 4.3: A sequence of 12 consecutive end mode images of guided Ti:sapphire pulses (20 mJ, 60 fs, 800 nm) in unmodulated hydrogen plasma waveguides with a relative delay of 1 ns. The channels were generated by Nd:YAG laser pulses (500 mJ, 100 ps, 1064 nm) focused in a jet of hydrogen clusters released by a source that was held at a temperature of -150° Celsius with 800 psi backing pressure. The set of images from which this sequence was taken has an RMS jitter of $2.6 \mu\text{m}$ and mean FWHM of $15.4 \mu\text{m}$. The main source of jitter in these images pointing of the femtosecond laser prior to coupling into the waveguide, the plasma structure itself is extremely consistent.

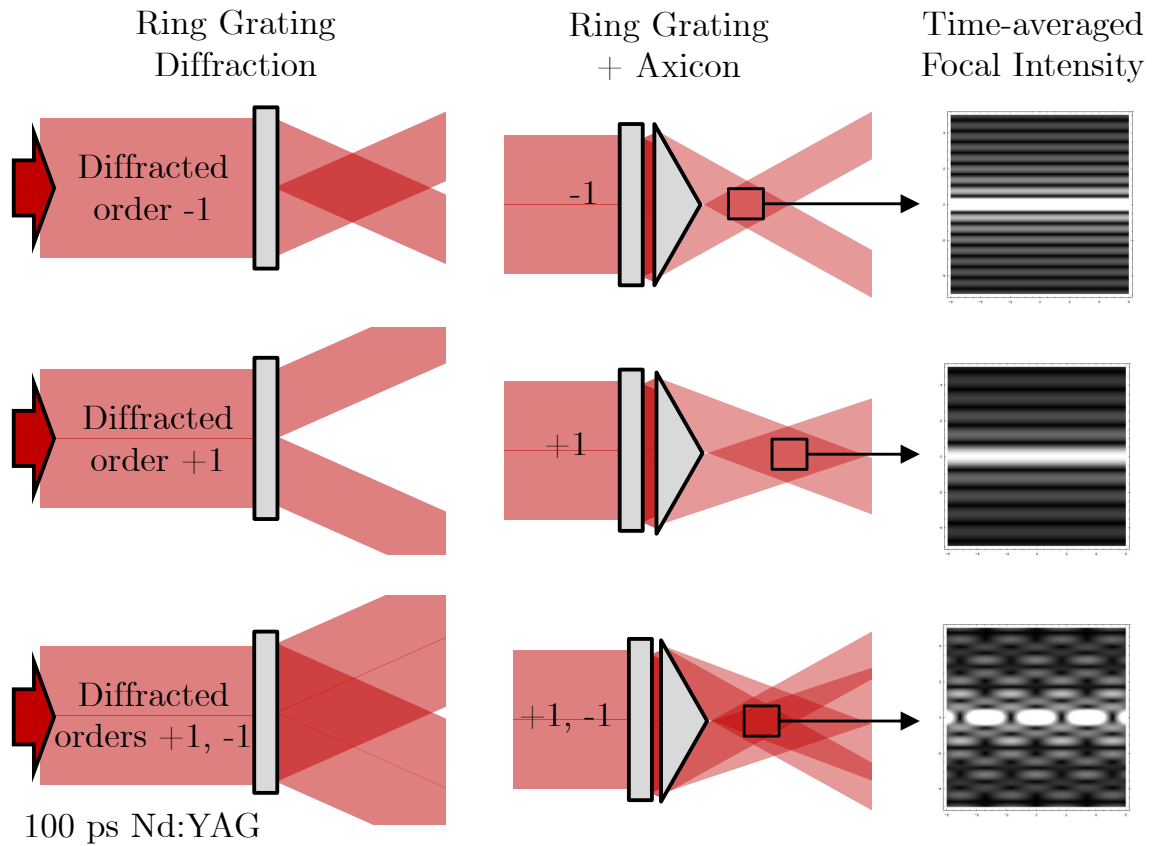


Figure 4.4: Sectional diagrams showing the radius vs propagation direction as a beam travels through a ring grating and then an axicon, demonstrating how periodic modulations are imposed. The lithographic etch depth of the grating was chosen to maximize the efficiency of the $n = \pm 1$ diffracted orders, so only those are shown. The $n = -1(+1)$ diffracted order of the ring grating is an inwardly (outwardly) traveling Bessel beam which converges towards the line focus of the axicon at a sharper (shallower) angle than the $n = 0$ order beam, as shown in the first (second) row. When both are focused together as shown in the third row, they interfere on-axis, resulting in a time-averaged intensity profile with periodic axial modulations.

The 100 ps pulse can be thought of as an impulse on the hydrodynamic time scale ($\sim 0.1 - 0.5$ ns) of the heated bulk plasma column formed from merged cluster explosions that remains after the pulse [102]. The merged cluster plasma then undergoes radial hydrodynamic expansion, with a faster expansion shock wave occurring in regions that underwent more intense heating, producing a diameter-modulated corrugated plasma waveguide (Figure 4.2(c)).

The ring gratings were fabricated at the University of Maryland Laboratory for Physical Sciences (LPS) by transferring the patterns from chrome-on-sodalime masks (custom fabricated by Microtronics Inc.) with contact lithography, which uses a layer of photoresist on 1" diameter fused silica discs followed by reactive ion etching. The etch depth was chosen to be $\sim 1 \mu\text{m}$ to impose a $\sim \pi$ phase shift on alternating radial zones of the 1064 nm Nd:YAG pulse, minimizing the intensity of the zero-order transmitted beam. A ring grating is the Fresnel lens equivalent of an axicon, creating Bessel beams with finite transverse extent.

When light of wavelength λ is incident upon the rulings with an angle θ_i from the surface normal, light is diffracted according to the grating equation,

$$\sin \theta_i + \sin \theta_m = \frac{m\lambda}{d} \quad (4.1)$$

where d is the groove period and m th order diffracted maxima occur at θ_m for integer values of $m = 0, \pm 1, \pm 2, \pm 3, \dots$. In these experiments, the ring gratings are used in a normally incident geometry (with the beam incident on the ungrooved side of the window), so $\theta_i = 0$ and order m is diffracted with an angle $\theta_m = \arcsin\left(\frac{m\lambda}{d}\right)$. In a grating with parallel grooves, the diffracted orders are plane waves, but in these

azimuthally symmetric gratings the m th diffracted orders form cones of rays that converge or diverge at θ_m .

By placing a ring grating in series with an axicon, multiple diffracted orders from the grating are brought to a common line focus, where they interfere and result in periodic axial intensity modulations (Figure 4.4). The angles γ_m (with respect to the beam axis) with which the m th Bessel beam approaches the line focus of an axicon is determined by the initial angle θ_m (also with respect to the beam axis) and the base angle of the axicon θ_{base} (the angle between the conical and flat faces of the axicon) by applying Snell's law twice, as the beam enters and exits the axicon as follows:

$$\theta_{mid} = \arcsin\left(\frac{n_1}{n_2} \sin \theta_m\right) \quad (4.2)$$

$$\gamma_m = \arcsin\left(\frac{n_2}{n_1} \sin(\theta_{base} + \theta_{mid})\right) - \theta_{base} \quad (4.3)$$

where n_1 and n_2 are the indices of refraction of the medium of incidence (vacuum in this case) and axicon, respectively, and θ_{mid} is the Bessel beam angle with respect to the axis, within the axicon. In our setup, a fused silica axicon with an index of refraction $n_2 = 1.4496$ at 1064nm and a base angle of $\theta_{base} = 28^\circ$ was used.

As the Bessel beams that originated as the m th diffracted orders of a ring grating converge through the line focus of the axicon at angles γ_m , they will interfere. In the case of the $m = \pm 1$ orders, the time-averaged on-axis electric field amplitude is

$$E(z) = e^{ik \cos \gamma_1 z} + e^{ik \cos \gamma_{-1} z} \quad (4.4)$$

which has the on-axis ($r = 0$) intensity distribution

$$I(z) = |E(z)|^2 = |e^{ik \cos \gamma_1 z} + e^{ik \cos \gamma_{-1} z}|^2 \quad (4.5)$$

$$= 1 + e^{ik(\cos \gamma_1 - \cos \gamma_{-1})z} + e^{-ik(\cos \gamma_1 - \cos \gamma_{-1})z} + 1 \quad (4.6)$$

$$= 2(1 + \cos(k(\cos \gamma_1 - \cos \gamma_{-1})z)) \quad (4.7)$$

so the on-axis intensity modulations from a pair of Bessel beams converging at angles γ_1 and γ_{-1} have a period Λ_m of

$$\Lambda_m = \frac{2\pi}{k(\cos \gamma_1 - \cos \gamma_{-1})} \quad (4.8)$$

which is half the period of the field modulations. In a given experimental configuration, the values of γ_1 and γ_{-1} are determined by the angles with which the diffracted orders from the ring grating are refracted towards the line focus by the axicon. In these experiments, ring gratings with periods $d = 10, 40, 70, 100,$ and 300 were used, which correspond to $m = \pm 1$ order diffracted angles of $\theta_{\pm 1} = 6.10^\circ, 1.52^\circ, 0.87^\circ, 0.61^\circ$ and 0.20° respectively.

4.2.1 ‘Beating’ of an odd number of diffracted orders

In practice, the transmitted $m = 0$ order of the ring grating was not completely eliminated by our choosing etch depth to give a π phase shift, and the $m = 0$ order was co-focused with the $m = \pm 1$ diffracted orders by the axicon. This added an envelope of lower frequency axial periodicity (henceforth referred to as ‘beats’) to the line focus of the axicon (Figures 4.5 and 4.6) in a way that could severely disrupt quasi-phase matched processes. These ‘beats’ were observed in plasmas generated

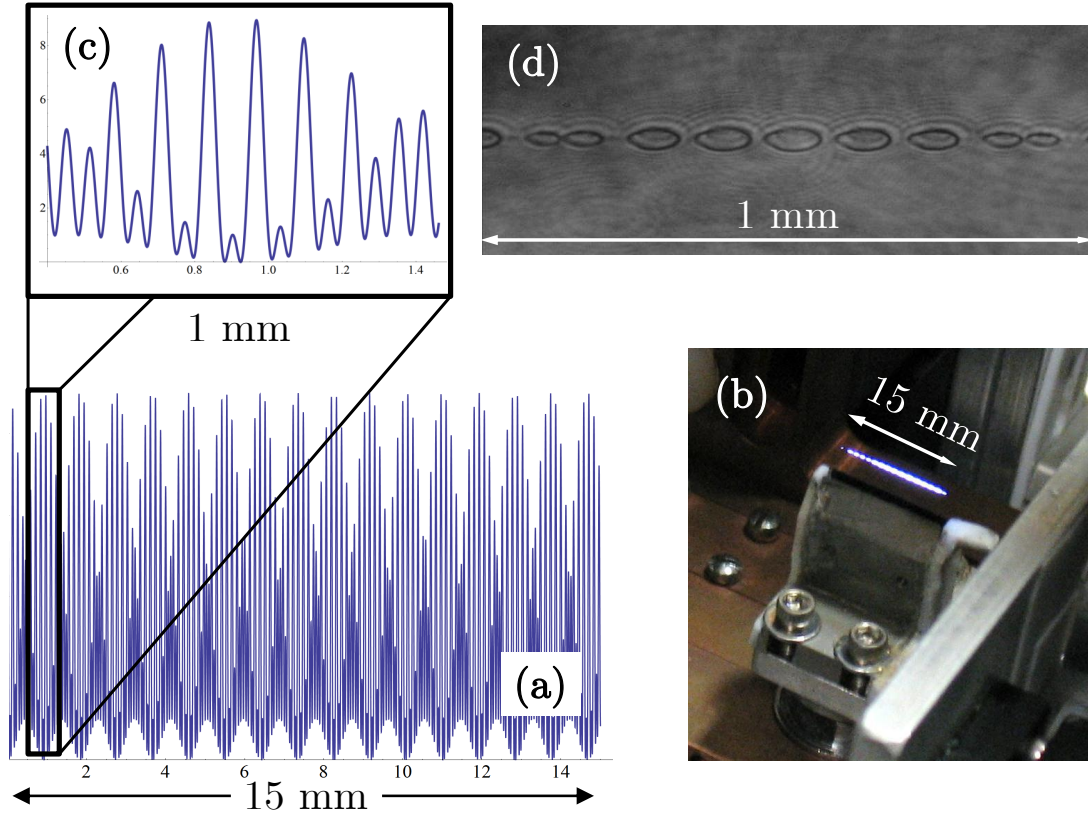


Figure 4.5: Diagram showing agreement between experimentally generated plasma profiles and a calculated intensity profile for a $40\ \mu\text{m}$ ring grating, for which $\theta_{\pm 1} = 1.524^\circ$. When used in conjunction with a $\theta_{base} = 28^\circ$ base angle fused silica axicon, this corresponds to γ_1, γ_0 and γ_{-1} values of $16.742^\circ, 14.886^\circ$ and 13.067° , respectively. Plot (a) and photograph (b) predict and demonstrate a $\sim 1.1\ \text{mm}$ beat period, and plot (c) and shadowgram (d) predict and show a modulation period of $\sim 130\ \mu\text{m}$. The plasma shown in (b) and (d) was generated in atmosphere.

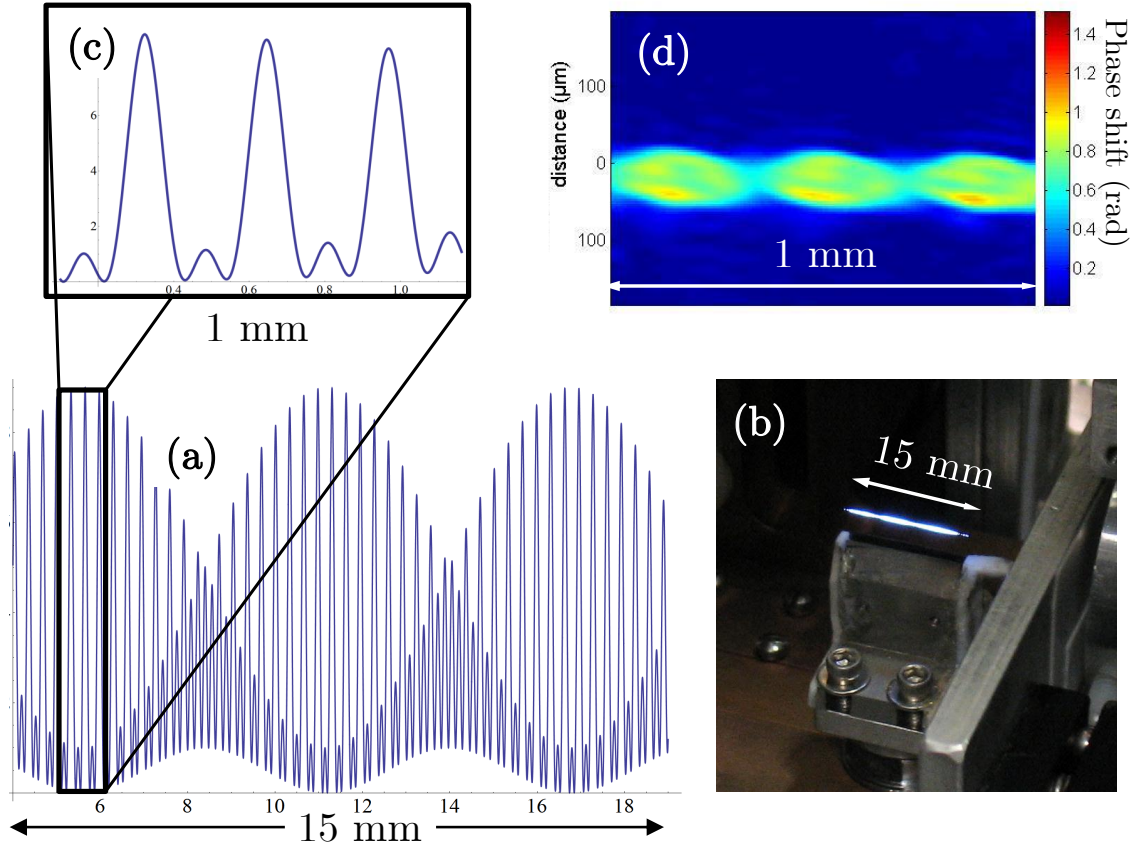


Figure 4.6: Diagram showing agreement between experimentally generated plasmas and a calculated intensity profile for the focal intensity of a $100 \mu\text{m}$ ring grating, for which $\theta_{\pm 1} = 0.610^\circ$. When used in conjunction with a $\theta_{base} = 28^\circ$ base angle fused silica axicon, this corresponds to γ_1, γ_0 and γ_{-1} values of 15.624° , 14.886° and 14.155° , respectively. Plot (a) and photograph (b) of a plasma generated in atmosphere show agreement with a ~ 5.5 mm beat period, and plot (c) and probe phase image (d) (of a plasma created in an argon cluster jet) show a modulation period of $\sim 330 \mu\text{m}$.

in atmosphere and cluster jets and could be eliminated by imaging the ring grating and blocking the $m = 0$ order, which will be discussed in the following section. It may also be possible to completely eliminate the $m = 0$ transmitted order by more carefully fabricating the gratings closer to the ideal specification of an etch depth of 1064 nm and a duty cycle of 50/50.

To determine the details of this periodic behavior we consider three Bessel beams approaching a line focus and at angles γ_1 , γ_0 and γ_{-1} with equal intensity and wave number magnitude k . Neglecting polarization, this results in a time-averaged electric field at $r = 0$ with axial dependence of

$$E(z) = e^{ik \cos(\gamma_1)z} + e^{ik \cos(\gamma_0)z} + e^{ik \cos(\gamma_{-1})z} \quad (4.9)$$

which results in an intensity

$$I(z) = |E(z)|^2 = \left(e^{ik \cos(\gamma_1)z} + e^{ik \cos(\gamma_0)z} + e^{ik \cos(\gamma_{-1})z} \right) \dots \quad (4.10)$$

$$\times \left(e^{-ik \cos(\gamma_1)z} + e^{-ik \cos(\gamma_0)z} + e^{-ik \cos(\gamma_{-1})z} \right)$$

$$= 1 + 2 \cos[k(\cos(\gamma_1) - \cos(\gamma_0))z] + \dots \quad (4.11)$$

$$1 + 2 \cos[k(\cos(\gamma_1) - \cos(\gamma_{-1}))z] + \dots$$

$$1 + 2 \cos[k(\cos(\gamma_0) - \cos(\gamma_{-1}))z].$$

To understand the behavior of this expression, the axial intensity profile $I(z)$ is plotted for two sets of $\gamma_1, \gamma_0, \gamma_{-1}$ (Figures 4.5(a) and 4.6(a)) corresponding to those found in experimentally tested ring grating and axicon pairs, at two levels of magnification, along with images (photographic and probe pulse) of corresponding experimentally

generated channels. Ring gratings with a ruling period of 100 and 40 μm were used, for which $\theta_{\pm 1} = 0.610^\circ$ and 1.524° , respectively. When used in conjunction with a $\theta_{base} = 28^\circ$ base angle fused silica axicon, this corresponds to γ_1, γ_0 and γ_{-1} values of $15.624^\circ, 14.886^\circ, 14.155^\circ$ and $16.742^\circ, 14.886^\circ, 13.067^\circ$ respectively. The wavenumber of our $\lambda = 1064$ nm Nd:YAG laser in vacuum is $k = 2\pi/\lambda = 5.9 \times 10^6$. It can be clearly seen that the periodicity of the predicted and experimentally measured structures match almost perfectly.

The critical observation to be taken away from these plots is that the high frequency intensity oscillations undergo a π phase shift with each ‘beat’, resulting in destructive interference and cancellation of quasi-phase matching in any interaction longer than the beat period, which was ~ 5.5 mm for 330 μm modulations (Figure 4.6) and 1.1 mm for 130 μm modulations (Figure 4.5). This beating effect will occur whenever an odd number of diffracted orders interfere at the focus.

4.2.2 Ring grating imaging

To eliminate the ‘beats’ and avoid their detrimental effects upon quasi-phase matched processes, the ring grating was imaged to the line focus of the axicon instead of being placed directly in front of the axicon. This allows us to physically block the $m = 0$ order at the intermediate focus while leaving the $m = \pm 1$ orders unimpeded. Aberration introduced to the beam by the imaging system did not affect the angles γ_m with which the diffracted orders converge upon the line focus of the axicon, as there was no measured change in the periodicity of the plasma channel after the

addition of the imaging system.

The imaging setup consisted of pair of 75 mm diameter plano-convex lenses with a $f = 15$ cm focal length placed 30 cm apart, imaging the ring grating 60 cm downstream. These large diameter imaging lenses were chosen to have sufficient numerical aperture to catch the diffracted orders being relayed to the cluster jet. The optical elements in the path of the laser were, in order, the ring grating, a $f = 15$ cm planoconvex lens, a 1064 nm AR coated BK7 glass vacuum window, a second $f = 15$ cm planoconvex lens, an 800 nm mirror at 45° (which combines the channel-generating and guided beams) and finally a 28° fused silica axicon.

The ring grating was held in an optical mount on a 3-axis transverse positioning stage in atmosphere, allowing the axes of the axicon and ring grating to be lined up with respect to one another with sufficient precision. The amount of transverse positioning precision required is of the order of the ring grating modulation period. Alignment of gratings with periods $< 100 \mu\text{m}$ was difficult in initial experiments, because flex of the vacuum chamber walls after evacuation was sufficient to misalign the ring grating with respect to the axicon. Additionally, when imaging the ring grating, each diffracted order of the ring grating comes to a high-intensity line focus in the process of being imaged from the ring grating to the cluster jet, so the axial position of the optics had to be carefully chosen to avoid damage.

Additionally, as the ruling period of the grating becomes smaller and θ_m becomes larger, the line foci of the $+m$ and $-m$ diffracted orders shift further away from and closer to the axicon, respectively (Figure 4.4). Due to the finite transverse extent of the beam, this reduces the axial length of the region of overlap between the

diffracted orders and thus the length of the modulated guide that can be created. To enable full overlap of all diffracted orders at the line focus and make the most efficient use of the beam energy available, the ring grating can be imaged on the line focus instead of simply placing it next to the axicon as shown in Figure 4.4.

4.2.3 Range of generated modulation periods

Figures 4.6(*d*) and 4.7(*b*) show phase images extracted from transverse interferograms of modulated channels with 330 and 35 μm modulation periods in an argon cluster jet, generated by ring gratings with radial groove periods of 100 and 10 μm . The use of clustered targets acts to greatly stabilize plasma generation and is responsible for our ability to ‘sculpt’ fine and consistent modulation features. Note that all density profiles shown are extracted from the average phase of 200 consecutive interferograms, and the shot-to-shot extracted density variation is less than 5%.

Corrugated guides were also generated in backfill gases. Figure 4.7(*a*) shows a shadowgram of a modulated channel produced in air with a period of 35 μm with a 10 μm ruling period RG. However, channels generated in backfill are not useful for guiding high intensity pulses due to ionization-induced defocusing, which prevents the pulse from reaching peak intensity and efficiently coupling into the entrance of the waveguide. We use these backfill plasmas primarily as an alignment diagnostic.

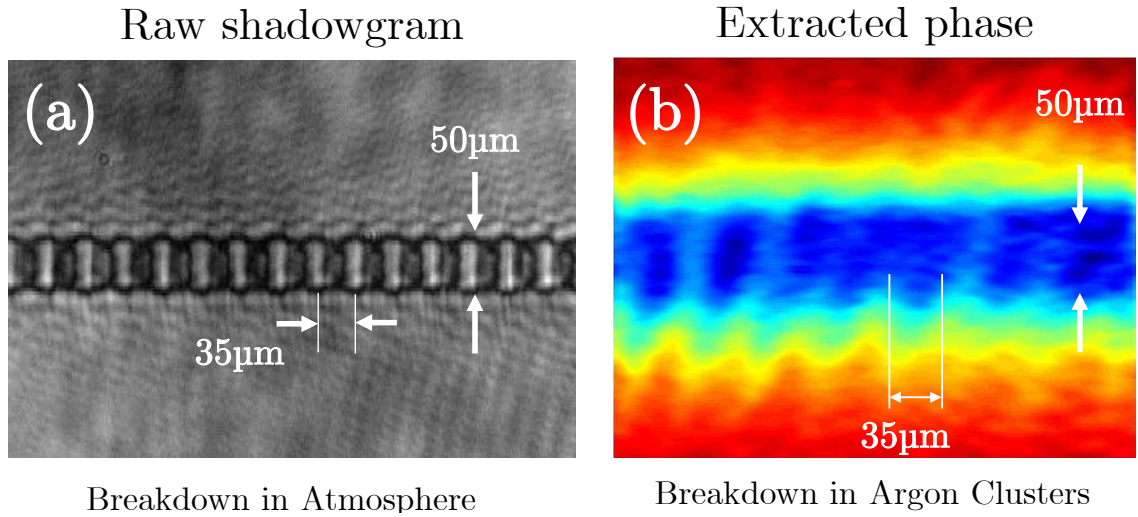
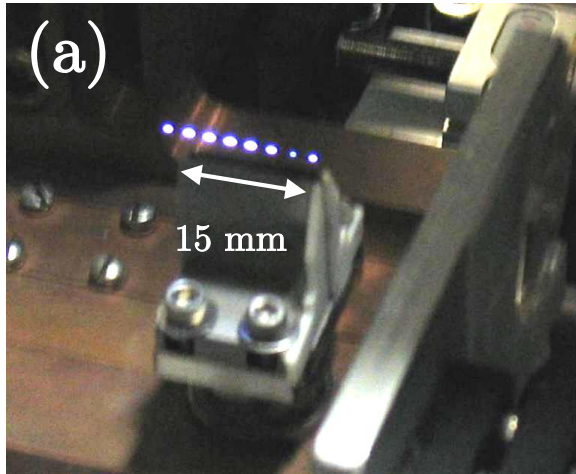
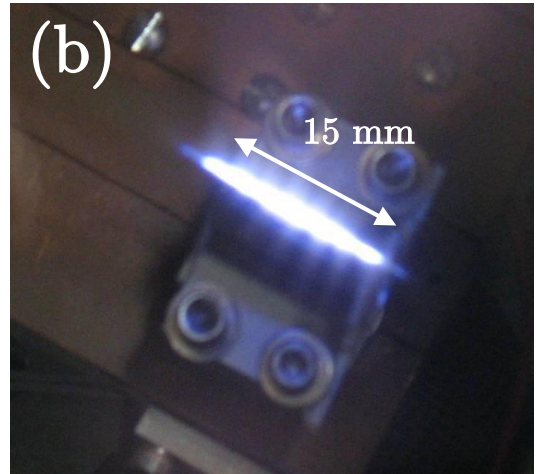


Figure 4.7: Transverse images of plasma channels with a 35 μm modulation period imposed using a ring grating a 10 μm radial ruling period. An axicon-focused Nd:YAG laser pulse (500 mJ, 100 ps, 1064 nm) was brought to focus in atmosphere (a) and in a uniform elongated argon cluster jet (b). Both images were taken using a transverse 60 fs Ti:sapphire probe pulse, where (a) is a raw shadowgram and (b) is the extracted phase from an interferogram.



Breakdown in atmosphere



Breakdown in Argon clusters

Figure 4.8: Photographs of channels with a ~ 2 mm modulation period, generated in atmosphere (a) and an axially uniform elongated argon cluster jet (b). The modulations were imposed upon the channel using a ring grating with a ~ 0.6 mm radial period in the path of the axicon-focused Nd:YAG laser pulse (500 mJ, 100 ps, 1064 nm).

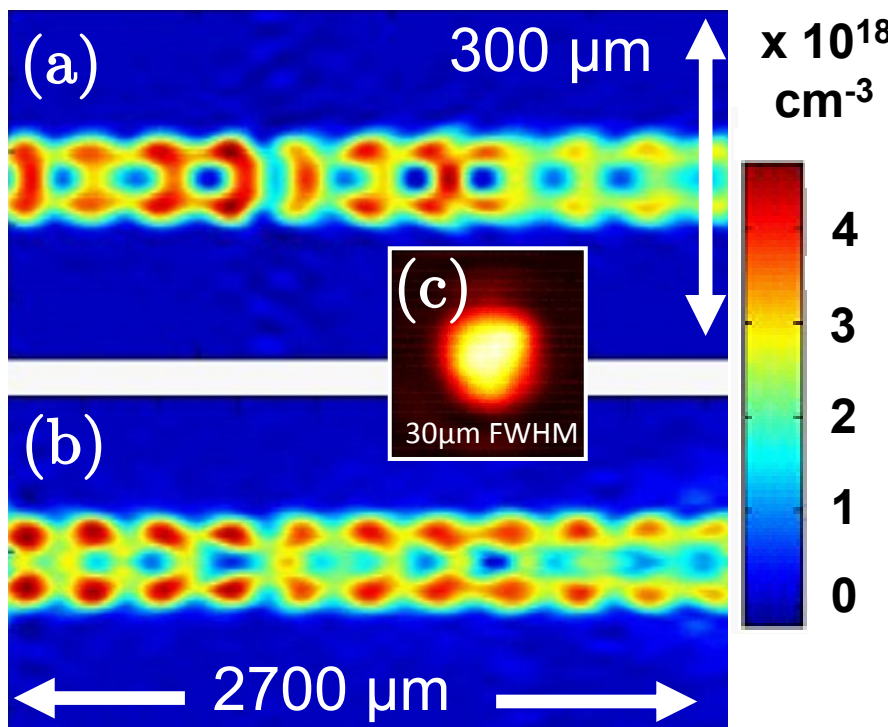


Figure 4.9: Abel-inverted radial electron density images of corrugated plasma channels made with a ring grating imaged to a hydrogen cluster jet (800 psi backing, -145° Celsius). 3 mm section of channel with (bottom panel (b)) and without (top panel (a)) a right-to-left propagating guided femtosecond pulse (70 mJ, 60 fs, 800 nm) injected 1 ns after channel formation. Exit mode from the bottom panel of (a) inset, 30 μm FWHM (c).

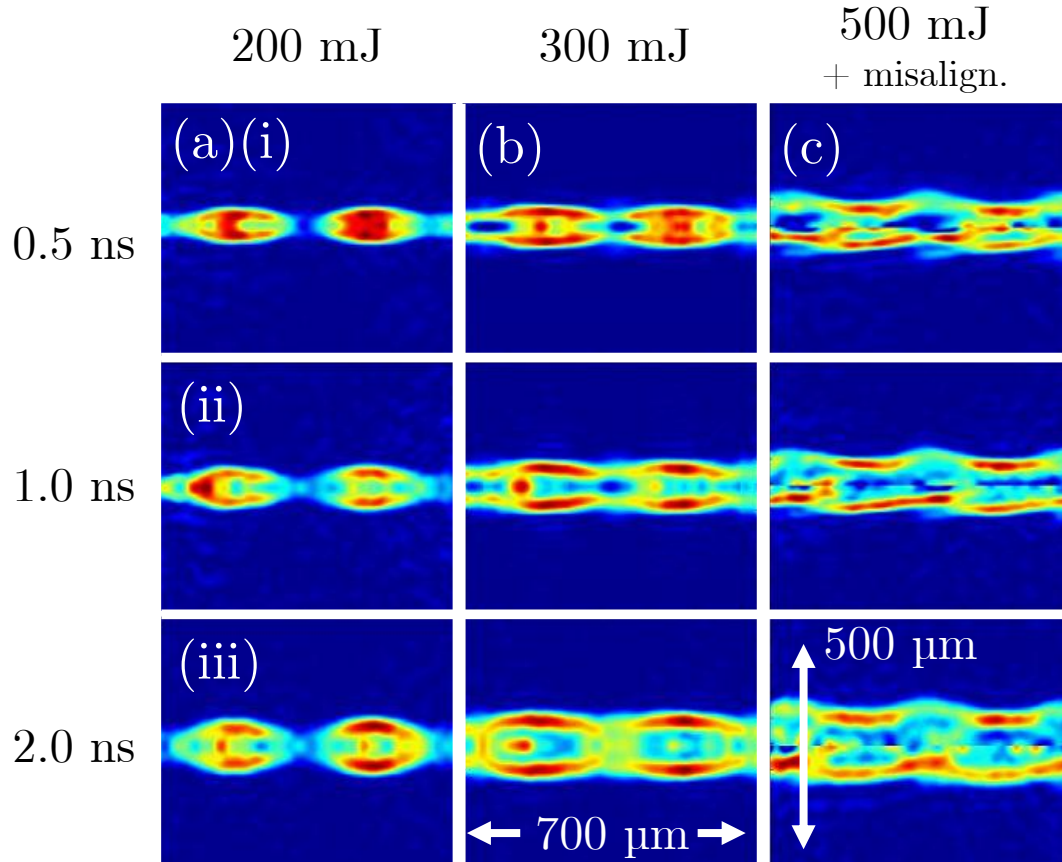


Figure 4.10: Abel-inverted radial electron density images of corrugated plasma channels made with a ring grating imaged to a hydrogen cluster jet (800 psi backing, -145° Celsius). Detail images of two periods of hydrogen plasma channels, for using 100 ps Nd:YAG laser pulse energies of (a) 200 mJ, (b) 300 mJ and (c) 500 mJ (with slight RG misalignment with respect to axicon), with interferometer probe delays, top to bottom, of 0.5 (i), 1.0 (ii) and 2.0 ns (iii).

4.2.4 Hydrogen plasma RG modulated waveguides

Results for a corrugated hydrogen plasma waveguide are shown in Figures 4.9 and 4.10. Hydrogen plasma is an attractive medium for laser-plasma acceleration [20, 85] because it is easy to fully ionize during formation, avoiding the prospect of refractive defocusing and pulse distortion that could be caused by further ionization. The modulation period of $330 \mu\text{m}$ was chosen because it ensured clearly observable periodic oscillations in plasma channel density. Figure 4.9 shows the electron density $N_e(r, z)$ of a 3 mm section near the entrance of a 15 mm hydrogen waveguide 1 ns after the arrival of the axicon-focused 100 ps pulse, immediately before (a) and after (b) guiding of a high-intensity femtosecond pulse. Figure 4.9(c) shows a guided mode imaged from the exit with $30 \mu\text{m}$ FWHM. The similarity in density profiles of the injected (b) and uninjected (a) waveguides shows that the guided pulse has little effect on the guide. Energy throughput in these hydrogen guides is approximately 10%, yielding output intensity of 10^{17} W/cm^2 . Leakage and side scattering out of the guide due to the modulations are the primary cause of this low throughput. This side leakage is observed in argon results presented later in this section (Figures 4.11 and 4.12).

Higher magnification pictures of a two-period section of the guide are shown in Figure 4.10 for 100 ps pulse energies of (a) 200 mJ, (b) 300 mJ and (c) 500 mJ as a function of interferometer probe pulse delays 0.5, 1, and 2 ns in rows (i), (ii) and (iii) respectively. It is seen in (a) that using a less energetic axicon-focused pulse can produce periodic ‘beads’ of plasma, separated by zones of neutral clusters

and atoms, while (b) shows that using more pulse energy results in a continuous ionization, which is desirable to avoid ionization-induced defocusing of the guided pulse. The beads in (a) act as a series of plasma lenslets, collecting the light emerging from each gap and re-focusing it to the next gap. Figure 4.10(c) shows the result of an intentional misalignment at 500 mJ of the Bessel beam axis and the RG optical axis: a continuous plasma fiber is generated with angular fluting. In this case, owing to the top-bottom asymmetry in the extracted phase image, separate Abel inversions were performed above and below the optical axis.

4.2.5 Argon plasma RG modulated waveguides

Modulated waveguides with higher average ionization Z were generated in clustered argon. An extended region is shown at 1.5 ns delay in Figure 4.11(a) with and without guided pulse injection (bottom and top panels, respectively) 10 ps before and after the guided pulse leaves the frame. The guided pulse has little effect on the preformed plasma waveguide, but a significant electron density ‘halo’ appears approximately 100 μm outside the channel wall. Sequences of probe images taken at increasing probe delays show that the halo propagates right to left at the speed of light with the guided pulse. The halo’s radial location remains constant over the full 15 mm length of the waveguide, but the initial density of the halo continuously drops with propagation distance from the entrance of the guide. This suggests that it is caused by a portion of the guided pulse leaking through the walls of the waveguide that ionizes neutral clusters around the periphery of the

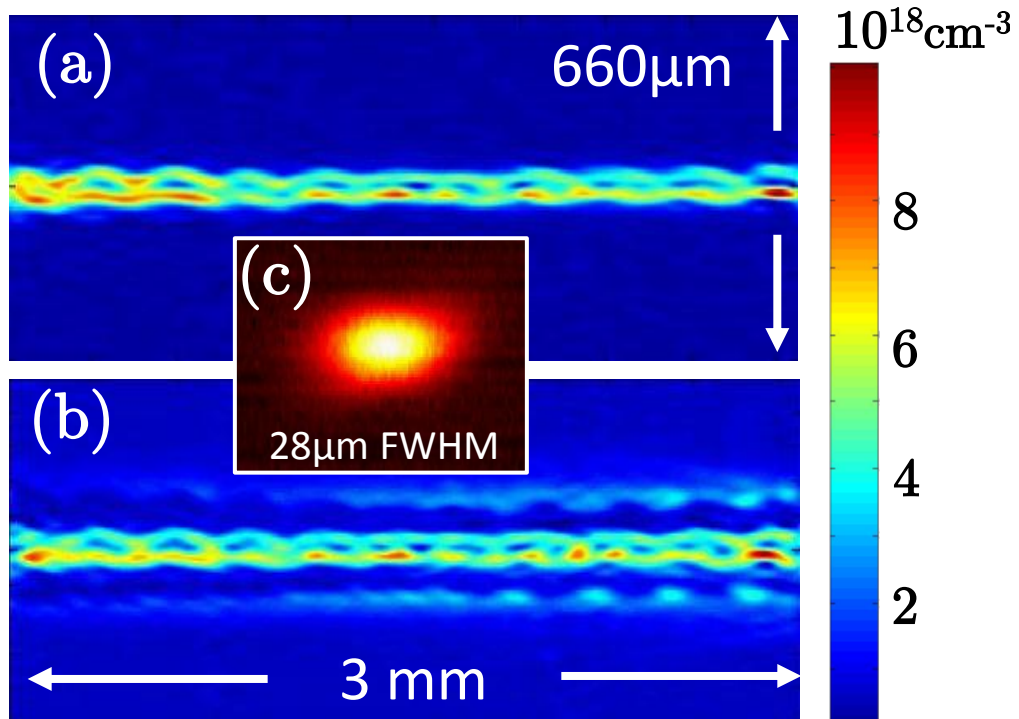


Figure 4.11: Extended Abel-inverted radial electron density images of corrugated plasma channels made with a ring grating imaged to an argon cluster jet with a $330 \mu\text{m}$ axial period (800 psi backing, 22° Celsius). 3 mm section of channel with (bottom panel (b)) and without (top panel (a)) a right-to-left propagating guided Ti:sapphire pulse (70 mJ, 60 fs, 800 nm) injected 1.5 ns after channel formation. (c) Lowest order exit mode from (b), with an average FWHM of $28 \mu\text{m}$ (c). The vertical FWHM of (c) is $26 \mu\text{m}$ and the horizontal FWHM is $30 \mu\text{m}$.

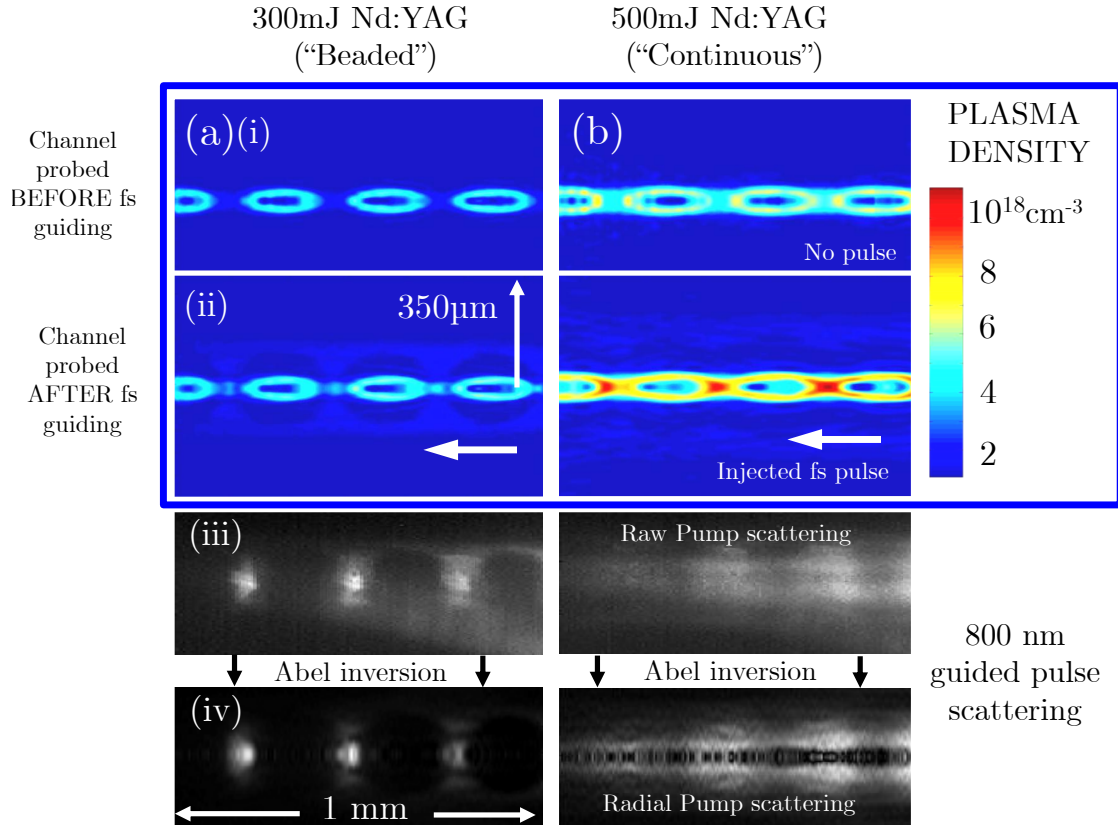


Figure 4.12: Plasma channels modulated by a ring grating in an argon cluster jet at 800 psi backing pressure and room temperature. Magnified images at 2 ns delay of beaded (300 mJ pump, (a)) and more continuous (500 mJ pump, (b)) modulations. Left and right columns: (i) density profile of uninjected waveguide, (ii) density profile of injected waveguide, raw (iii) and Abel-inverted (iv) scattering image at 800 nm corresponding to (ii).

channel [103], rather than by a portion of the driving femtosecond pulse that failed to couple into the channel at the entrance and continued to propagate outside of the channel. Note that although no halo is observed around the hydrogen plasma channels, the hydrogen clusters in these experiments are smaller and more weakly bound together, so it is unlikely they can survive so close to the channel after its formation.

Higher resolution images of modulations near the center of argon cluster channels are shown in Figure 4.12, revealing in the left column (*a*) that using a less energetic axicon-focused pulse (300 mJ) can produce periodic ‘beads’ of plasma separated by zones of neutral clusters and atoms, while the right column (*b*) shows that using more pulse energy (500 mJ) results in continuous ionization. Rows (*i*) and (*ii*) show the plasma channels before and after the passage of the intense guided femtosecond pulse. It can be seen that the beads in column (*a*) act as a series of plasma lenslets, collecting the light emerging from each gap and re-focusing it to the next gap. Strong additional ionization by the guided pulse is observed in the initially neutral gaps of the channels in column (*a*) as the beam is focused and collected by successive segments. Both the beaded and continuous channels in row (*ii*) show in more detail the ionization halo seen in Figure 4.11(*b*) induced by leakage of the guided pulse through the walls of the channel.

Remarkably, the guided energy throughput of the channel is still $\sim 10\%$, showing that the plasma lenslets can recapture the guided pulse with reasonable efficiency. Throughput for continuous channels made with more 100 ps energy is $\sim 20\%$, yielding a peak intensity of 2×10^{17} W/cm² at the beam waist, based on the fact that

the exit mode of the channel is measured at a guide bulge. This peak guided intensity was limited by available pulse energy in the femtosecond laser system. For comparison, throughput at this injection delay in an unmodulated waveguide is $\sim 60\%$.

Thomson-Rayleigh scattering of guided 800 nm light was transversely imaged through the same optics used to record probe images is shown before (Figure 4.12, row (iii)) and after (row (iv)) Abel inversion. These scattering images are dominated by regions where there was no measurable plasma density prior to the arrival of the guided pulse, making it clear that the dominant scatterers are likely ionizing clusters and atoms that either survived in the gaps between beads or in between bulges of the continuous guide.

4.3 Wire obstruction modulations

Our second method for producing modulated plasma channels uses an axially uniform channel generating beam focused upon a modulated cluster target, an example of which shown in Figure 4.13. We accomplish this modulation of the target by stretching thin wires with periodic separation across the orifice of our standard 15 mm by 1 mm elongated cluster source nozzle, parallel to the 1 mm dimension. This array of wires disrupts the cluster jet at regular intervals, allowing the formation of a modulated waveguide with a uniform axicon-focused 100 ps laser pulse.

Wire Obstruction Modulated Waveguide Layout

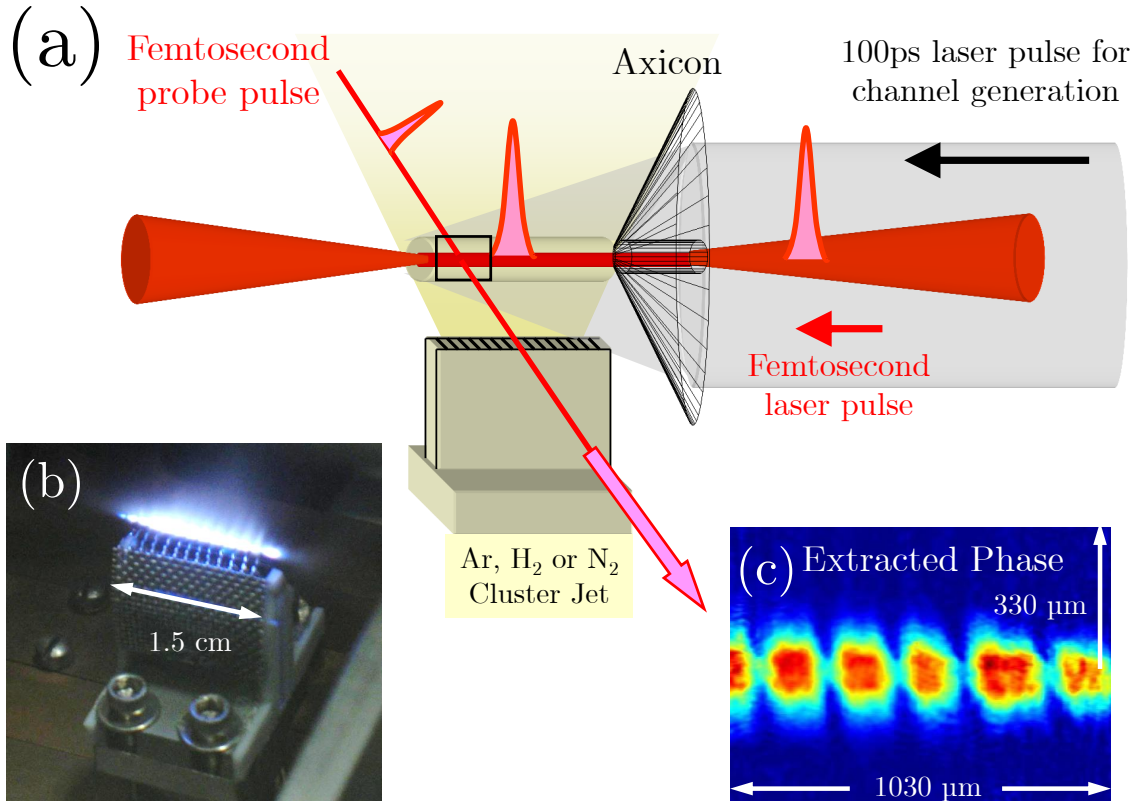


Figure 4.13: Experimental setup for waveguides modulated with cluster jet obstructions. A Nd:YAG laser pulse (200 – 500 mJ, 100 ps, 1064 nm) is brought to a line focus with an axicon, overfilling an elongated cluster jet target with periodic obstructions, making a 15 mm corrugated plasma channel. A Ti:sapphire laser pulse (70 mJ, 60 fs, 800 nm) is focused to the entrance of the guide through a hole in the axis of the axicon, guiding with electronically adjustable delay. A < 1 mJ portion of this fs pulse was used to probe the channel transversely, then sent through a folded wavefront Michelson interferometer. (b) Photograph of channel with an array of 250 μm wires with 1 mm spacing and (c) an extracted phase image of channel with 25 μm wires at a 200 μm modulation period, both in room temperature argon cluster targets.

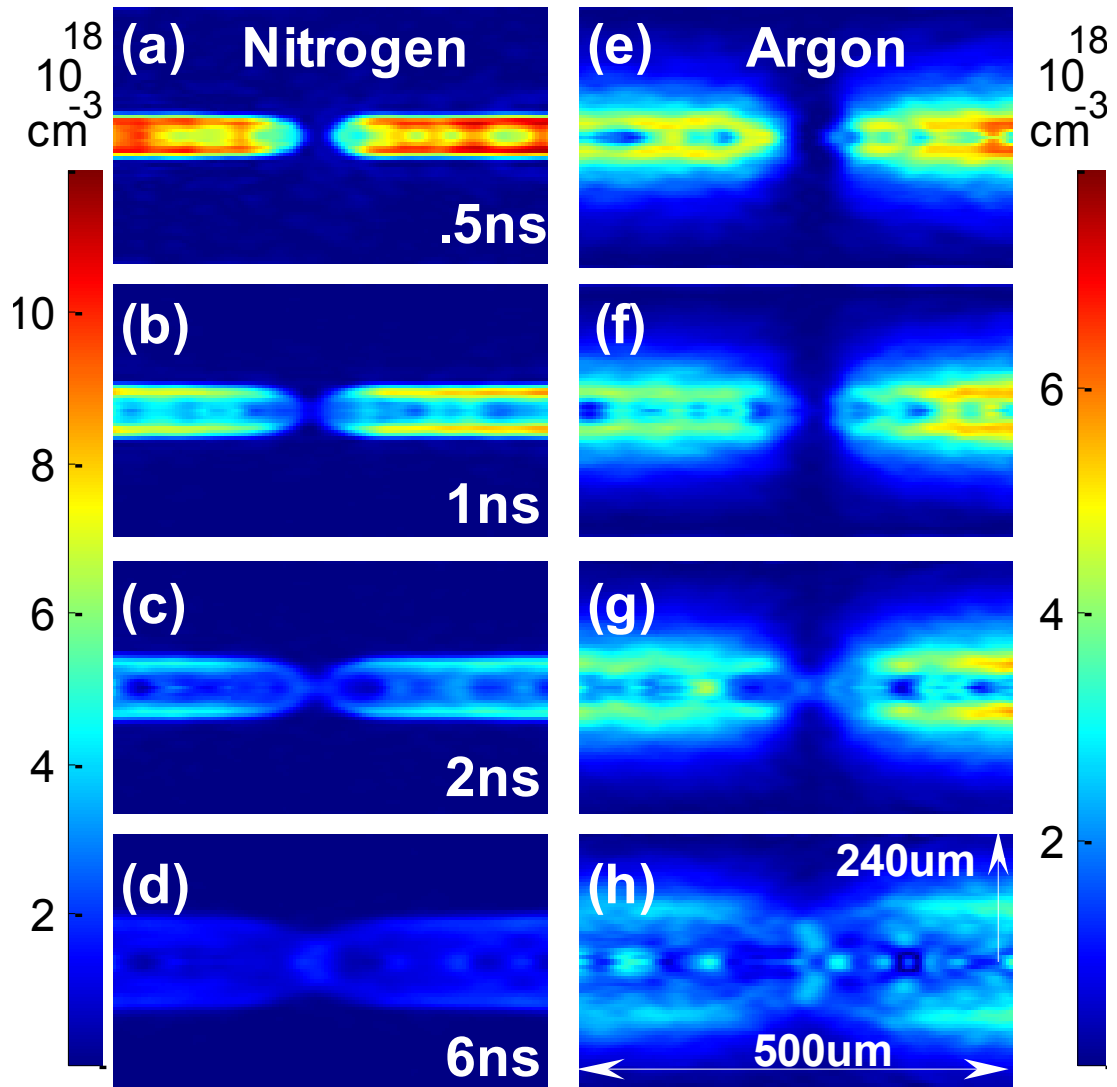


Figure 4.14: Abel-inverted radial electron density images of a single break in a plasma waveguide as a function of delay, produced with a Nd:YAG pulse (1064 nm, 500 mJ, 100 ps) in 800 psi nitrogen (*a–d*) and argon (*e–h*) cluster jets at -145° and 22° Celsius, respectively. The gap in the channel was caused by a $25\ \mu\text{m}$ diameter wire across the exit of the elongated nozzle. The wire is in contact with the nozzle, $\sim 2\ \text{mm}$ below the channel.

4.3.1 Single wire obstructions

Initial experiments examined the effects upon the plasma waveguide of a single 25 μm diameter tungsten wire stretched across the short dimension of our gas valve nozzle. We observed the temporal evolution of the waveguide in the neighborhood of the wire using the same transverse interferometry setup used in the ring grating channel experiments. Abel-inverted radial electron density images $N_e(r, z)$ in Figure 4.14 show that this obstruction in the cluster flow causes a gap in the plasma column with an initial width of $\sim 50 \mu\text{m}$. This gap remains remarkably sharp and well defined as the plasma column expands radially and axially, as the gaps between sections of the waveguide shrink and eventually disappear after 6 ns of expansion, for the full useful life of the waveguide.

These images show that the primary effect of a single wire positioned over the nozzle exit is to cast a localized downstream ‘shadow’ in the cluster flow. Subsequent guiding experiments, to be discussed shortly, showed that this shadow is a manifestation of the absence of clusters, and hence any appreciable plasma. The mean free path for inter-cluster collisions with our jet parameters [42] is $\lambda_{cluster} = (N\sigma)^{-1} \approx 1 \text{ mm}$, where $N \approx 10^{13} \text{ cm}^{-3}$ is the cluster density and $\sigma \approx 1.5 \times 10^{-12} \text{ cm}^2$ is the hard sphere collisional cross section for a 70 Å cluster [42]. $\lambda_{cluster}$ is much larger than the wire diameters in these experiments, so the cluster encounter with the wire is almost purely ballistic. Cluster collisions with the wire are of sufficient energy to disintegrate them, and the resulting low density accumulation of monomers near the wire might impede the ballistic flow of massive clusters, although the magnitude of

this effect has not been assessed. It is seen in Figure 4.14 that the edges and gaps in the nitrogen channels are significantly sharper than those seen in the argon channels. We attribute this to the larger number of available ionization stages in argon, which allow electron density profiles to vary spatially over a larger extent.

The effect of 50, 100, and 250 μm wire obstructions upon the channel was also investigated, and it was found that the break widths in the plasma channel increased with wire diameter (for example, a 300 μm gap for a 250 μm wire). Smaller diameter wires led to sharper gaps. It is likely that gaps less than 50 μm can be achieved, but wires smaller than 25 μm were too fragile to mount with the manual winding method used in these experiments. Note that like the corrugated channels generated with ring gratings, wire-modulated plasma channels are highly stable and reproducible. All density profiles shown in this paper are extracted from the average phase of 200 consecutive interferograms, with a shot-to-shot extracted density variation of less than 5%.

4.3.2 Arrays of wire obstructions

For this method to be usable for the particle acceleration and coherent light generation applications requiring quasi-phase matching that were discussed in Chapter 3, a sequence of appropriately located breaks in the plasma channel must be imposed with an array of regularly spaced wires. The first array constructed consisted of 250 μm wires with 1 mm periodicity, seen in figure 4.13(b). 25 μm wires with ~ 200 μm spacing were then used, which produced argon and nitrogen plasma

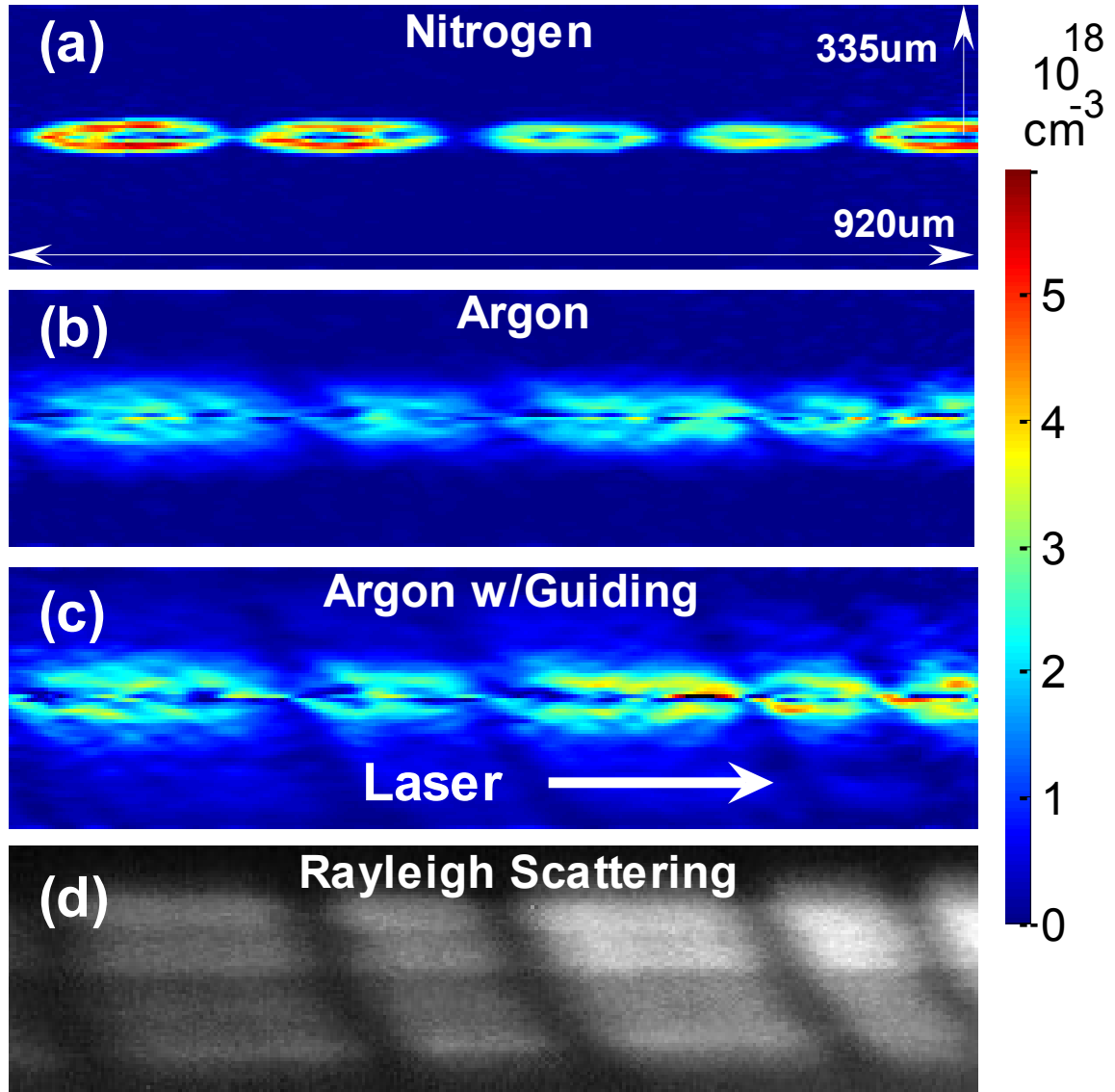


Figure 4.15: Waveguides with multiple wire obstructions at the nozzle exit. Abel-inverted radial electron density profile 2 ns after channel generation in (a) a nitrogen cluster jet (800 psi, -145° Celsius) and (b) an argon cluster jet (800 psi, -85° Celsius), both with $25 \mu\text{m}$ diameter wire obstructions at a $200 \mu\text{m}$ period. (c) shows a channel made using the same parameters as (b) but with a Ti:sapphire laser pulse (70 mJ, 60 fs, 800 nm) guided from right to left. In (d) Rayleigh scattering of the guided pulse in (c) is imaged by blocking the probe pulse and placing an 800 nm interference filter in the imaging setup.

waveguides (Figures 4.15(a) and 4.15(b)) with local radial electron density profiles and temporal evolution similar to those observed with single wires. We observed a suppression of peak local plasma density where the wires in the hand-wound array were more closely spaced, possibly also reflecting the effect of monomer interference with cluster flow.

Any electron density in the gaps of the channels is below the sensitivity of the transverse interferometer, a clear indication that there were little to no clusters in that region of the target. However, based on unguided channel images alone, the gaps could still contain significant unclustered gas density, because the 100 ps Bessel beam may not cause detectable ionization in the unclustered gas densities of our jet. A 70 mJ, 60 fs, 800 nm Ti:sapphire laser pulse was then guided in an argon channel, shown in radial electron density images taken from probe pulses before (Figure 4.15(b)) and after (Figure 4.15(c)) passage of the guided pulse. After the high intensity pulse propagated through the gaps there was virtually no change in plasma density. Given the ion stage of the plasma and the $\sim 10^{17} \text{ cm}^{-3}$ threshold phase shift sensitivity of the probe in our optical interferometry setup, the gas atom density in the gaps must therefore be $\sim 10^{16} \text{ cm}^{-3}$, assuming ionization of order $10\times$. An examination of the scattered light from the guided pulse (Figure 4.15(d)) corroborates this conclusion of negligible atom density in the gaps. Note that the slanted gap shadows seen in figures 4.15(c) and 4.15(d) can be attributed to the local direction of the flow from the cluster nozzle near that section of the wire grid.

Also seen in Figure 4.15(c) is the halo of plasma density appearing outside the walls of the plasma waveguide also observed in the RG modulated channels in Figure

4.12. The halo is present only with passage of the guided femtosecond pulse, as also observed in the corrugated channels formed with RGs. We attribute this plasma halo to leakage of the guided pulse through the walls of the modulated channel, and subsequent scattering/absorption by ionized clusters in the peripheral region around the channel. There is no such further ionization in the regions adjacent to the gaps, reinforcing the conclusion that there are no clusters present in the wire shadows. Figure 4.15(*d*) shows Rayleigh scattering of the femtosecond pulse guided in the channel shown in figure 4.15(*c*). As was the case for the RG modulated channel, femtosecond light impinging upon ionized clusters was the primary source of Rayleigh scattering, which in the channel shown in figure 4.15(*c*) only occurred after leakage reached ionized clusters outside channel walls.

Chapter 5

Nitrogen cluster plasma EUV generation

In this Chapter, we present results from experiments in which a nitrogen cluster jet from a cryogenically cooled gas valve was irradiated with femtosecond laser pulses of peak reduced vector potential up to $a_0 = 0.97$ (2×10^{18} W/cm², $\lambda_0 = 800$ nm). The original purpose of these experiments was to create a nitrogen soft x-ray laser on the $2p_{3/2} \rightarrow 1s_{1/2}$ ($\lambda = 24.779$ Å) and $2p_{1/2} \rightarrow 1s_{1/2}$ ($\lambda = 24.785$ Å) Lyman α transitions in hydrogen-like nitrogen (N⁶⁺). Although no gain was observed, the process of EUV emission from these laser-irradiated nitrogen clusters is rich in physics.

This x-ray laser scheme attempted is a transient, recombination-pumped 3-level laser with severe pumping requirements — more than 50% of an ensemble of N⁶⁺ ions must be in the upper laser level to achieve a population inversion because the lower level of the lasing transition is the ground state of the ion. To achieve this, a majority of the nitrogen atoms must first be fully ionized, then recombination must occur on a timescale shorter than the radiative lifetime of the upper state (886.3 fs for the $2p_{3/2}$ and $2p_{1/2}$ levels in H-like nitrogen) so that large upper level populations can be established before a significant fraction of H-like ions in the ground state is built up.

This requires the recombination to be predominantly 3-body (collisional) with

little 2-body (radiative) recombination, because 3-body recombination preferentially captures electrons to outer excited states of the ion (with a rate $\propto n^4$, where n is the principal quantum number), while 2-body primarily captures electrons to the innermost unoccupied energy levels of the ion, for reasons discussed in Chapter 1. The ratio of the 3-body to 2-body recombination rates scales $\propto N_e T^{-3.83}$ (obtained by dividing the rates given in Chapter 1), so colder, denser plasmas are required.

The transient scheme being attempted in this dissertation must be distinguished from quasi-steady state x-ray laser schemes, in which stimulated emission can occur repeatedly from a given ion in the gain medium as the upper state of the lasing transition is continuously re-populated. For example, one of the first soft x-ray laser schemes to be theoretically explored [145] and experimentally demonstrated [146] ($3p \rightarrow 3s$ transitions in Ne-like Se and Y) used quasi-steady state collisional electron excitation. In this Ne-like scheme, electron-ion collisions in a plasma excite bound electrons which decay to the metastable upper state. The lifetime of the laser upper level is much longer than the lifetime of the lower level, and electron-ion collisions are sufficiently frequent to re-populate the upper level after stimulated depletion to the lower laser level and decay to the ground state. In contrast, the scheme proposed here in H-like nitrogen utilizes a transient population inversion mechanism, in which the plasma is rapidly heated more quickly than the relaxation rate of the excited states.

There have been previous theoretical and experimental studies attempting development of a transient soft x-ray laser on this transition using recombination pumping in a plasma generated by optical field ionization (OFI) of a gas with a

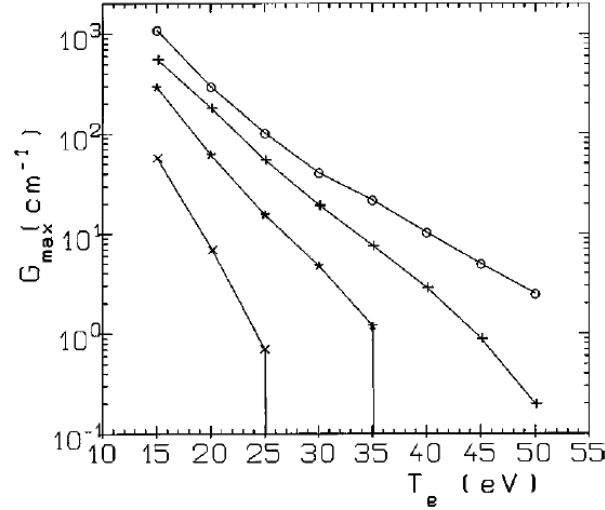


FIG. 8. Maximum local gain of the $2p_{3/2} \rightarrow 1s_{1/2}$ transition ($\lambda = 24.78 \text{ \AA}$) as a function of the temperature for several densities: $6 \times 10^{20} \text{ cm}^{-3}$ (\circ), $5 \times 10^{20} \text{ cm}^{-3}$ ($+$), $4 \times 10^{20} \text{ cm}^{-3}$ (\star), $3 \times 10^{20} \text{ cm}^{-3}$ (\times).

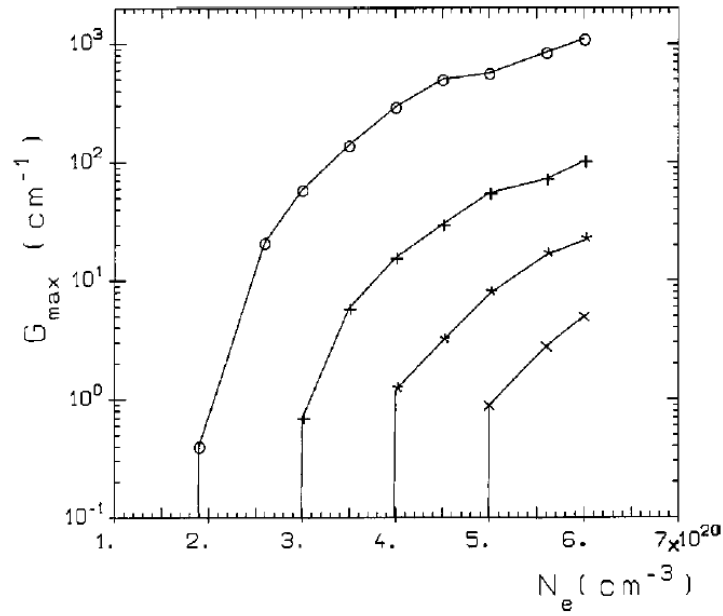


FIG. 9. Maximum local gain of the $2p_{3/2} \rightarrow 1s_{1/2}$ transition ($\lambda = 24.78 \text{ \AA}$) as a function of the density for several temperatures: 15 eV (\circ), 25 eV ($+$), 35 eV (\star), 45 eV (\times).

Figure 5.1: Figures reproduced from reference [147] showing calculated maximum transient local gain coefficients G_{max} for the $2p_{3/2} \rightarrow 1s_{1/2}$ transition in uniform, fully ionized nitrogen plasmas as a function of electron density and temperature.

femtosecond laser, including some that exclusively consider nitrogen plasmas [147, 148]. First, 2-dimensional PIC simulations were performed to determine the laser and target parameters required to create a fully stripped nitrogen plasma via OFI, then hydrodynamic simulations were run to investigate the time-dependent behavior of the temperature and density as the plasma expands and cools after the passage of the laser pulse. Transient local gain coefficients are also calculated, and are reproduced in Figure 5.1.

These calculations indicated that in a fully ionized nitrogen plasma, after the passage of the femtosecond pulse, an electron density and temperature of $> 3 \times 10^{20}$ cm^{-3} and < 50 eV are required to obtain a population inversion on the $2 \rightarrow 1$ transition in H-like nitrogen [147], as shown in Figure 5.1. For an electron density and temperature of 6×10^{20} cm^{-3} and 15 eV, G_{max} values of 1100 and 400 cm^{-1} are predicted for the $2p_{3/2} \rightarrow 1s_{1/2}$ and $2p_{1/2} \rightarrow 1s_{1/2}$ Lyman α transitions, respectively. This peak local gain occurred approximately 400 fs after the peak of the pump pulse, and then fell to zero after < 1 ps. Note that this is roughly the same timescale as the 886.3 fs lifetime of the upper state found by taking the inverse of the Einstein A coefficient.

Simulation results for an assortment of initial electron temperatures and densities (reproduced in Figure 5.1) indicated that the scaling of the maximum local gain coefficient G_{max} is proportional to $N_e^3 \exp(-k_B T_e)$ [147]. In the hydrodynamically expanding plasma columns created via OFI of a gas considered in these simulations, the electron density and temperature were essentially static during the subpicosecond timescale over which transient gain is predicted. Although this is not

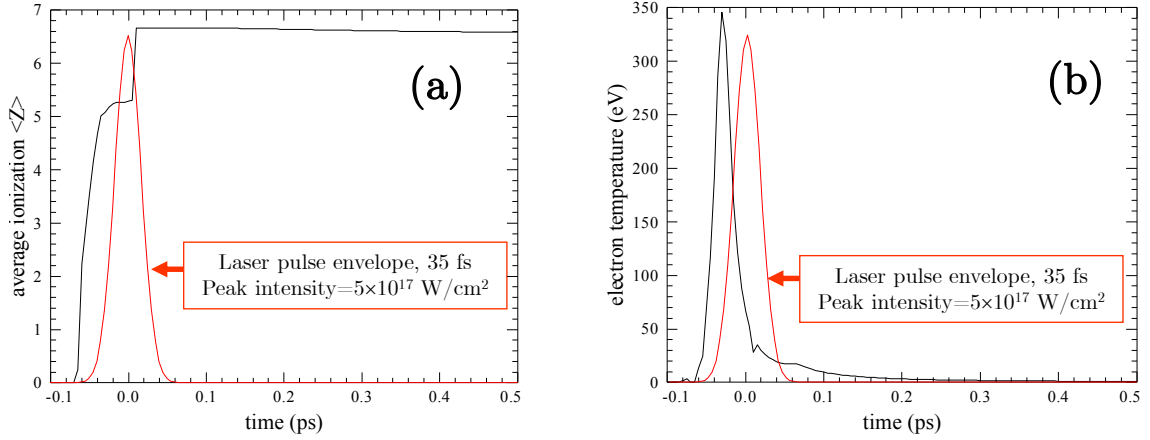


Figure 5.2: Plots of average ionization (a) and peak electron temperature (b) from a 1D hydrodynamic simulation [62] of the explosion of a 25 nm radius nitrogen cluster irradiated by a Ti:sapphire laser with peak intensity of 5×10^{17} W/cm² and pulsewidth of 35 fs.

the case for exploding laser-irradiated clusters, which explode on a subpicosecond timescale [63], the simulation results reproduced in Figure 5.1 should still provide a rough guide for the G_{max} values that might be expected for similar electron densities and temperatures within an exploding laser-irradiated cluster.

This theory was followed by experiments [148] in which a 10 TW Ti:sapphire femtosecond laser was focused in a jet of nitrogen gas with peak intensity of $\sim 10^{19}$ W/cm², producing plasma with an electron density of up to 10^{20} cm⁻³ via OFI, but no amplification was observed. This was attributed to the high initial electron temperatures of ~ 400 eV, resulting from heating of the plasma due to Raman excitation, driving plasma waves [148].

The experiments described in this Chapter attempted to use the unique prop-

erties of laser-irradiated clusters to create the dense, cold, fully stripped plasma for which gain is predicted. Simulations performed with a 1D hydrodynamic code [62] show that when a 35 fs Ti:sapphire laser pulse with peak intensity of 5×10^{17} W/cm² ionizes and heats a nitrogen cluster with a radius of 25 nm, a plasma is created that quickly reaches an average ionization $\langle Z \rangle > 6.5$ (Figure 5.2(a)), the first prerequisite for a population inversion. At the same time, the peak electron temperature within the nanoplasma drops to < 10 eV less than 100 femtoseconds after the passage of the pulse (Figure 5.2(b)), while the electron density is still $> 10^{21}$ cm⁻³, creating ideal conditions for gain according to the simulation results from reference [147] in Figure 5.1. These laser and cluster parameters are easily within the capabilities of our 25 TW laser system and cryogenically cooled gas valve.

However, the laser intensity used in these runs approaches the upper limit of the regime in which this code is applicable, as the code does not incorporate relativistic effects and this intensity corresponds to a reduced vector potential $a_0 \simeq 0.5$. Additionally, use of a fluid code assumes that the oscillation amplitude of free electrons quivering in the laser field is much less than the the diameter of the cluster. For this intensity, the quiver excursion amplitude $x_{\text{osc}} = \frac{eE}{m_e\omega^2} = 62$ nm (ignoring relativistic corrections). This exceeds the limits where the hydrocode is valid, but these simulation results are used to gain physical insight into the cluster heating and explosion dynamics.

Based on the cluster explosion velocities seen in these 1D simulations ($\sim 5 \times 10^7$ cm/s), the clusters merge into a uniform plasma with an electron density of $< 10^{20}$ cm⁻³ approximately 5 ps after the peak of the pump pulse. This merging time is

longer for higher intensity laser intensity laser pulses and larger cluster sizes for fixed average atom densities, but was always between 1 and 10 ps for the parameter range explored in these experiments. The average ionization $\langle Z \rangle$ shows relatively slow decline over the 500 fs window of the simulation, which indicates that recombination may not take place quickly enough to create a population inversion before the clusters merge. However, these initial simulation results were still sufficiently promising to motivate experiments.

5.1 Experimental setup

To study EUV emission from laser-produced nitrogen plasmas, we irradiated a jet of clusters in vacuum with a 25 TW peak power Ti:sapphire femtosecond laser. The cluster size and average density within the jet were independently controlled by changing the backing pressure and temperature of a gas valve. The 15 mm by 1 mm elongated nozzle of the gas valve could be variably oriented with respect to the incoming laser, resulting in a cluster jet target between 1 and 15 mm thick. To minimize propagation effects due to strong absorption of the laser pulse by clusters, most EUV spectral data was collected using a 1 mm thick cluster target. The energy and pulsewidth of the femtosecond laser pulses were controlled using a half wave plate/ thin film polarizer pair and the compressor grating spacing, respectively. The cryogenically cooled gas valve and femtosecond laser are described in detail in Chapter 2. This interaction takes place in the vacuum system described in Appendix A.

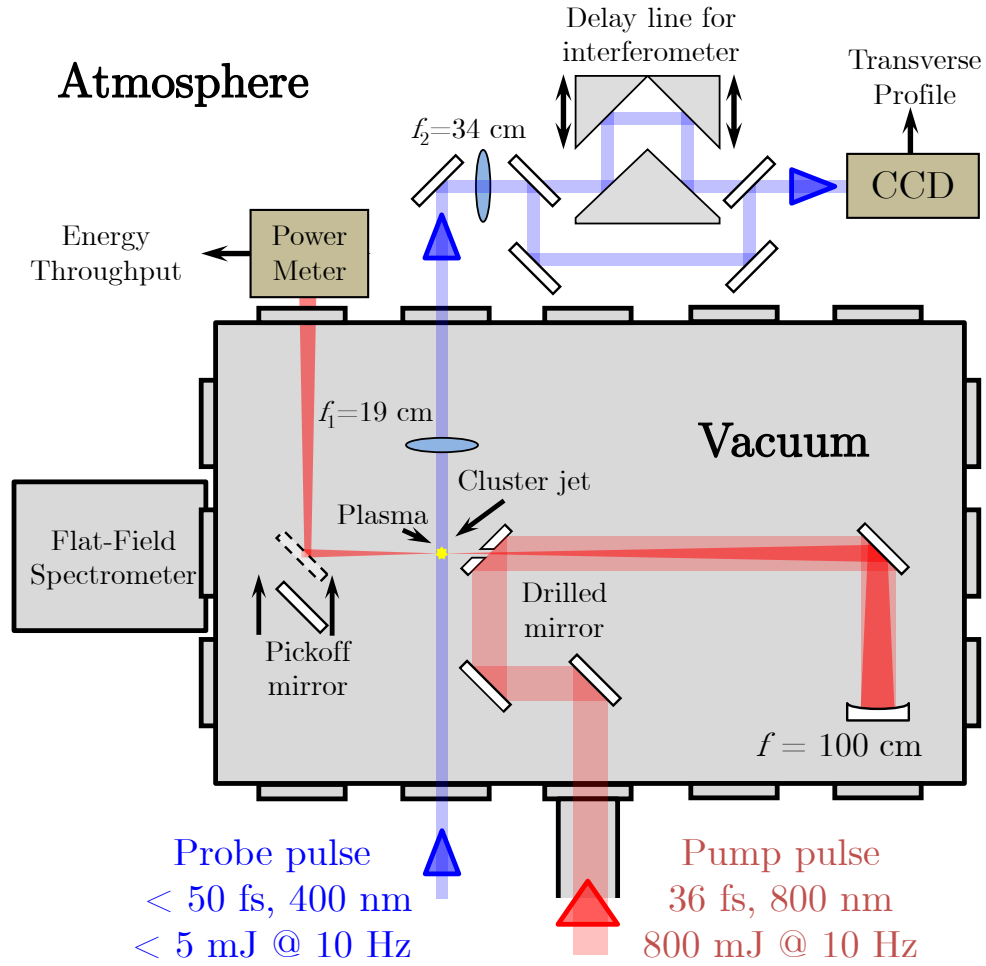


Figure 5.3: Experimental layout for the generation of laser-produced plasmas in a nitrogen cluster jet. A Ti:sapphire laser pulse (up to 830 mJ, 36 fs, 800 nm) is focused using a dielectric concave spherical mirror ($f = 1$ m) in a retro-reflecting geometry through a 4 mm diameter hole in a 45° turning mirror. Transverse profiles of the plasma and cluster jet (interferograms and shadowgrams) were gathered by sending a frequency-doubled probe pulse through an interferometer into a CCD camera. Energy throughput measurements were collected by moving a pickoff mirror on a motorized stage into the beam path of the laser after the focus. A flat-field spectrometer collected EUV spectra (1.5 – 20 nm, see Appendix B)

The laser was brought to focus by retro-reflecting the beam off a dielectric concave spherical mirror with a focal length $f = 1$ m through a 4 mm hole drilled in an 45° turning mirror (Figure 5.3). This focused the beam at $f/25$ to a Gaussian spot with FWHM of $34.6 \mu\text{m}$ in the X and $23.4 \mu\text{m}$ in the Y dimension (Figure 5.4). This corresponds to an average $1/e^2$ radius of $w_0 = 12.3 \mu\text{m}$ and a confocal parameter of $b = 1.2$ mm, longer than the 1 mm thickness of the cluster jet. When operated at minimum pulsewidth (36 fs FWHM) and maximum energy (830 mJ) the laser reaches a maximum peak intensity of $1.8 \times 10^{18} \text{ W/cm}^2$ at the focus in this weakly focusing configuration.

EUV light in the $15 - 200 \text{ \AA}$ wavelength range emitted by the nitrogen plasma was collected at a repetition rate of up to 10 Hz (the maximum repetition rate of the laser) by the flat-field spectrometer described in Appendix B. The acceptance cone of the spectrometer was oriented towards the plasma along the axis of the driving femtosecond laser and residual laser light was blocked from the spectrometer using thin metal filters that transmit EUV (Al, Zr or Ni with thicknesses from $0.1 - 0.8 \mu\text{m}$). Reducing the repetition rate of the laser extends the usable lifetime of the metal filters, which were eventually punctured by the laser. These thin metal filters allowed single-shot observation of emission lines from hydrogen-like, helium-like and lithium-like nitrogen, which will be described in detail later in this Chapter. The $\sim 0.05 - 0.20 \text{ \AA}$ spectral resolution of the spectrometer was limited by the CCD pixel size.

Radial and axial profiles of plasma and neutral gas density were obtained using a frequency-doubled transverse probe pulse (Figure 5.3). The probe pulse ($<$

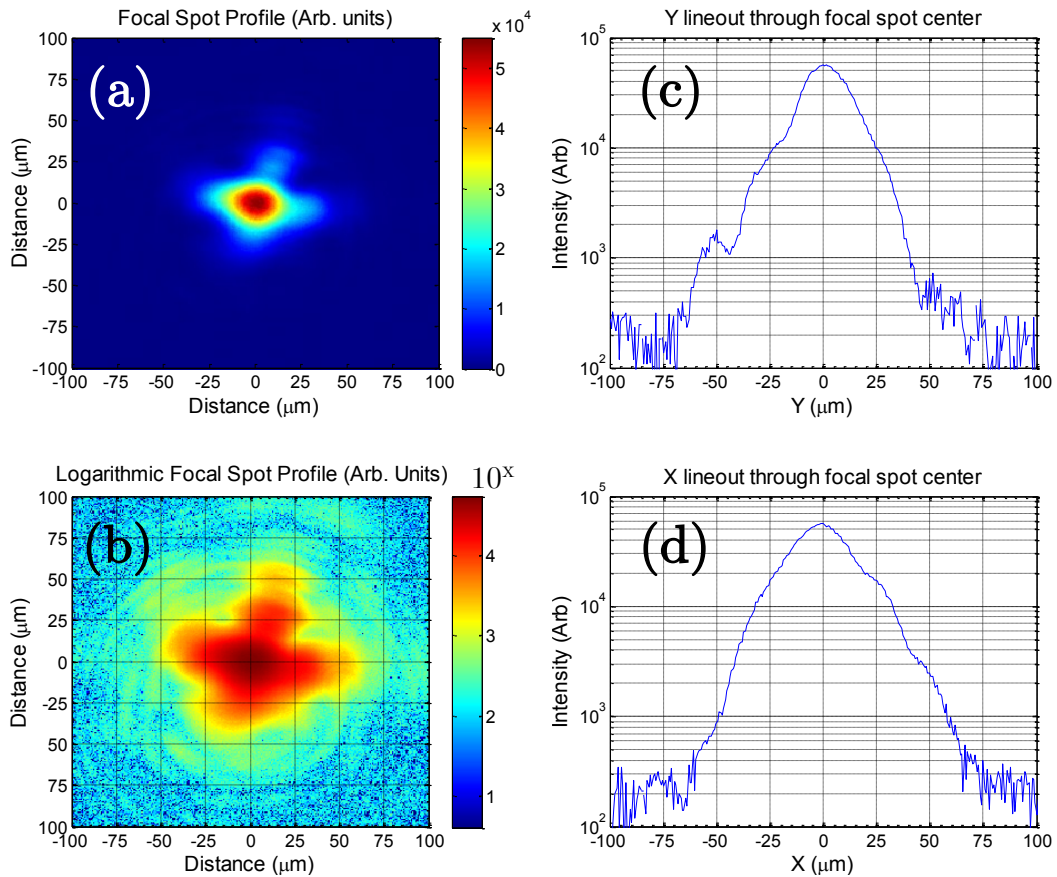


Figure 5.4: Focal spot profile of the Ti:sapphire laser focused with the $f = 1$ m concave mirror in the setup shown in Figure 5.3. This profile was directly obtained using a CCD camera and $10\times$ magnification microscope objective, and displayed using a (a) standard and (b) logarithmic intensity colormap. Plots (c) and (d) show Y ($23.4 \mu\text{m}$ FWHM) and X ($34.6 \mu\text{m}$ FWHM) lineouts through the focus, respectively. 69% of the beam energy is contained within the central Gaussian profile.

5 mJ) was split from the main pump pulse, sent through a variable-length optical delay arm and then frequency-doubled to 400 nm. This collimated probe pulse then arrives at the interaction region in the vacuum chamber up to 1 ns prior to or 2 ns after the main pump pulse, depending on the delay arm position. When the delay is set such that the probe arrives at the cluster jet before the pump pulse and sent transversely through the plasma column, the neutral atoms in the jet impart a phase shift on a section of the probe, allowing us to measure the volume average neutral gas density. Alternatively, when the probe arrives after the pump pulse, electron density is measured.

To extract the phase shift imparted upon the probe pulse by plasma or clustered neutral gas, it is directed out of the vacuum chamber through a window into a folded wavefront interferometer, where it is split into two pulses that are spatially offset and recombined at a slight angle, resulting in interference fringes. By using the flat phase front at the edge of the beam as a reference, the phase shift resulting from plasma is encoded in the spatial phase of the fringes of an interferogram collected by a CCD camera. This image is processed by extracting the phase of the fringes, then Abel-inverting the image about the axis to obtain radial density profiles. The 800 nm pump light scattered off the clusters was blocked from the imaging system while transmitting the 400 nm probe using an interference filter. A detailed description of the algorithm used to implement the Abel inversion integral can be found in a prior dissertation from our group [144].

5.2 Neutral gas density measurements

Neutral N₂ molecule density was measured by extracting the phase shift in a 400 nm probe pulse to determine how the jet density varied as a function of gas valve temperature and backing pressure. The individual clusters are much smaller than the wavelength of the probe pulse, and cannot be resolved by the imaging setup, and the phase shift of the probe pulse will be determined exclusively by the local volume averaged molecule density, independent of the cluster size distribution. The gas valve nozzle has a rectangular 1 by 15 mm exit. This measurement was performed for two different gas valve orientations offset from one another by 90° , such that the probe propagation path is 1 mm or 15 mm long through the jet of clusters, henceforth referred to ‘side-on’ and ‘end-on’ probing, respectively.

In the 1 mm long probe path orientation (side-on), the phase shift imparted upon the probe was too small to allow consistent measurement of the absolute density. However, the phase shift observed along the width of the jet in the side-on orientation was sufficiently uniform to justify treatment of the density along the long axis of the nozzle as a 15 mm step function, and infer the 3-dimensional profile of the jet based on the profile measured in the end-on orientation, shown in Figure 5.5(a). This and all other extracted phase profiles are the average of 100 consecutive shots.

A lineout of the density profile experienced at the pump laser focus ~ 1.5 mm above the gas nozzle exit is shown in Figure 5.5(b). The nominal gas density at the laser focus is obtained by observing the value of the ~ 0.5 mm wide uniform

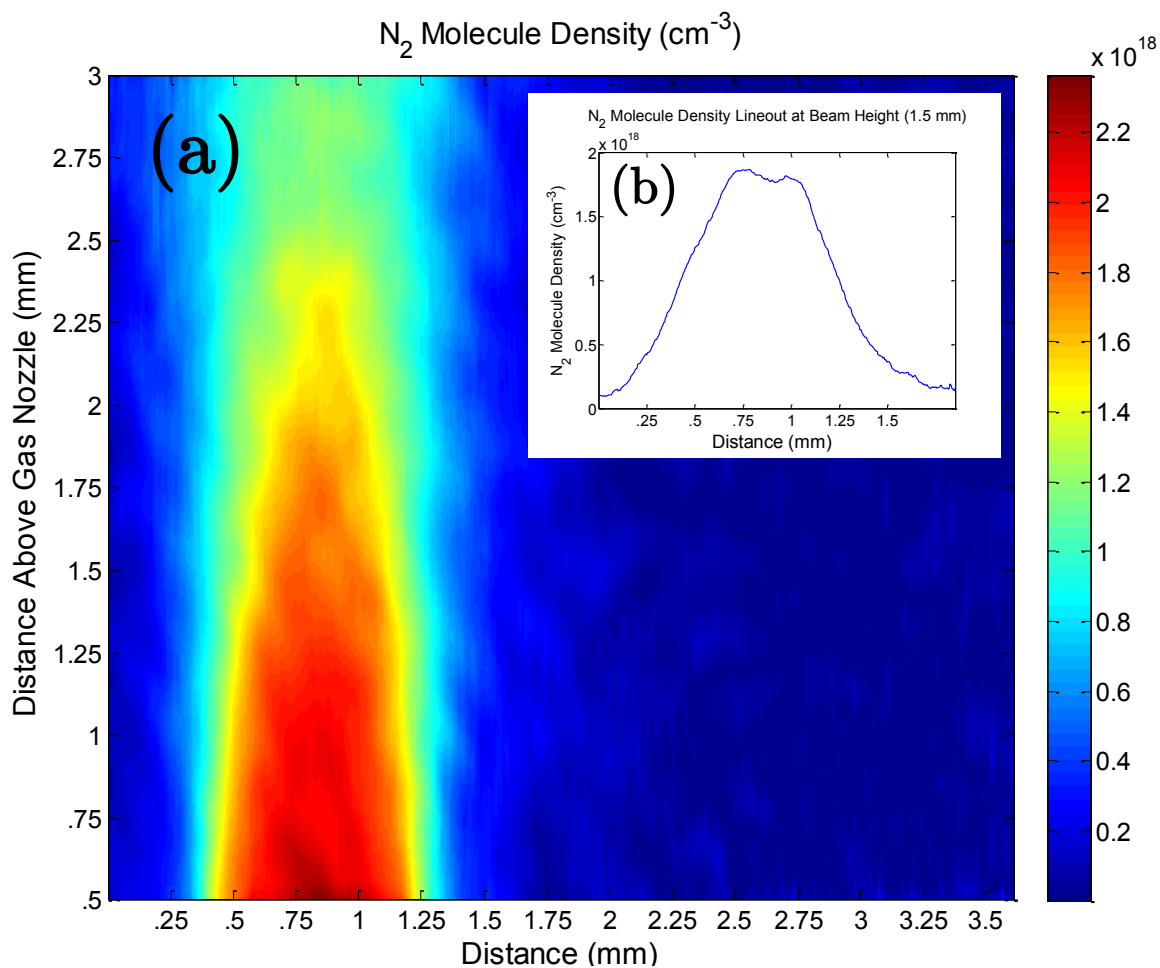


Figure 5.5: Example image (a) of N₂ molecule density extracted from a transverse interferogram when the gas valve is held at -100° Celsius with a backing pressure of 425 PSI. This cluster jet shown emerged from the 1 mm by 15 mm rectangular nozzle positioned 0.5 mm below the frame, and is flowing in the Y direction. To collect this image the probe was oriented end-on, such that it propagated through 15 mm of jet material. The inset plot (b) is a lineout of (a) at Y=1.5 mm, the height at which the pump beam strikes the jet.

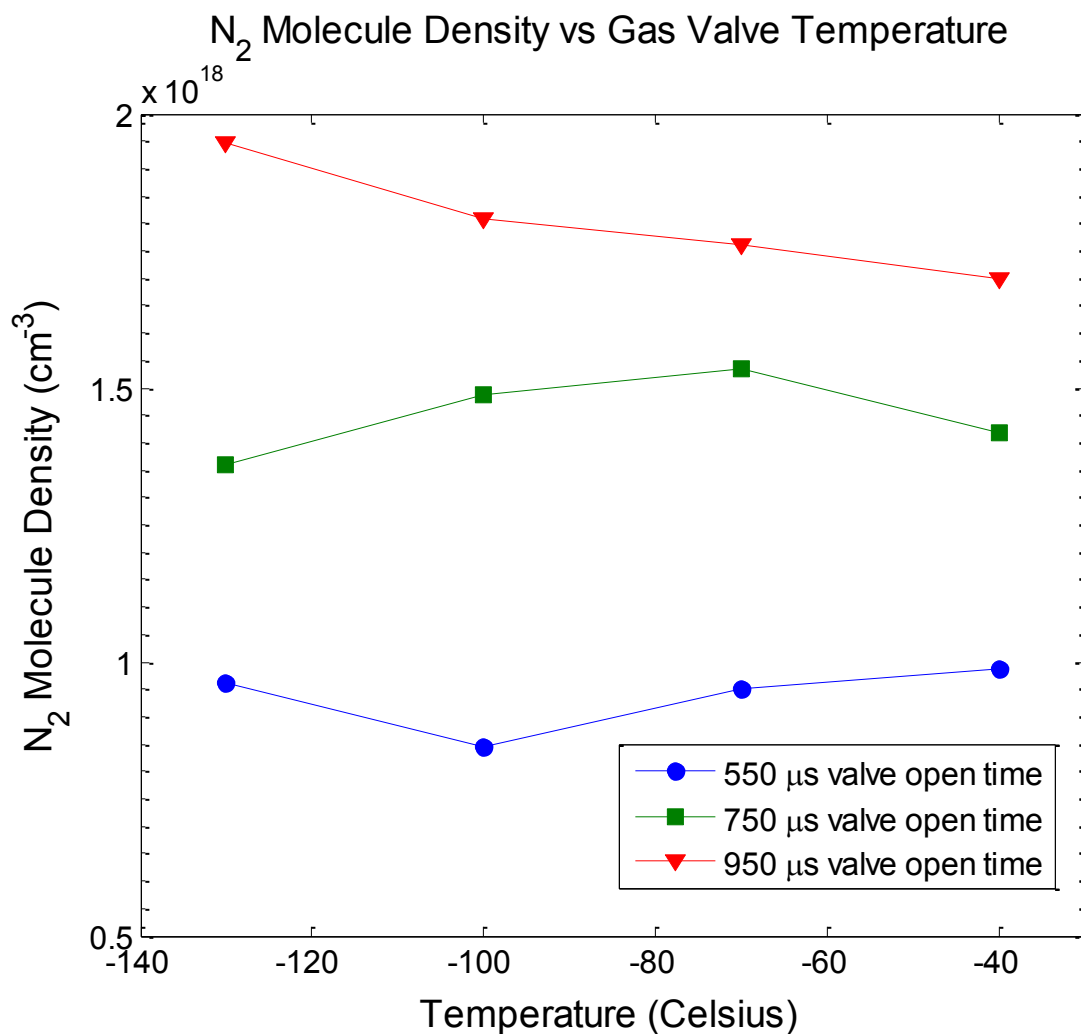


Figure 5.6: Plot demonstrating our ability to maintain reasonably constant N₂ molecule density over a wide range of gas valve temperatures. This effectively allows independent control of the mean cluster size and molecule density of the jet. Each data point is extracted from an image of the neutral N₂ molecule density similar to the one shown in Figure 5.5(a).

central peak region, 1.85×10^{18} N₂ molecules/cm³ in this case. These neutral gas measurements allowed us to verify that we were holding the N₂ molecule density constant while adjusting the temperature of the gas valve (Figure 5.6). This effectively allows independent control of the mean cluster size and atom density of the cluster jet. The scaling of the Hagena parameter predicts that larger mean cluster sizes occur at lower temperatures, and this was confirmed with measurements of the mean cluster radius \bar{a} that will be discussed in a later section.

5.3 Electron density measurements

Electron density measurements recorded using the 400 nm probe pulse 10 ps after the onset of pump-pulse-driven plasma formation. This relative timing between the pump and probe pulses was set by finding the probe pulse delay arm position for which plasma formation was seen on half of the transverse interferogram in the axial dimension, then adding 10 ps worth of path length on the probe pulse delay arm micrometer. Images and radial electron density profiles of the plasma generated by a 100 mJ, 36 fs Ti:sapphire pump pulse are shown in Figure 5.7. These conditions ((*a*) -40° , (*b*) -70° , (*c*) -100° and (*d*) -130° Celsius) correspond to the same parameters as those shown in the top line (950 μ s valve open time) in Figure 5.6, so the pump laser propagated through a 1 mm thick jet of clusters with a mean density of approximately 1.85×10^{18} N₂ molecules/cm³. The top and bottom halves of each electron density phase image were Abel-inverted independently, which is why the radial profiles are asymmetric about the axis.

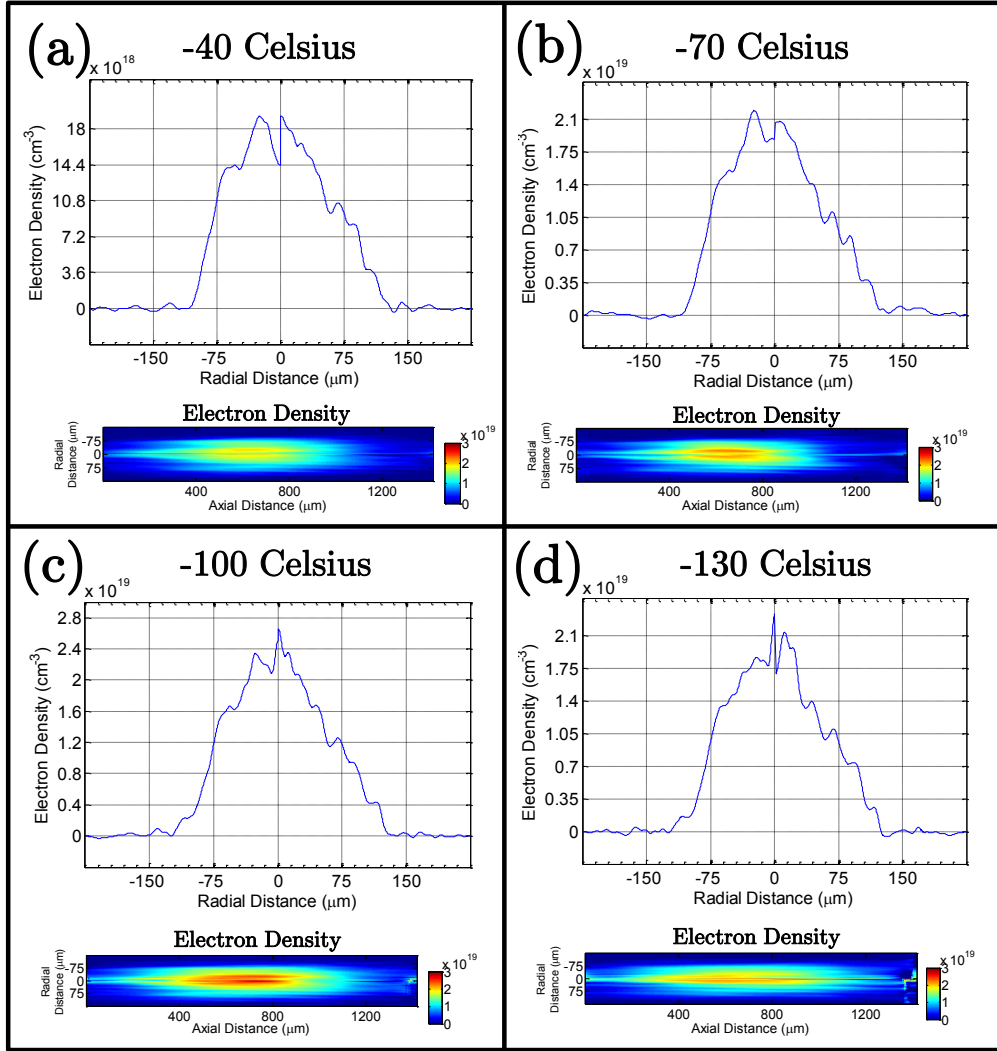


Figure 5.7: Plots showing radial lineouts (top of each frame) from electron density profile images (bottom of each frame) measured ~ 10 ps after the arrival and passage of the pump laser (100 mJ, 36 fs, 800 nm) for gas valve temperatures of (a) -40° , (b) -70° , (c) -100° and (d) -130° Celsius. The N_2 molecule density in all four cases is $\sim 1.85 \times 10^{18}$ molecules/cm³, measured in Figure 5.6. In each plot, the electron density gridlines occur at multiples of the nitrogen atom density. On the right-hand side of each plot, ‘steps’ in the electron density appear to correspond to the different ionization stages of nitrogen plasma in the wings of the focal spot (Figure 5.4).

The horizontal gridlines on the radial profiles in Figure 5.7 are drawn at integer multiples of the neutral nitrogen atom density (double the neutral nitrogen molecule density), allowing the state of ionization attained by different radial sections of the plasma to be seen. This indicates that for all four gas valve temperatures plotted, a significant fraction of the nitrogen atoms within $30 \mu\text{m}$ of the axis reach the He-like ionization stage. However, due to fluctuations in the measured electron density within $\sim 15 \mu\text{m}$ of the central axis, it is unclear based on these profiles whether or not there is significant population of H-like or fully stripped ions. Additionally, sharp ‘steps’ in electron density are seen on the right side of each extracted radial profile in Figure 5.7 that jump in integer multiples of the neutral atom density. It is likely that these steps occur at radii where the laser intensity is capable of creating successive ion species within the nitrogen clusters due to collisional ionization (focal profile shown in Figure 5.4).

One possible source of fluctuations in an Abel-inverted profile is incorrect choice of the axis of symmetry. To minimize this effect, the height and angle of the axis on each frame was found using an algorithm that minimizes the on-axis discontinuity of the Abel-inverted profile within a $10 \mu\text{m}$ radius of the axis. The discontinuities that remain are likely artifacts from the Abel inversion algorithm caused by the azimuthal nonuniformity of the plasma, because this algorithm assumes an azimuthally symmetric object. It is likely that the plasma is azimuthally nonuniform as a result of the focal spot (Figure 5.4) which deviates from a Gaussian profile in the ‘wings’ at radii greater $> 15 \mu\text{m}$. Any artifacts in the inverted profile will increase in magnitude as the axis is approached. This could explain both the

relatively strong on-axis electron density fluctuations and why the ‘step’ electron densities in the wings of the radial profiles do not always occur at exact multiples of the neutral atom density.

5.4 Cluster size measurements

To determine the mean radius \bar{a} and density n_{cl} of clusters within the jet, two types of measurements are used in conjunction — Rayleigh scattering of an end-on probe pulse (1), and transverse interferometry to measure the mean neutral gas density (2), as described in a prior section. The foundation of this all-optical technique is the fact that the Rayleigh scattering cross-section of a cluster with radius a σ_{scat} is proportional to $n_{cl}a^6$ and the phase shift $\Delta\phi$ imparted on a probe pulse in the neutral gas density measurement is proportional to $n_{cl}a^3$. This procedure has been performed previously in our group and described in detail [42, 84].

For a single cluster of radius a , the Rayleigh scattering cross section σ_{scatt} in the near-field limit $ka \ll 1$ is given by

$$\sigma_{\text{scatt}} = \frac{8\pi}{3} k^4 |\gamma|^2 = \frac{8\pi}{3} k^4 a^6 \left| \frac{\varepsilon - 1}{\varepsilon + 2} \right|^2 \quad (5.1)$$

where k is the probe laser wavenumber, $\gamma = a^3(\varepsilon - 1)/(\varepsilon + 2)$ is the cluster polarizability and ε is the dielectric function of the cluster material. For larger clusters that violate the near-field approximation, Mie terms must be incorporated into the expression for scattering cross section σ_{scatt} .

The nucleation of clusters in expanding jets of gas results in a distribution of cluster sizes. This technique does not provide information about the details of this

distribution — in practice, the ensemble average over the cluster size distribution \bar{a} is the value that can be measured. By making the additional assumption that all nitrogen atoms are contained in clusters and that no absorption of the probe by neutral atoms occurs, we see that the intensity of Rayleigh scattered light S_{Rayleigh} from a jet is given by $S_{\text{Rayleigh}} \propto n_{cl}\sigma_{\text{scat}} \propto n_{cl}\bar{a}^6$.

Measuring the phase shift $\Delta\phi$ imparted on a probe pulse by a jet of neutral clusters satisfies $\Delta\phi \propto n_{cl}\gamma \propto n_{cl}\bar{a}^3$. Taken together with S_{Rayleigh} , these two measurements allow us to solve for the average cluster radius \bar{a} and density n_{cl} . Neutral gas density images collected resembled Figure 5.5(a) and a sample Rayleigh scattering image from a cluster jet is shown in Figure 5.9(a).

The imaging setups used for this all-optical measurement had the same specifications as those used in Reference [42] and were performed in an auxiliary vacuum chamber (Figure 5.8). The only significant difference is that a 1064 nm Nd:YAG probe beam was used in the current setup, while a 532 nm probe (frequency-doubled Nd:YAG) was used previously [42]. This results in a factor of 16 reduction in scattering yield for a given cluster size (because $\sigma_{\text{scatt}} \propto k^4$), but allows the characterization of clusters that are twice as large before the near-field approximation is violated and Mie scattering terms must be accounted for.

Mean cluster radius and gas density measurements were performed as a function of gas valve temperature for a fixed mass output of 1.5×10^{18} atoms/cm³, shown in Figure 5.10(a). Axial Rayleigh scattering lineouts at select temperatures within this scan are shown in in Figure 5.9(c). This scan shows that the cluster radius increases with decreasing temperature, in qualitative agreement with the Hagena

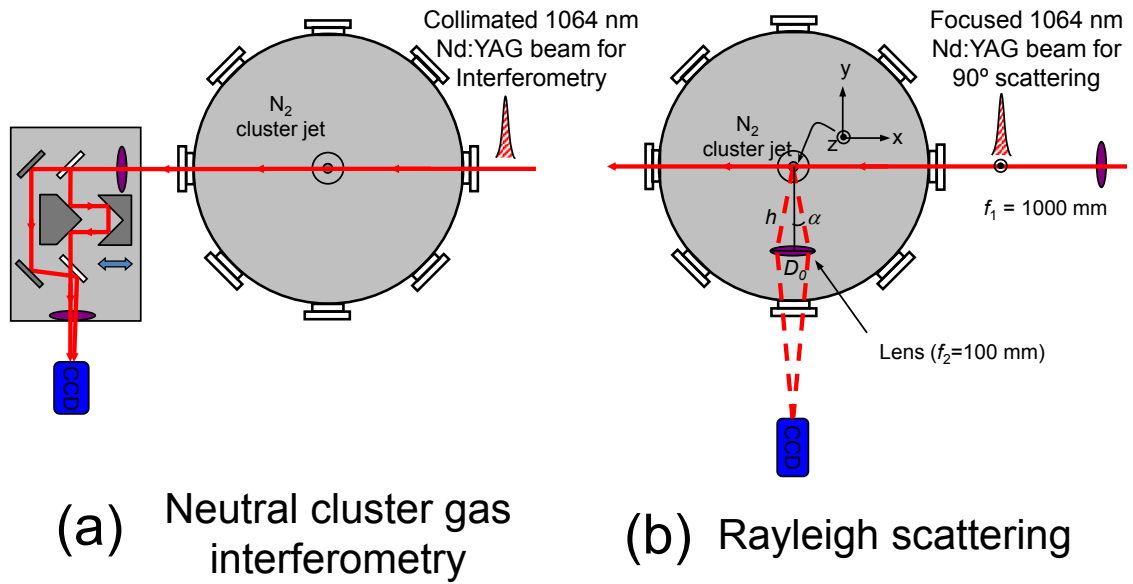


Figure 5.8: Layout of the auxiliary vacuum chamber used to measure the mean cluster size within the jet. In both the neutral gas density (*b*) and Rayleigh scattering (*b*) measurements, the probe beam propagated end-on through the jet, experiencing 15 mm of jet material. Taken together, these measurements allow us to calculate the mean cluster radius \bar{a} and mean cluster density n_{cl} in the jet.

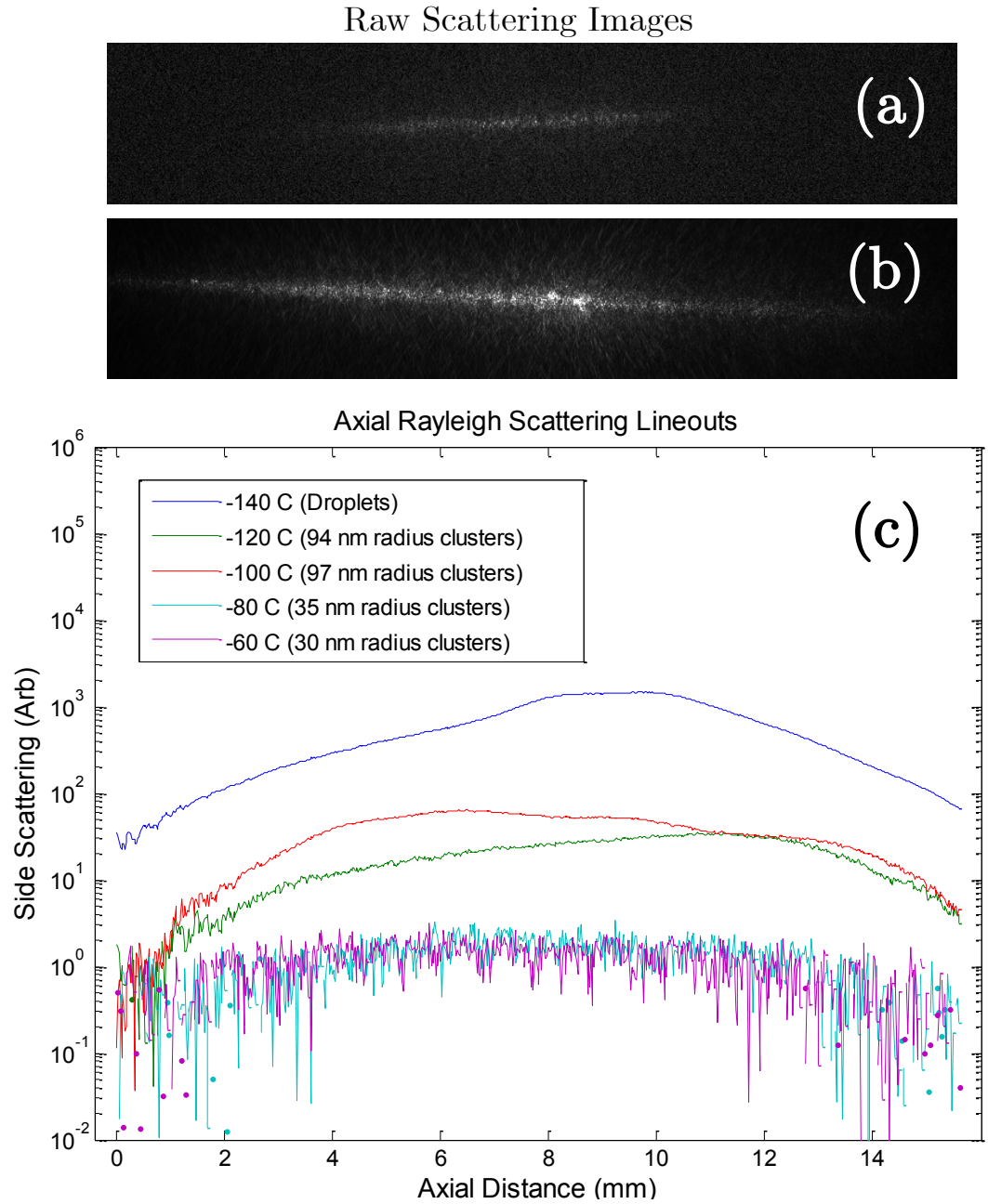


Figure 5.9: Sample raw images of 1064 nm light scattered from (a) a cluster jet (-120° Celsius gas valve temperature, mean radius $\bar{a} = 94$ nm) and (b) a droplet jet (-165° Celsius gas valve temperature). Also shown are central lineouts for various gas valve temperatures at a constant nitrogen atom density of 1.5×10^{18} cm $^{-3}$.

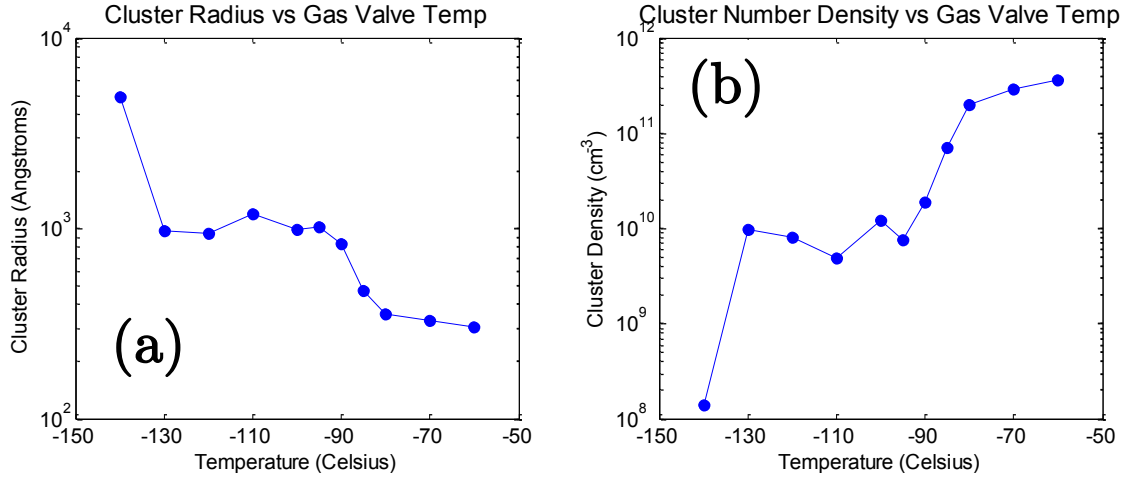


Figure 5.10: Plot showing average cluster radius \bar{a} and mean cluster density n_{cl} as a function of temperature for a constant nitrogen atom density of $1.5 \times 10^{18} \text{ cm}^{-3}$, extracted from the data shown in Figure 5.9. The data point at -140° Celsius corresponds to the onset of the droplet regime in which the aggregate diameter is of the order of the probe wavelength ($\lambda = 1064 \text{ nm}$), where an accurate measurement of cluster size would require the incorporation of Mie terms.

parameter scaling. However, as the temperature drops from -80° to -100° Celsius, there is a sharp jump in average cluster radius from 30 to 100 nm. This jump is likely caused by gas flow details specific to this nozzle.

As the temperature drops to -140° Celsius, the average radius \bar{a} jumps sharply again, to a value of 500 nm. This value underestimates the true size, because this radius is of the same order as the 1064 nm wavelength of light being used to perform the measurement. Mie terms would need to be included in the processing algorithm to account for this. An inspection of the pressure-temperature phase diagram of nitrogen overlaid with the operating regime of the gas valve (Figure 5.11) reveals

that this closely corresponds to the gas-liquid phase transition of nitrogen at the 600 PSI pressure in the gas valve reservoir. In this regime, the gas valve releases a stream of liquid that fragments into droplets with mean radii typically larger than $1 \mu\text{m}$ [50].

Although the critical point of nitrogen does not occur until -146.9° Celsius, the temperature of the gas valve in the cluster size measurement setup is likely $\sim 10^\circ$ Celsius lower than the thermocouple reading. This can be explained by a difference between the cryogenic cooling blocks used in the cluster size test chamber and the 25 TW target chamber (Figure 5.3) — the thermocouple that measures the temperature is mounted in a different location in the copper block that holds the cryogenic cooling line and gas valve, so there could be a difference in temperature reading for the same gas valve temperature. This is corroborated by a transition in EUV emission from the laser-produced plasma at $\sim -160^\circ$ Celsius that occurs at the onset of droplet formation that will be discussed in a subsequent section.

5.5 Laser energy absorption measurements

The laser energy absorbed by the cluster jet was measured by diverting the 800 nm light transmitted through the jet after focus out of the vacuum chamber with a dielectric mirror on a motorized translation stage, then measuring it with a power meter (Figure 5.3). Although a measurement of pump light scattered by the cluster jet was not performed, the beam transmitted through the cluster jet had similar diameter and divergence as a beam with the jet off. Additionally, previous

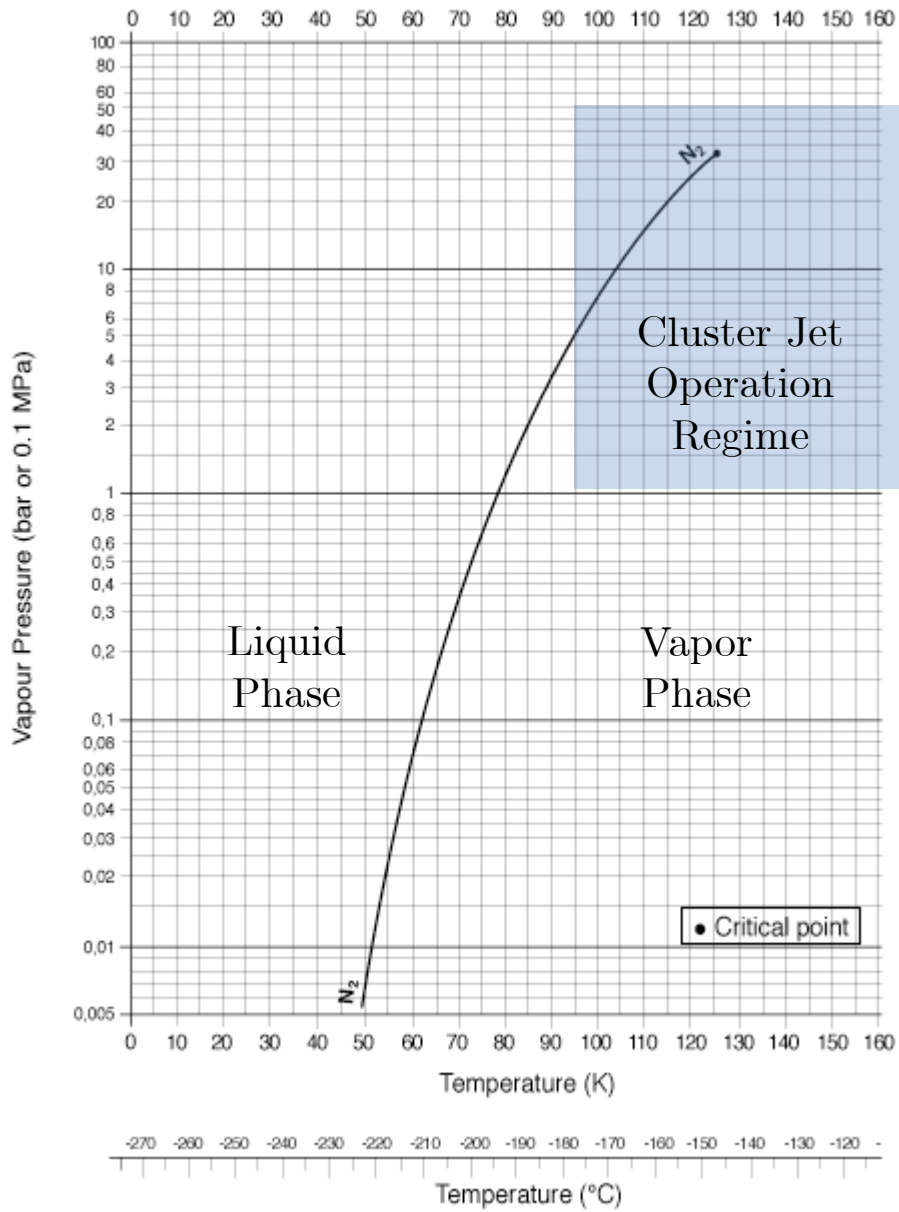


Figure 5.11: Plot showing the region within pressure-temperature phase space accessible to the gas valve overlaid upon the vapor pressure curve of nitrogen. At backing pressures below 33 bar to the left of the vapor pressure curve, the gas valve produces a stream of liquid that fragments into droplets instead of a jet of gas in which cluster nucleation occurs.

experiments under similar conditions in which the laser light scattered from a cluster jet was collected [149] have shown that a negligible fraction of the pump laser is scattered. Therefore, we can attribute the energy loss in the beam to absorption.

Figure 5.12 shows the fraction of incident laser energy absorbed by a 1 mm thick nitrogen cluster jet with an atom density of $\sim 1.5 \times 10^{18} \text{ cm}^{-3}$ as a function of laser energy for gas valve temperatures of -80° , -100° , -120° , -140° and -150° Celsius. This clearly shows that at lower temperatures (which result in larger clusters, as discussed in the previous section) a higher fraction of the incident pulse energy is absorbed by the nitrogen clusters. Higher incident laser pulse energy also results in a higher absorption fraction.

In the case of a 15 mm long cluster jet transverse electron density measurements, laser energy throughput measurements and visual inspection of the plasma showed that the laser was only able to penetrate the full 15 mm length of the cluster jet and create a uniform plasma column when the atom density was below $\sim 1 \times 10^{17}$, due to extremely efficient absorption of laser energy by the nitrogen clusters. Although up to half of the incident laser energy was transmitted through a 15 mm cluster jet with a density of 3.8×10^{17} (Figure 5.13) this resulted in a plasma column with a strong axial taper. Absorption measurements collected for several densities at -145° Celsius corroborated the observations in Figure 5.12 of a 1 mm jet, with a higher fraction of pulse energy being absorbed when higher incident beam energies were used. To minimize the axial gradients in laser intensity and plasma density, all EUV spectral data presented in this dissertation were gathered with the jet oriented such that the laser encountered a 1 mm thick sheet of clusters at focus.

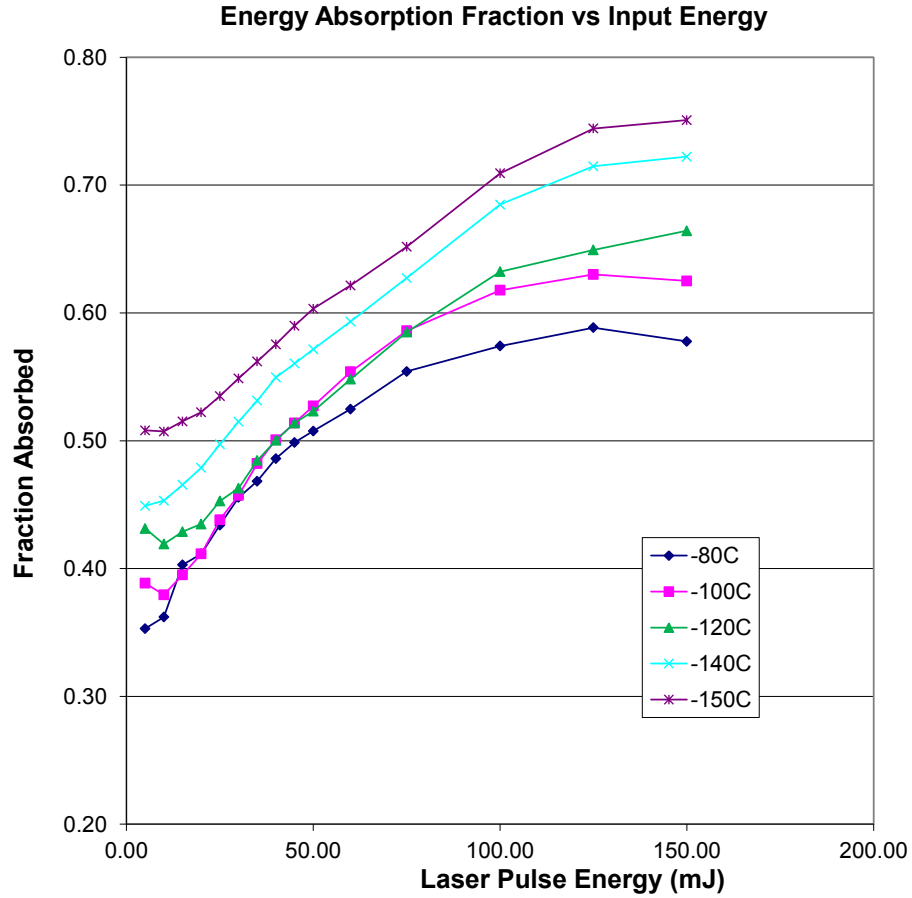


Figure 5.12: Plot showing the fraction of laser pulse energy absorbed (36 fs, 800 nm) by a 1 mm thick cluster jet as a function of laser energy for select gas valve temperatures. Nitrogen atom density is $\sim 1.5 \times 10^{18} \text{ cm}^{-3}$ for all conditions. Rayleigh scattering measurements (Figure 5.10) showed that jets with larger mean cluster radii were released from lower temperature gas valves, as predicted by the Hagena parameter scaling.

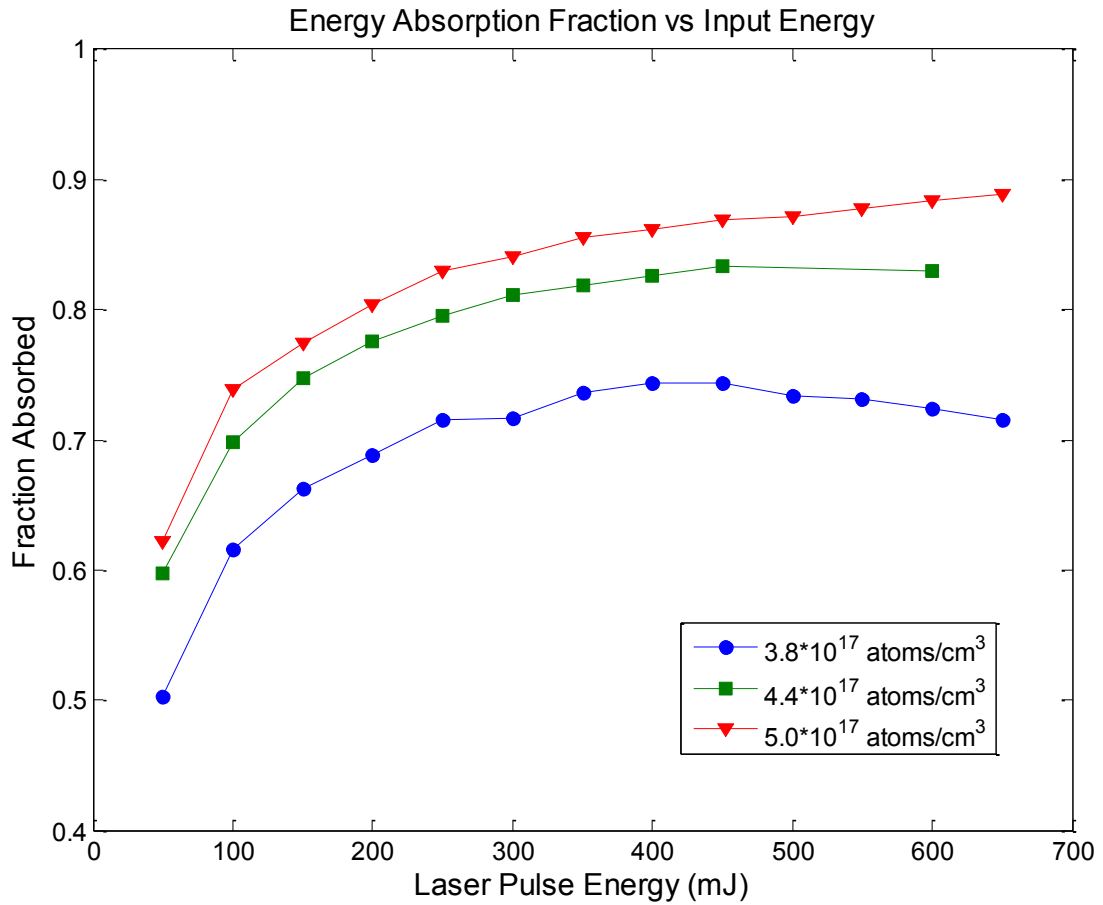


Figure 5.13: Plot showing laser pulse energy fraction absorption as a function of laser energy when the pump laser experienced a 15 mm thick cluster jet for several nitrogen atom densities, all with the gas valve held at a temperature of -145° Celsius.

5.6 Spectral Data

The flat-field EUV spectrometer described in Appendix B is capable of using two different diffraction gratings (Hitachi), both with variable line spacing. The first grating, with a central ruling density of 2400 lines/mm, is capable of observing wavelengths in the 15 – 100 Å spectral range. The second has a ruling density of 1200 lines/mm, which allows the observation of wavelengths between 50 and 200 Å. Additionally, $< 1 \mu\text{m}$ thick metal filters (Lebow Company) were installed on a filter wheel in front of the spectrometer entrance slit to block the Ti:sapphire laser light and allow the passage of EUV. By using different grating/filter combinations, emission from different spectral regions was observed.

When using the 2400 line/mm grating and a $0.2 \mu\text{m}$ Ni filter, H-like and He-like recombination lines (diffracted in the first order from the grating) were visible in the 17 – 24.8 Å and 21 – 29.6 Å spectral range, respectively, identified in the sample spectrum shown in Figure 5.14. These lines were clearly visible on the EUV spectrometer for the full range of gas jet temperatures (-173° to 23° Celsius) and backing pressures (50 to 800 PSI) used.

When the 1200 line/mm grating was installed in the spectrometer and a $0.2 \mu\text{m}$ Zr filter was used, emission lines from H-like, He-like and Li-like nitrogen were visible, and are labeled in Figures 5.15 and 5.16 (the same spectrum, displayed twice with different lines identified in each Figure for clarity). Line emission diffracted in the first order from the grating was observed from H-like (79.3 – 133.8 Å), He-like (99.5 – 136.6 Å) and Li-like (131.3 – 143.9 Å) nitrogen. Emission lines with

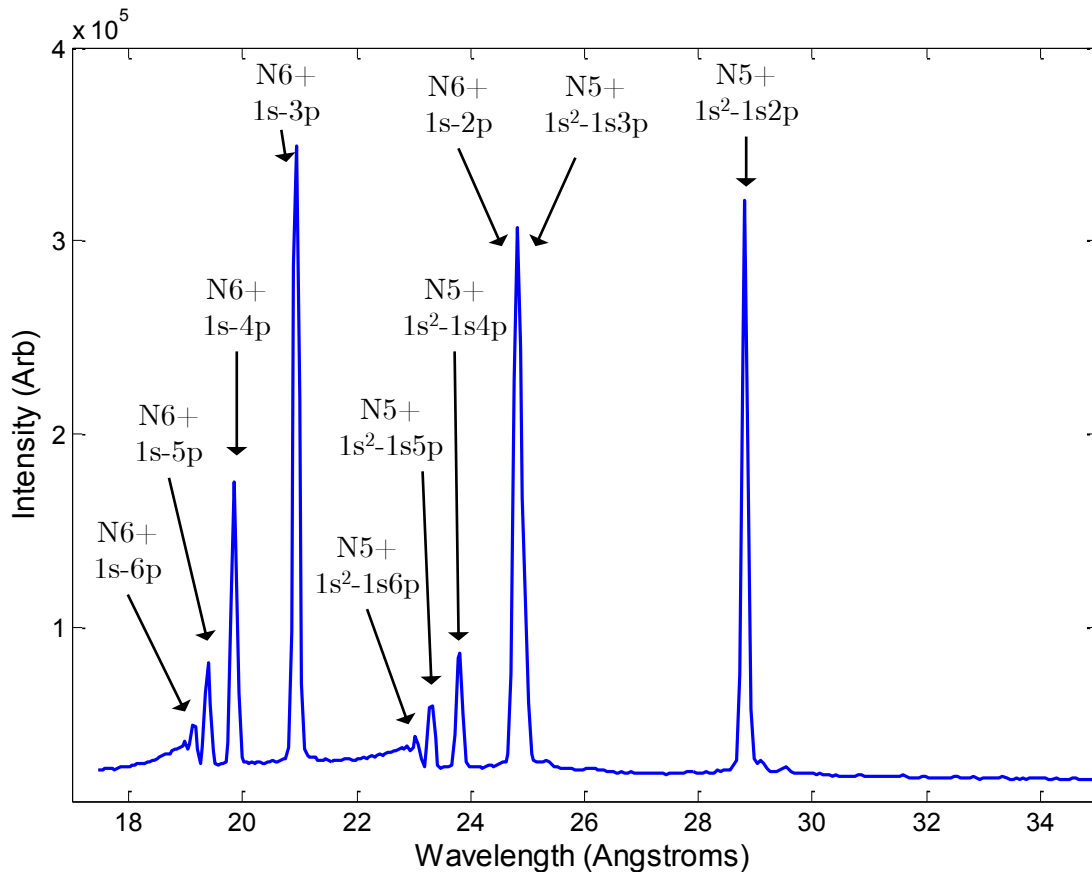


Figure 5.14: Example of a raw nitrogen spectrum recorded with the flat-field spectrometer using the 2400 line/mm grating. A 36 fs Ti:sapphire laser pulse with peak intensity of 4×10^{17} W/cm² (200 mJ/pulse) irradiated a cluster jet with an average atom density of $\sim 3 \times 10^{18}$ cm⁻³ (solenoid valve at -100° Celsius, backed by 475 PSI N₂). A thin nickel filter prevented laser light from entering the spectrometer. He-like and H-like nitrogen emission lines are visible.

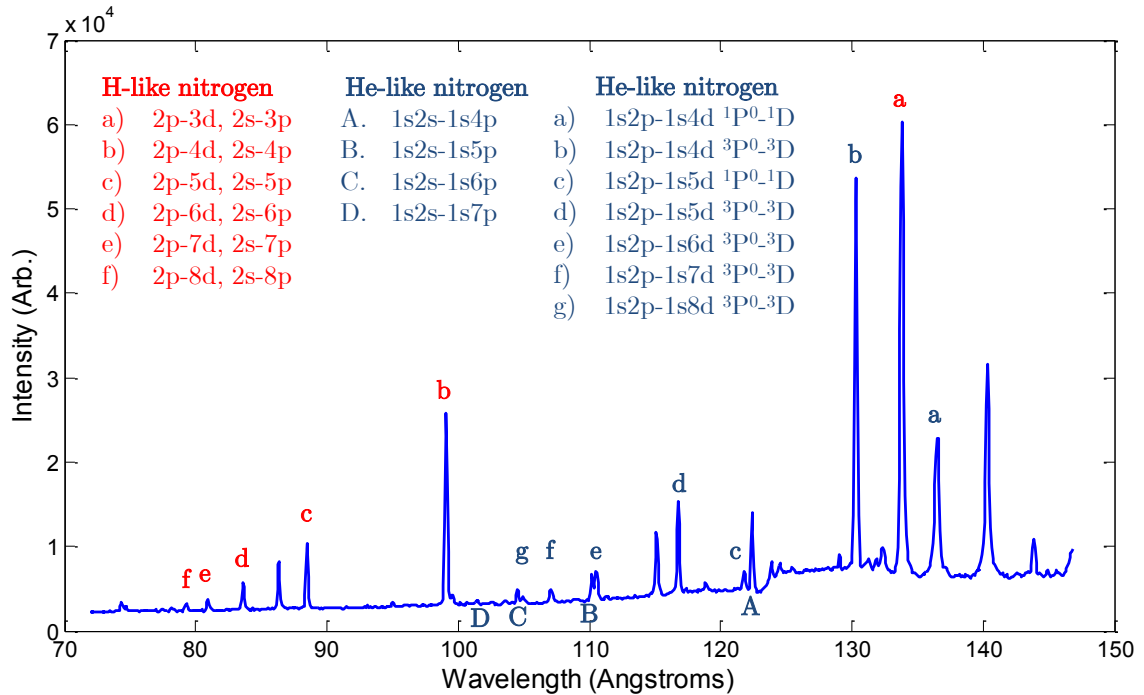


Figure 5.15: Example of a raw nitrogen spectrum recorded with the flat-field spectrometer using the 1200 line/mm grating. A 36 fs Ti:sapphire laser pulse with a peak intensity of 3.5×10^{17} W/cm² (175 mJ/pulse) irradiated a cluster jet with an average atom density of $\sim 2 \times 10^{18}$ cm⁻³ (solenoid valve at -150° Celsius, backed by 550 PSI N₂). A thin zirconium filter prevented laser light from entering the spectrometer. Li-like, He-like and H-like nitrogen emission lines are visible in first order, and some H-like and He-like lines are visible in higher orders. Here, select first-order H-like and He-like emission lines have been labeled. In the H-like emission series shown, the 2p-Xd and 2s-Xp line pairs are not separately resolved.

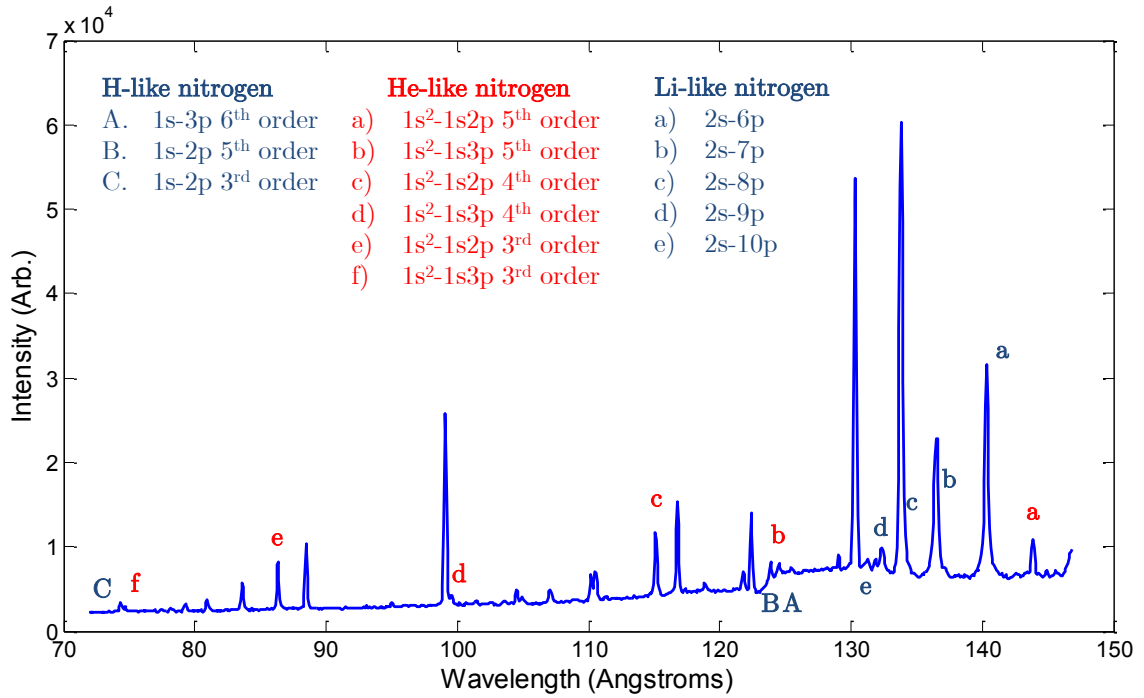


Figure 5.16: The same spectrum shown in Figure 5.15, with a different group of emission lines labeled. Li-like emission lines and continuum are observed in the first order above at wavelengths above 125 Å. He-like and H-like emission with wavelength < 30 Å is observed in higher orders.

wavelengths longer than 145 Å were not observed due to the positioning of the back-thinned CCD camera in the spectrometer, which has an active area that is narrower than the flat focal field of the diffraction grating. Additionally, some H-like and He-like emission lines with wavelengths less than 50 Å were diffracted in high order from the 1200 line/mm grating and are labeled in Figure 5.16. These lines were also observed using the 2400 line/mm grating in first order in Figure 5.14.

A peak laser intensity of 10^{19} W/cm² is required to field-ionize H-like nitrogen with a femtosecond pulse at a wavelength of 800 nm [74,77], well in excess of the peak intensities reached in this experiment, so it is clear that any observation of He-like or H-like spectral emission must be attributed to electron collisional ionization enabled by the presence of clusters. On this basis, the EUV spectra we have collected indicate that the nucleation of nitrogen clusters occurs within the full range of temperatures accessible to our gas valve, at temperatures as high as 22° Celcius. EUV emission lines from H-like nitrogen in the femtosecond laser-irradiated cluster jet below the OFI ionization threshold has also been observed in previous experiments, in a jet from a cryogenically cooled gas valve irradiated by a 7×10^{17} W/cm² laser [77] and in a jet from an uncooled gas valve irradiated with a peak intensity of 1.2×10^{17} W/cm² [74].

Over the full range of experimental parameters explored, the relative emission intensity of all spectral lines from within each individual ion species (H-like, He-like or Li-like) was stable. The only changes in the intra-species line intensity ratios observed were explained by variations in the frequency-dependent re-absorption of EUV by neutral gas in the vacuum chamber between the laser-produced plasma

and spectrometer. This suggests that the combination of 2-body and 3-body recombination responsible for emission is constant within each species, and that no amplification is occurring on the $2p_{3/2} \rightarrow 1s_{1/2}$ ($\lambda = 24.779 \text{ \AA}$) and $2p_{1/2} \rightarrow 1s_{1/2}$ ($\lambda = 24.785 \text{ \AA}$) Lyman α transitions in H-like nitrogen. However, there were changes in the *inter*-species emission intensity ratios between the H-like, He-like and Li-like species as the laser energy and nitrogen cluster size were changed. This indicates that the fraction of the nitrogen atom ensemble reaching a given ionization species is changing as the laser pulse energy and cluster size vary. These trends are discussed in detail below.

5.6.1 EUV emission scaling with laser intensity

When the gas valve was held and constant backing pressure (550 psi) and solenoid open time (450 μs) used for several temperatures and the laser energy was scanned up to 250 mJ ($5 \times 10^{17} \text{ W/cm}^2$), EUV emission from H-like, He-like and Li-like nitrogen species all monotonically increased (Figure 5.17, subplots (a), (b) and (c), respectively). An absolute comparison of the EUV intensity from each species is not meaningful in these plots, because the wavelength-dependent quantum efficiency of the CCD camera and diffraction efficiency of the grating in the EUV spectrometer was not compensated for. However, by comparing the relative emission ratios between these three species (Figure 5.18), differences in EUV emission growth as a function of energy become apparent.

It can be seen in Figure 5.18(a) that at laser energies below 50 mJ (1×10^{17}

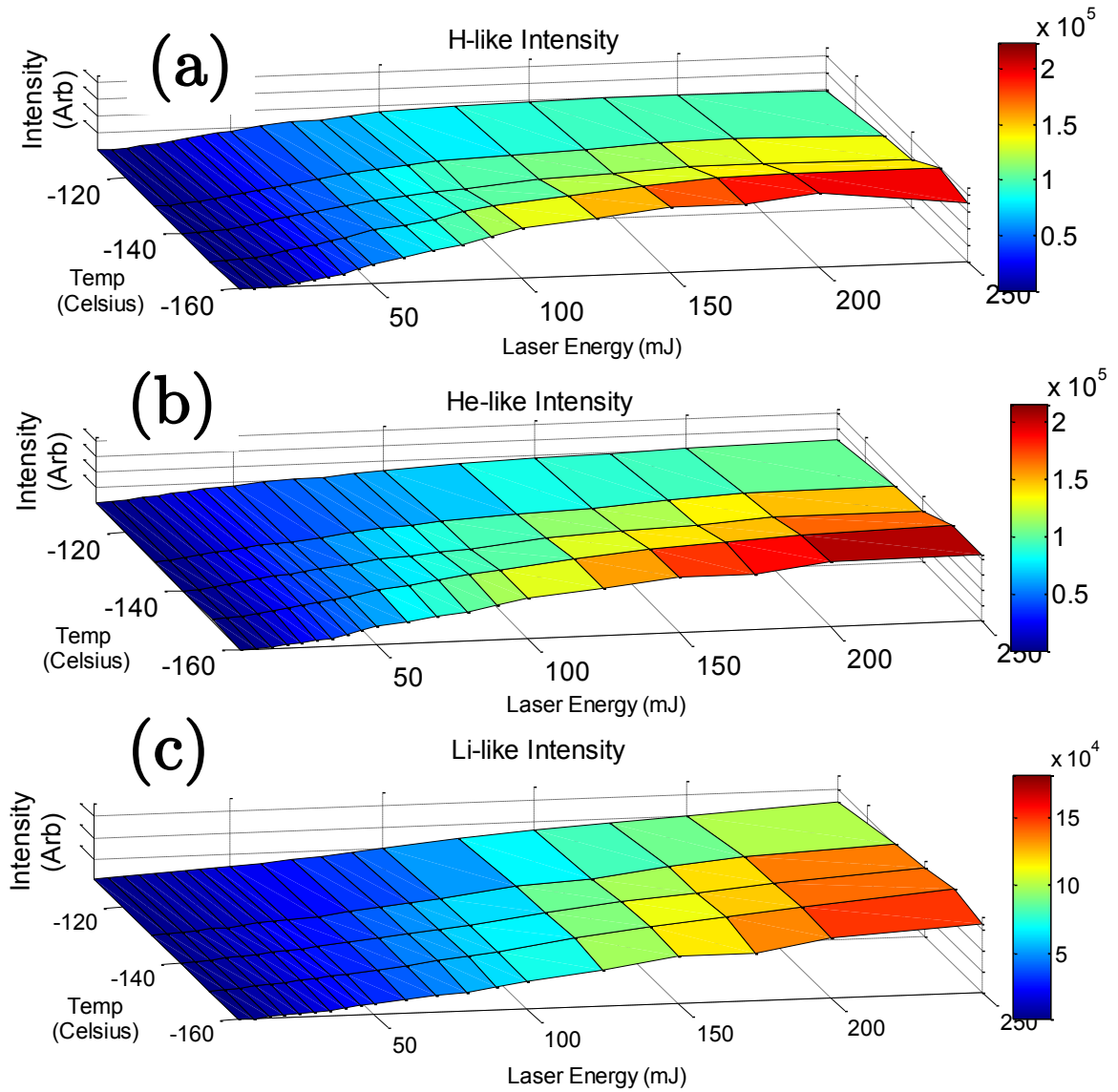


Figure 5.17: A 36 fs FWHM Ti:sapphire laser pulse energy vs valve temperature scan showing (a) H-like, (b) He-like and (c) Li-like intensity measured by summing emission lines. The H-like intensity shown is the sum of the 2p-3d, 2s-3p, 2p-5d and 2s-5p lines, He-like is the sum of 1s2p-1s4d and 1s2p-1s5d, and Li-like is the sum of 2s-6p and 2s-9p. The emission from each species grows steadily as the laser energy rises and the solenoid valve temperature drops (which increases the mean cluster size). In this data set, the nitrogen atom density was not measured, but likely increased as the temperature was decreased.

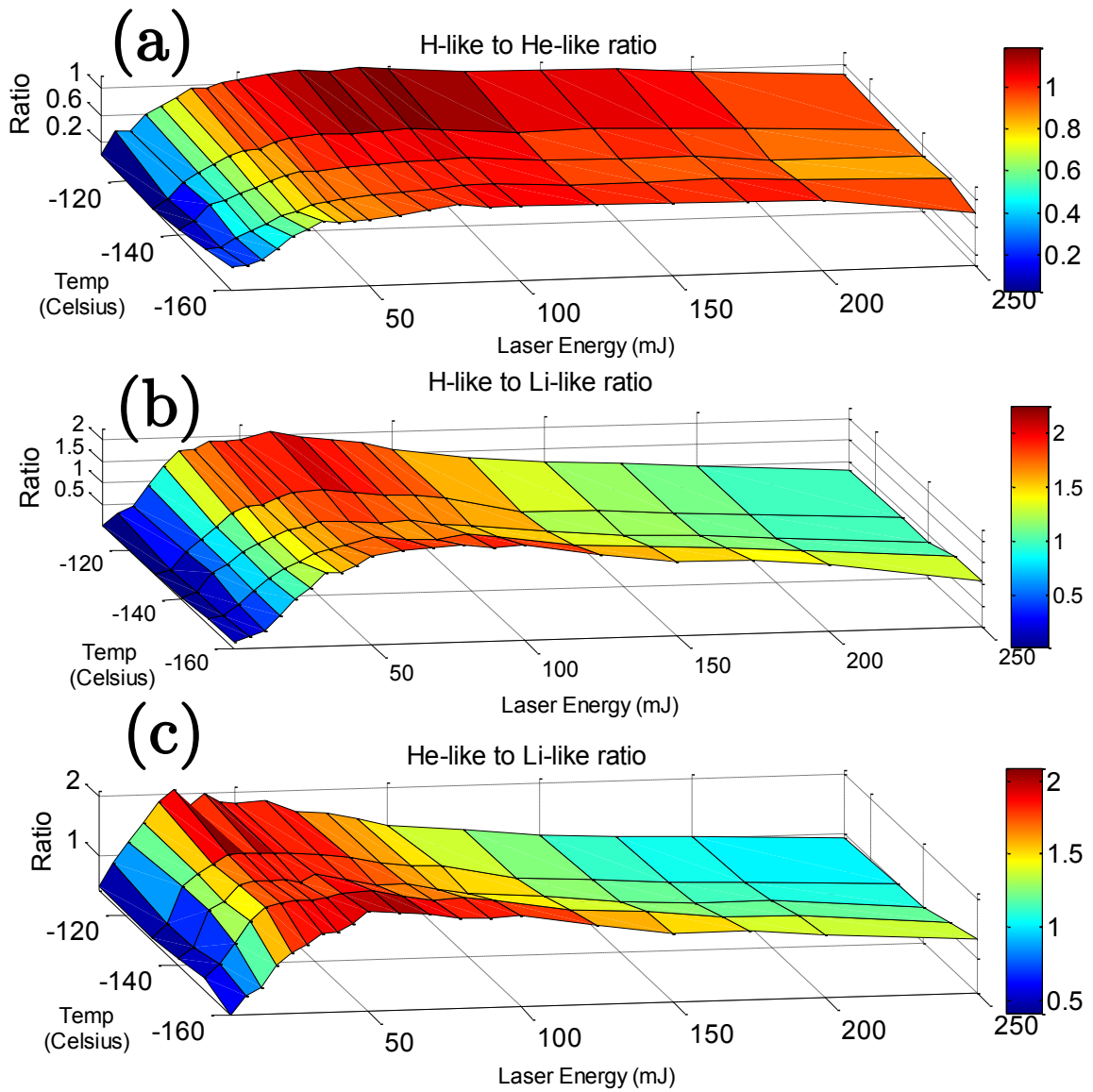


Figure 5.18: The relative ratios of the line emission intensities from species shown in Figure 5.17. The ratio of H-like to He-like reveals that the H-like EUV emission begins at higher laser intensities than the He-like, and that the H-like to He-like emission ratio stabilizes above ~ 50 mJ (a peak intensity of 1×10^{17} W/cm²). The H-like to Li-like (b) and He-like to Li-like (c) ratios are similar, peaking at ~ 40 mJ (8×10^{16} W/cm²), which can be explained by the fact that the Li-like ionization threshold (97 eV) is much lower than the similar He-like (552 eV) and H-like (667 eV) thresholds.

W/cm²), the relative ratio of H-like to He-like emission grows with increasing intensity. Additionally, it can be seen in Figures 5.18(b) and (c) that at laser energies below 40 mJ (8×10^{16} W/cm²), the relative ratios of H-like and He-like to Li-like emission grow. This can easily be explained by observing the ionization thresholds of Li-like (97 eV), He-like (552 eV) and H-like (667 eV) nitrogen — the onset of emission for species with larger ionization thresholds occurs at higher intensities, then saturates for each species once the laser pulse is able to maintain the intensity required for ionization throughout the entire thickness of the jet. Once this saturation occurs, the relative ratios in Figure 5.18 remain essentially constant as the laser energy is further increased. The continued growth of absolute EUV emission intensity from all three species above 50 mJ seen in Figure 5.17 can be explained by the radially increasing focal volume subject to laser intensity above the ionization threshold for each species.

The qualitative behavior of these results agrees with previous observations [150] in which it was shown that xenon clusters exhibit a relatively low intensity threshold for x-ray and EUV production from a given cluster. Once the effective species ionization threshold was crossed, the emission per cluster within that ion species remained essentially constant as a function of intensity and the primary consequence of increasing intensity was to increase the focal volume exposed to intensities above the species ionization threshold. The results presented in Figure 5.18 bear this out, and show that once the laser has crossed the effective ionization threshold for all ion species, all EUV emission grows in tandem with laser intensity as the volume of the focus increases radially.

Figure 5.17 also shows that for fixed laser energy, EUV emission intensity from all species increased as the gas valve temperature was decreased from -110° to -160° Celsius. However, the nitrogen atom density in the cluster jet was not measured in this particular experimental run and likely increased as falling gas valve temperature reduced the impedance of the solenoid, increasing the mass output per pulse, which could explain the growth in EUV emission intensity with decreasing temperature in this data set. In the data presented in subsequent sections, this issue was avoided by measuring the neutral atom density and adjusting gas valve parameters (solenoid open time and backing pressure) to maintain constant jet density as the temperature was adjusted. This allowed us to study the trends in EUV emission as a function of mean cluster radius while holding the mean atom density within the jet fixed.

5.6.2 EUV emission scaling with cluster radius

Using the procedure for holding atom density constant discussed above, scans were performed with fixed laser intensity and target density, while the mean cluster size in the jet was controlled by scanning the gas valve temperature from -180° to -60° Celsius. EUV in the $15 - 50 \text{ \AA}$ spectral region was collected using the 2400 line/mm grating and a $0.2 \text{ }\mu\text{m}$ thick Ni filter, allowing observation of the H-like and He-like nitrogen emission lines shown Figure 5.14. The relative ratios of the emission lines within both of these ion species was stable as the gas valve temperature was scanned for each laser energy and target density. This was also the case for the data presented in the previous section which was collected as a function of laser energy

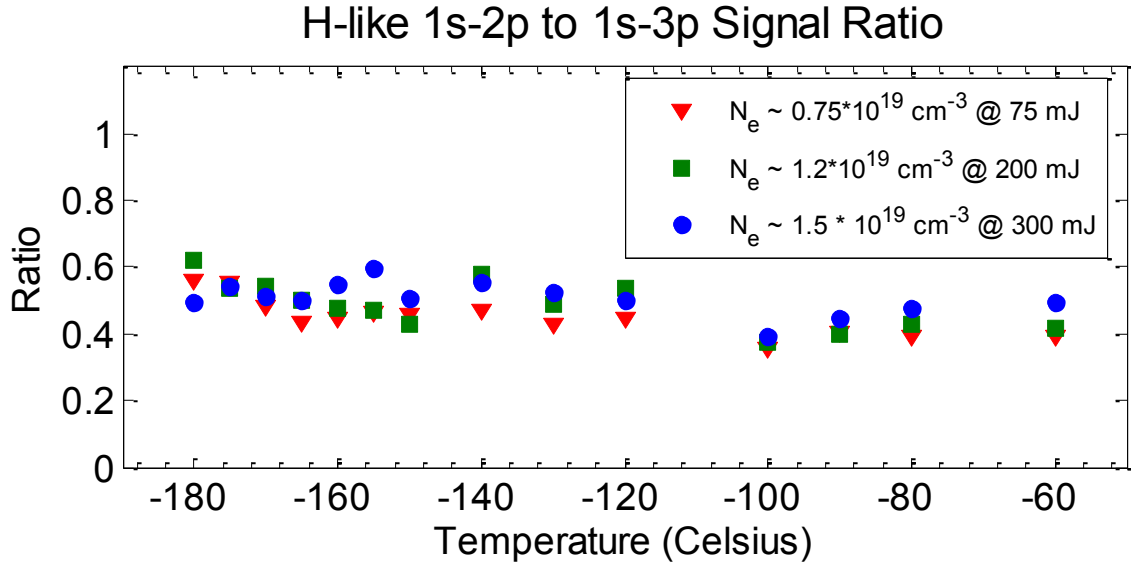


Figure 5.19: Plot showing that the ratio of 1s-2p to 1s-3p H-like nitrogen emission remains constant as a function of gas valve temperature for three different mean target densities, indicating that no amplification is taking place. These two H-like nitrogen emission lines are components of the signal shown in Figure 5.20(a).

(Figure 5.17). An example of this stability is displayed in Figure 5.19. The ratio of the 1s-2p to 1s-3p H-like nitrogen emission lines was essentially unchanged as the gas valve temperature was varied for three different mean target densities. This indicates that the original goal of this experiment, amplification of the $2p_{3/2} \rightarrow 1s_{1/2}$ and $2p_{1/2} \rightarrow 1s_{1/2}$ H-like nitrogen emission lines, is not taking place.

The slight apparent discontinuity in the data between -120° and -100° Celsius can be explained by noting that this data was collected in experimental runs on two separate days (-180° to -120° , then -100° to -60° Celsius). Gradual wear in the gas valve poppet and variation in the laser output made it difficult to exactly

replicate experimental conditions from day to day.

Trends in the total EUV emission intensity from the H-like and He-like species as a function of gas valve temperature are shown in Figures 5.20(a) and 5.20(b), respectively. The intensities plotted are the sum of the five H-like and five He-like EUV emission lines labeled in Figure 5.14. Emission line intensities were measured (in arbitrary units) by subtracting the optical background, then adding the values of the four highest-valued pixels within the line profile. The wavelength-dependent diffraction efficiency of the diffraction grating and quantum efficiency of the camera were not compensated for, so this analysis only considers trends in EUV emission intensities.

These temperature scans were run for three different electron density / laser energy pairs — $7.5 \times 10^{18} \text{ cm}^{-3}$ at 75 mJ, $1.2 \times 10^{19} \text{ cm}^{-3}$ at 200 mJ and $\sim 1.5 \times 10^{19} \text{ cm}^{-3}$ at 300 mJ. These pairs were chosen to ensure that at least ~ 50 mJ of laser energy was transmitted through 1 mm thick cluster jet. This guarantees that the intensity within the cluster jet is always above $1 \times 10^{17} \text{ W/cm}^2$, where saturation in the H-like emission growth was observed in the energy scans discussed in the previous section (Figure 5.18).

For all three laser energy/ target density pairs, EUV emission from H-like (Figure 5.20(a)) and He-like (Figure 5.20(b)) nitrogen species increased as the gas valve temperature was decreased from -60° to -160° Celsius. By comparing these trends to the mean cluster radius measurement shown in Figure 5.10, it is clear that a jet containing larger clusters will emit more intense EUV emission. This is corroborated by 1-D hydrocode simulations that will be discussed in the subsequent

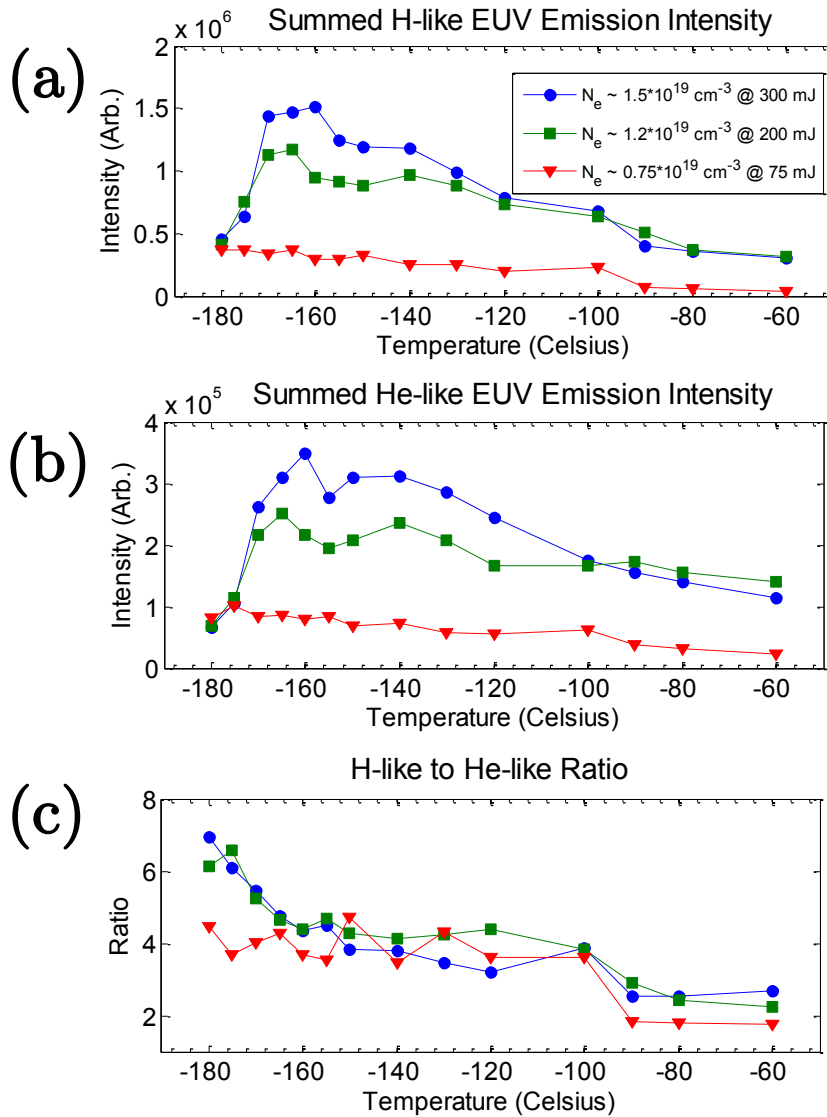


Figure 5.20: Trends in H-like (a) and He-like (b) nitrogen EUV emission as a function of gas valve temperature for three target density/ laser energy pairs. The intensities displayed are the sum of all emission lines within each species labeled in Figure 5.14. The sharp drop in H-like and He-like emission intensity as the temperature drops below -160° Celsius corresponds to the onset of droplet formation. The H-like to He-like nitrogen EUV emission ratio (c) is relatively stable as a function of temperature, with the exception of a sharp jump as the temperature drops below -90° Celsius, when the mean cluster radius increases from 30 to 100 nm (Figure 5.10).

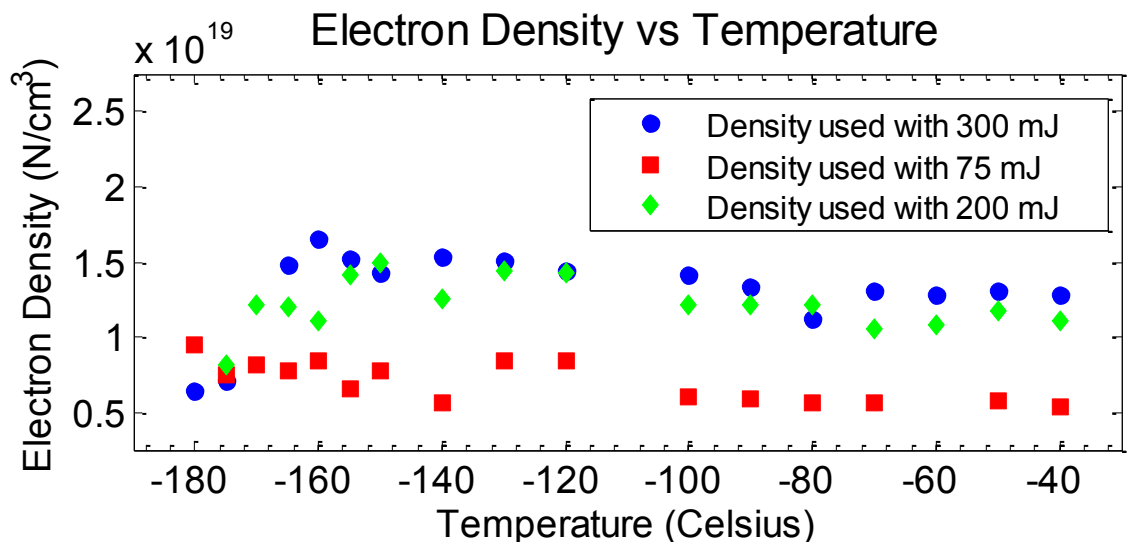


Figure 5.21: Electron densities measured using transverse interferometry for the experimental parameters used in Figures 5.20 and 5.19. At lower temperatures, the mass output of the gas valve was unstable as a function of backing pressure and difficult to control precisely.

section. Fluctuations in the EUV emission intensity below -140° Celsius can be explained by variations in the target density, which was measured using transverse interferometry at each data point and is shown in Figure 5.21.

However, once the gas valve is cooled below approximately -160° Celsius, this trend is reversed as the EUV emission from H-like and He-like nitrogen sharply drops (Figures 5.20(a) and 5.20(b)). We attribute this to the pre-expansion nitrogen in the solenoid valve undergoing a gas-to-liquid phase transition, resulting in the release of a stream of liquid that fragments into droplets after entering the vacuum. It has also been previously observed [50] that the mean aggregate diameter in a droplet jet is larger ($> 1 \mu\text{m}$) than those encountered in a cluster jet ($< 100 \text{ nm}$). The gas-liquid phase transition in nitrogen at -160° Celsius occurs at 250 PSI, in good agreement with our experimental parameters. We also see that this transition occurs at slightly lower temperatures when the backing pressure is dropped, as predicted by the pressure-temperature phase diagram (Figure 5.11).

Sharply increased pump scattering seen in transverse interferograms (prior to phase extraction and Abel inversion) and stronger absorption of the pump corroborate this conclusion. There is also an abrupt increase in the amount of visible, blue-shifted laser light (due to self-phase modulation during the ionization process) in the transmission through the cluster jet. Additionally, when the pressure and temperature within the solenoid valve crosses the vapor pressure curve and enters the liquid regime, the mass output of the valve as a function of backing pressure becomes highly unstable. This agrees with previously published results in which the gas-liquid phase transition was observed in argon jets [37].

Although a previous study on EUV production from nitrogen clusters [77] claimed to generate nitrogen droplets, the sharp drop in absolute EUV emission at the onset of droplet formation that we observe was not seen. Moreover, the temperature of -95° Celsius at which droplets were reported is well above the N_2 critical temperature of -146.9° Celsius. Therefore, we believe that the results in this dissertation are the first measurements of EUV spectra from laser-irradiated nitrogen droplets.

The ratio of EUV emission from H-like and He-like nitrogen (Figure 5.20(c)) is relatively stable as the temperature is decreased from -60° to -160° Celsius, with the exception of a sharp jump as the temperature drops below -90° Celsius, when the mean cluster radius increases from 30 to 100 nm (Figure 5.10). The ratio of H-like to He-like emission seen when the mean cluster radius is greater than 100 nm (which occurs at temperatures of -100° Celsius and lower) is robust over a wide range of laser intensities (Figure 5.18(a)) and indicates that a fully stripped nitrogen plasma is being created by the laser-cluster interaction. This conclusion is corroborated by 1-D hydrocode simulations of these parameters that will be discussed in the following section.

Additional support for this conclusion can be found by comparing the absolute intensities of the H-like and He-like emission spectra. Although the wavelength dependent quantum efficiency of the CCD camera and diffractive efficiency of the grating in the spectrometer were not compensated for in these measurements, the H-like $1s-2p$ (24.779 and 24.785 Å) and He-like $1s^2-1s3p$ (24.898 and 24.962 Å) emission lines are sufficiently close together to allow an absolute comparison of

species emission intensity to be made without compensating for the spectrometer efficiency.

To make a simple prediction for what the relative strength of the emission in these two spectral lines should be in a fully stripped plasma, we assume that all electrons pass through the $n = 3$ electron shell of a He-like or H-like nitrogen ion after recombining, and that they are evenly distributed amongst all possible states within this shell. When this assumption holds during the H-like then He-like recombination, each atom will either decay straight from an $n = 3$ to $n = 1$ state and emit a single photon, or will decay in two stages, first from $n = 3$ to $n = 2$ then $n = 2$ to $n = 1$. The ratio of the total rate of all possible H-like $n = 3$ to $n = 2$ decay to the total rate of all possible He-like $n = 3$ to $n = 1$ decay should thus be the ratio of the H-like $1s-2p$ and He-like $1s^2-1s3p$ emission line intensities.

This can be easily determined by observing the dipole allowed decay pathways in H-like atoms. Electrons in $3d$ and $3s$ states decay to $2p$, which then decays to $1s$, whereas electrons initially in $3p$ states can decay to $2s$ or $1s$ states. However, the $2s$ state is metastable and cannot decay to the $1s$ state, so it will likely be re-excited into the $3p$ state, eventually decaying directly to the $1s$ state. Therefore, the total ratio of 3-1 to 2-1 emission will be the ratio of the total number of $3d$ and $3s$ states to the number of $3p$ states. The $3d$ level is 14 times degenerate ($\ell = 3/2, 5/2$ and $3/2$ states) [151], the $3p$ level is 6 times degenerate ($\ell = 3/2$ and $1/2$ states) [151] and the $3s$ level is 4 times degenerate ($\ell = 1/2$ and $1/2$ states) [151]. Therefore, the total expected ratio of 3-1 to 2-1 emission within H-like nitrogen is $(14+4)/6 = 3$.

Although these energy levels will undergo additional splitting during He-like

decay when there is also an electron in the ground state, this will not change the H-like result substantially. Therefore, the 3-2 to 3-1 intensity ratio within H-like should be the same as that within He-like, and the ratio of H-like $1s-2p$ (24.779 and 24.785 Å) to He-like $1s^2-1s3p$ (24.898 and 24.962 Å) should be approximately 3 if the plasma is fully stripped. This is in very good agreement with the ratios of 2.5 to 3.5 observed in spectra collected when the gas valve temperature was below -100° Celsius (Figure 5.20).

5.7 Electron temperature extraction from EUV spectra

It was also possible to extract electron temperature information from these spectra [152] that correspond to the times at which recombination to the H-like and He-like ion species occurs, using the recombination continua shown in Figure 5.22. The shape of the continuum reflects the distribution of kinetic energies in electrons that undergo recombination. Thermal electrons will have a Maxwellian speed distribution $\propto v^2 \exp(-m_e v^2 / 2kT_e)$, so radiative recombination to a given bound state with ionization potential E_i will result in the emission of photons with a frequency distribution $\propto \exp(-h\nu/kT_e)$. This allows extraction of the electron temperature T_e using an exponential fit to the recombination continua in the H-like and He-like emission spectra displayed in Figure 5.20.

The electron temperature at the time of recombination is found to be between 5 and 20 eV for both species, independent of the gas valve temperature. Any trends in electron temperature as a were obscured by these fairly large error bars, which were

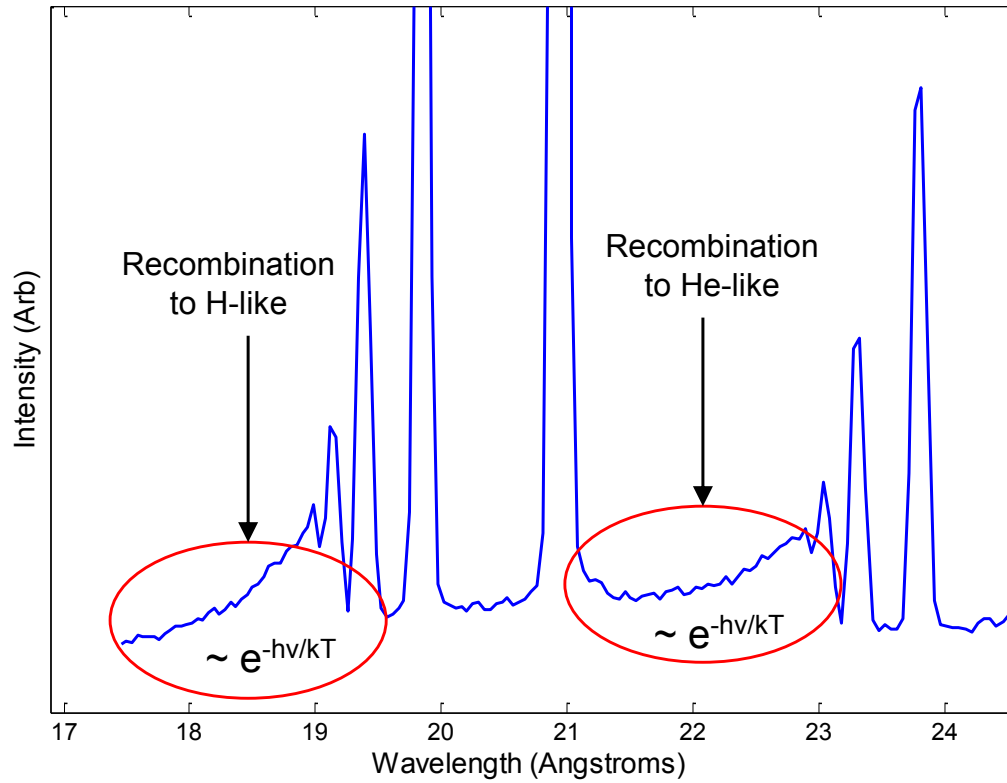


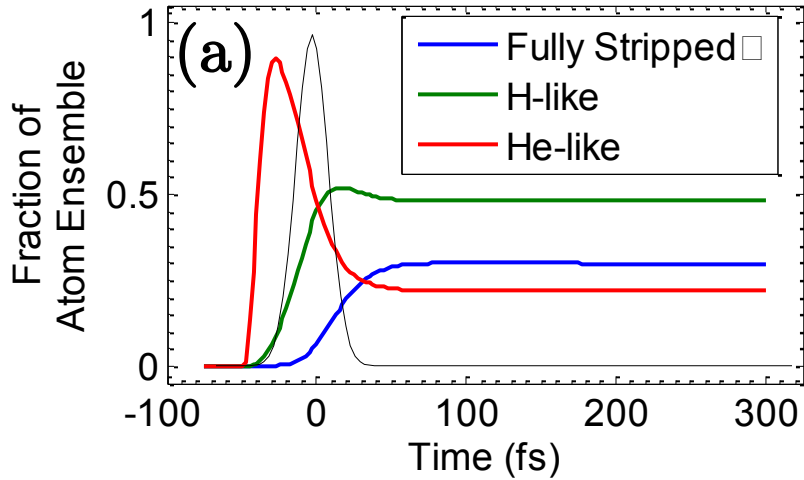
Figure 5.22: Detail of a raw spectrum from Figure 5.14 showing the He-like and H-like series recombination continuum edges from which the electron temperature could be estimated.

a result of nonuniform optical background on the CCD from scattered light within the spectrometer. This diffuse background could not be cleanly disentangled from the EUV signal dispersed by the grating, and choosing different levels of background subtraction resulted in different extracted electron temperatures. The fact that this deeply ionized plasma was created in the presence of electron temperatures many orders of magnitude below the ionization threshold is confirmation of the strong nonequilibrium processes that this experiment was designed to achieve.

5.8 Simulations and analysis

In an effort to better understand trends in the H-like and He-like emission ratios observed experimentally and to investigate why no lasing occurred, simulations of the laser-cluster ionization process were performed. The irradiation of a 20, 40, 60, 80 or 100 nm radius nitrogen cluster with a 36 fs, 800 nm, 6.25×10^{17} W/cm² peak intensity pulse was simulated with the 1D fluid code described in [62]. This corresponds to the range of cluster sizes encountered in the data shown in Figure 5.20 and the laser intensity reached with 300 mJ of laser energy. Time $t = 0$ denotes the peak of the laser pulse. The output provides the fluid velocity, electron temperature, electron density, ion temperature and ion species densities as a function of radius over this time interval. As discussed above, this code does not include effects due to the large electron oscillation amplitudes and relativistic mass corrections encountered at intensities above 10^{16} W/cm², but can be used to gain insight into trends in the cluster heating and explosion dynamics.

20 nm Cluster Radius, Ionization vs Time



100 nm Cluster Radius, Ionization vs Time

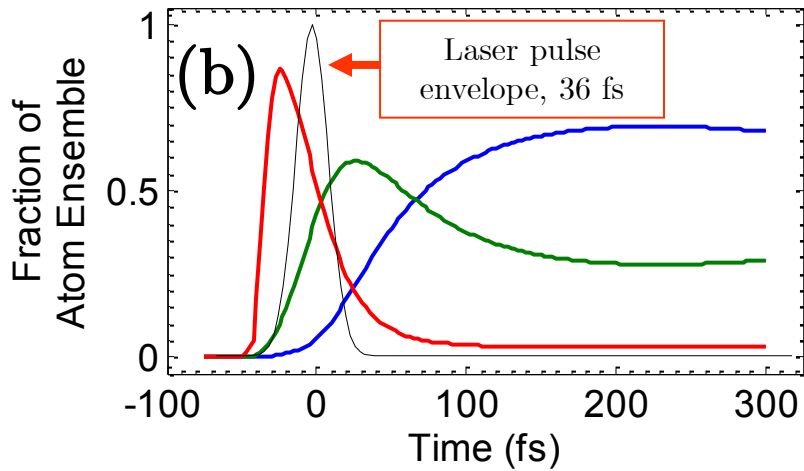


Figure 5.23: Plots of the simulated ion species populations as a function of time when 20 nm (a) and 100 nm (b) radius nitrogen clusters were irradiated with a 36 fs FWHM Ti:sapphire laser pulse with a peak intensity of $6.25 \times 10^{17} \text{ W/cm}^2$. Maximum average ionization $\langle Z \rangle_{avg}$ occurs at $t = 105 \text{ fs}$ and 225 fs for the 20 and 100 nm clusters, which are 30% and 69% fully stripped at those times, respectively.

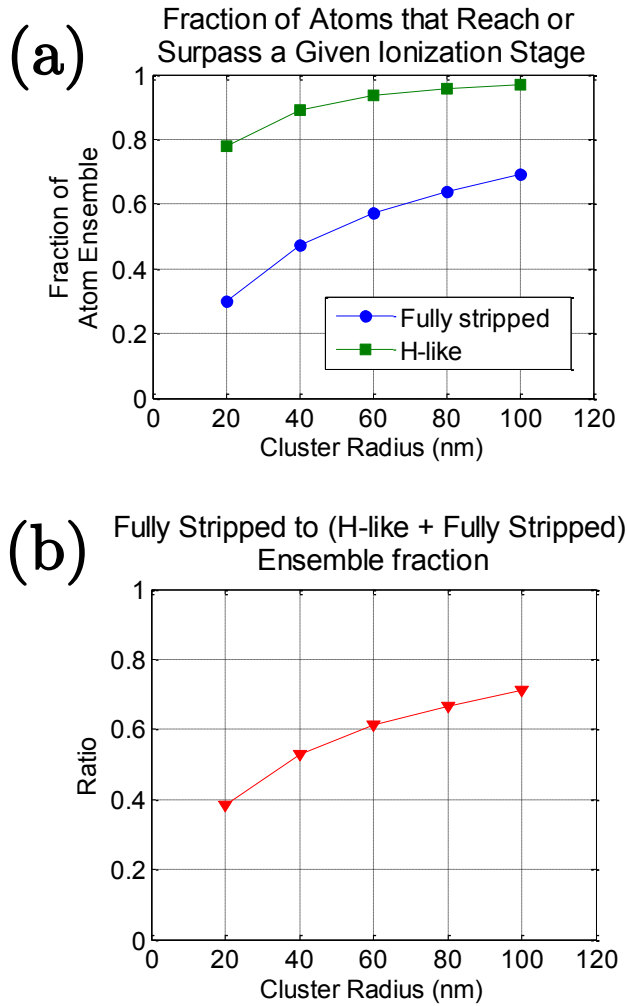


Figure 5.24: Simulation results showing the absolute (a) and relative (b) ionization fraction of the ensemble of nitrogen atoms within 20, 40, 60, 80 and 100 nm radius nitrogen clusters irradiated with a 36 fs FWHM Ti:sapphire laser pulse with a peak intensity of $6.25 \times 10^{17} \text{ W/cm}^2$. Plot (b) is the ratio of the two lines plotted in (a). The relative ratio of EUV emission from H-like and He-like ion species should follow the trend in (b), ignoring any collisional re-excitation events after recombination has occurred.

5.8.1 Ionization fraction vs cluster size

For all five cluster sizes simulated, the entire ensemble of ions within the cluster reached at least the He-like ionization stage before the laser pulse reached peak intensity. The fraction of the ensemble of ions in the He-like, H-like and fully stripped ion stages for the largest (100 nm) and smallest (20 nm) clusters simulated is shown as a function of time in Figure 5.23. In both cases, $> 99\%$ of the atoms in the cluster reach at least the He-like ionization stage before the pulse reaches peak intensity, and do not drop below this stage for the duration of the simulation window. The larger 100 nm cluster then becomes more deeply ionized than the 20 nm cluster, but takes longer to do so. The peak fully stripped fraction is larger (69% vs 30%) and occurs at a later time after the peak intensity (225 fs vs 105 fs) in the 100 nm cluster as compared to the 20 nm cluster.

The details of this trend as a function of cluster size are shown in Figure 5.24. A plot of the fraction of the nucleus ensemble that reaches the H-like and fully stripped ion stages are shown in (a), rising with the cluster size. Plot (b) then shows the ratio of the two lines plotted in (a), which should follow the same trend as the EUV recombination emission seen from the H-like and He-like species, assuming that no ‘extra’ emission from collisional re-excitation and decay in these ion species happens after the initial recombination has occurred.

This provides reasonable quantitative agreement with the features observed in our experiment. The plot in Figure 5.24 predicts an EUV emission ratio from the H-like to He-like species that jumps by 54% (from 0.46 to 0.71) as the cluster size is

increased from 30 nm to 100 nm, which agrees reasonably well with the 73% jump in relative emission intensity (from 2.2 to 3.8) observed experimentally as the temperature drops through -90° Celsius in Figure 5.20(c), when the measured cluster size increases from 30 to 100 nm (Figure 5.10). Additionally, it should be noted that this code underestimates the ionization fraction that will actually occur. The code considers electron collisional ionization only from the ground state of each ion. However, in practice collisional ionization will proceed from excited states already populated by electron collisions, thus strongly enhancing the ionization yield. It is thus highly likely that a fully stripped plasma occurs in the conditions simulated and shown in Figure 5.20(c), as we concluded based on the experimental results.

5.8.2 Energy deposition and plasma temperature

The simulation results give a mean radial fluid expansion speed of 7×10^7 cm/s in the 20 nm cluster at the end of the simulation window. Since a jet of uniformly distributed 20 nm clusters with an average atom density of 3×10^{18} cm $^{-3}$ will have an average cluster separation of 0.9 μ m, the expanding nanoplasmas will merge into a uniform plasma after ~ 2 ps. Based on the slow recombination rate seen within the simulation window (Figure 5.23), to a good approximation we can say that $\langle Z \rangle_{avg}$ does not change in the time period before the clusters merge into a uniform plasma. Once the laser pulse has passed, all of the residual energy deposited by the laser will be contained in the random thermal motion of the ions and electrons, directed kinetic motion of the electron-ion fluid and potential energy in the ions from the

liberation of electrons.

Figure 5.25 shows how the distribution of residual energy within the plasma changes after the passage of the laser pulse. Initially, all of the energy deposited by the laser is contained in the thermal energy of the electrons (Figure 5.25(a)) plus ionization potential energy, which remains approximately constant throughout the simulation window after the passage of the laser pulse. As electron pressure drives radial expansion of the cluster, the electron temperature T_e drops, and the average radial velocity v_j of each radial mass element j rises (Figure 5.25(f)). The nanoplasma remains quasi-neutral throughout expansion, so the average radial velocity of the ions and electrons will be the same, resulting in an ion to electron radial kinetic energy ratio of $m_i/m_e \simeq 25000$. Thus the net effect is that the residual energy deposited by the laser is initially in the form of electron thermal energy (Figure 5.25(a)), but is transferred almost completely into radial ion kinetic energy (Figure 5.25(e)) within the 300 fs simulation window.

To determine the temperature of the uniform plasma created by the merged cluster plasmas 5 ps after the arrival of the laser, consider an ion in a mass element j of an expanding cluster with velocity $\mathbf{v} = \mathbf{v}_j + \Delta\mathbf{v}_j$, where \mathbf{v}_j is the fluid velocity of mass element j (radially directed with respect to the cluster center of mass) and $\Delta\mathbf{v}_j$ represents the range of ion thermal velocities in mass element j such that $\frac{1}{2}m_i\langle\Delta v_j^2\rangle \simeq \frac{3}{2}k_B T_i$. After the clusters merge, a new effective ion temperature T_{eff} is

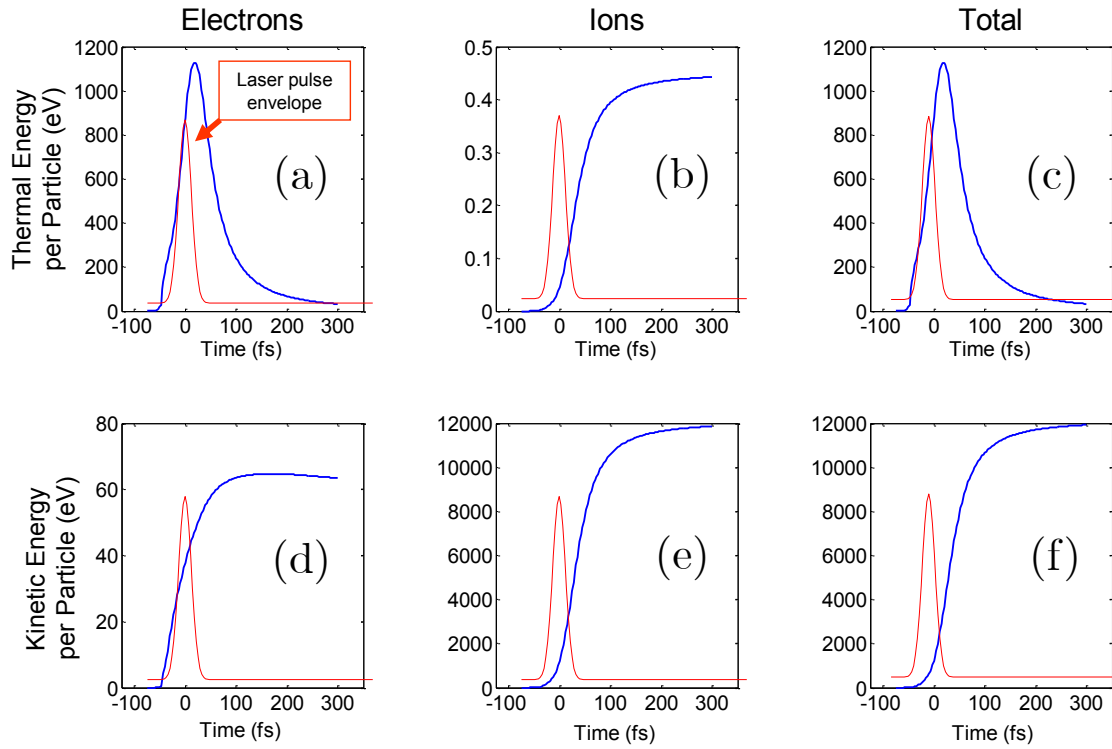


Figure 5.25: Results for a simulation of the irradiation of a 20 nm radius nitrogen cluster with a 36 fs FWHM Ti:sapphire laser pulse with a peak intensity of 6.25×10^{17} W/cm² showing the average thermal (*a* – *c*) and kinetic (*d* – *f*) energy per particle as a function of time for electrons (*a*, *d*), ions (*b*, *e*) and in total (*c*, *f*). Initially, the deposited laser energy is primarily in electron thermal motion (*a*), but as the cluster expands the energy is transferred almost entirely to radial ion kinetic energy (*e*). The clusters merge into a uniform plasma after < 5 ps, at which time the ion kinetic energy re-thermalizes.

established, where

$$\begin{aligned}
\frac{3}{2}k_B T_{\text{eff}} &= \frac{1}{2}m_i \langle \mathbf{v} \cdot \mathbf{v} \rangle & (5.2) \\
&= \frac{1}{2}m_i \langle (\mathbf{v}_j + \Delta \mathbf{v}_j) \cdot (\mathbf{v}_j + \Delta \mathbf{v}_j) \rangle \\
&= \frac{1}{2}m_i \langle v_j^2 \rangle + \frac{1}{2}m_i \langle \Delta v_j^2 \rangle + m_i \langle \mathbf{v}_j \cdot \Delta \mathbf{v}_j \rangle \\
&= \frac{1}{2}m_i \langle v_j^2 \rangle + \frac{3}{2}k_B T_i + 0
\end{aligned}$$

where $\langle \mathbf{v}_j \cdot \Delta \mathbf{v}_j \rangle = 0$ because for every ion with thermal velocity contribution $\Delta \mathbf{v}_j$ there is another ion with opposite contribution $-\Delta \mathbf{v}_j$. This means that after the cluster plasmas merge, the ion temperature T_{eff} of the merged, uniform plasma will be

$$T_{\text{eff}} \simeq \frac{1}{3} \frac{m_i}{k_B} \langle v_j^2 \rangle + T_i. \quad (5.3)$$

Note that an identical analysis can be performed for the electron temperature, and that the velocities with which the electrons and ions expand will be identical due to quasi-neutrality.

This has the effect of creating a uniform plasma with hot ions and cold electrons after the clusters have merged, where the mean ion and electron velocities v_i and v_e are roughly equal and randomly directed, so $T_i/T_e \simeq m_i/m_e$. Thus for a 20 nm radius cluster, this means that because the residual kinetic energy deposition per atom (thermal and directed) was ~ 12 keV, after the clusters merge into a uniform plasma the electron temperature will be < 1 eV and the ion temperature will be ~ 12 keV. In conjunction with the electron density, these parameters could be used to calculate the 3-body recombination rate in the plasma.

5.8.3 Comparison with x-ray laser theory

Although it is likely that a fully stripped nitrogen plasma is being created, no gain was observed on the $2p_{3/2} \rightarrow 1s_{1/2}$ and $2p_{1/2} \rightarrow 1s_{1/2}$ Lyman α transitions in hydrogen-like nitrogen. This can be explained by the fact that strong 3-body recombination needs to occur on a timescale faster than the 886.3 fs lifetime of the upper states, but relatively slow recombination rates are seen in fluid simulations during the 300 fs after the peak of the laser pulse (Figure 5.23).

The 3-body recombination scales $\propto n_e^2 T_e^{-9/2}$, so high electron densities and low temperatures are required to facilitate a fast rate. Simulations and data (Figure 5.22) indicate that recombination occurs when the electron temperature is < 20 eV, within the range where gain is predicted in Figure 5.1. Therefore, the electron density during the cluster explosions must be dropping too quickly to facilitate a sufficiently fast 3-body recombination rate. Once the clusters merge after ~ 10 ps of expansion, the electron densities measured in these experiments were always $< 5 \times 10^{19} \text{ cm}^{-3}$. According to the calculations [147] shown in Figure 5.1, this is too low for gain to occur even with low electron temperatures. Thus the electron density and temperature conditions in which this x-ray laser is predicted do not occur during the evolution of the plasma.

Previous work [74] in which time-resolved EUV from nitrogen cluster plasmas was observed with an x-ray streak camera showed that the majority of EUV emission occurred after the nanoplasmas merged and the bulk plasma column had time to expand and cool, between 1 and 1.8 ns after the peak of the laser pulse.

This corroborates our conclusion that little recombination occurs during the early expansion phase of the clusters, < 10 ps after the peak of the pump pulse.

Chapter 6

Conclusion

In this dissertation, the unique properties of clusters were used to enable experiments with applications in laser-based particle acceleration and coherent EUV generation. Modulated plasma waveguides capable of guiding ultra-high intensity laser pulses that can be used to directly accelerate charged particles [126] were generated in cluster jets [141]. Additionally, development of an x-ray laser on the $2p \rightarrow 1s$ transition in H-like nitrogen was attempted, but no amplification was observed.

6.1 Summary

The results of experiments in which structured plasma waveguides were generated using two different methods to impose periodic modulations are presented in Chapter 4. These methods are both modifications of the hydrodynamic shock technique, in which a laser pulse is brought to a line focus within an elongated jet of clusters [102], creating a plasma column that hydrodynamically evolves into a channel capable of guiding. The first modulation technique uses a ‘ring grating’ to add periodic intensity modulations to the channel generating beam, which is then focused on a uniform elongated jet of clusters, resulting in periodic variations in heating that lead to modulations in diameter. The second method uses thin wire

obstructions ($< 50\mu\text{m}$ diameter) in the elongated jet of clusters, resulting in vacuum gaps in the jet. When a *uniform beam* is brought to focus within this *modulated target*, a plasma channel is created with periodic index of refraction modulations due to the vacuum gaps.

In Chapter 5, experiments were presented in which nitrogen clusters were irradiated with intense femtosecond laser pulses, in an attempt to make a transient x-ray laser [78] on the $2p_{3/2} \rightarrow 1s_{1/2}$ ($\lambda = 24.779 \text{ \AA}$) and $2p_{1/2} \rightarrow 1s_{1/2}$ ($\lambda = 24.785 \text{ \AA}$) transitions in H-like nitrogen, but no amplification was observed. Trends in the emission lines from H-like, He-like and Li-like nitrogen (1.5 to 15 nm spectral range) were collected with a single-shot flat-field spectrometer (Appendix B) as a function of incident laser energy and nitrogen cluster radius. The mean radius of clusters within the jet was measured by observing the Rayleigh scattering from a low-intensity laser [42]. Additionally, a transverse probe was used to directly measure the neutral N_2 molecule density in the jet and the electron density of the plasmas that were created using the femtosecond laser. Taken together, these results indicated that a fully stripped nitrogen plasma was created.

6.2 Future work

6.2.1 Laser-based particle acceleration

The successful demonstration of modulated plasma waveguides in cluster jets makes several avenues of research possible. Guided pulses in these channels could be used to generate terahertz [86], to quasi-phase match high harmonic generation, and

to directly accelerate charged particles [126–128]. Currently, research is underway attempting to realize the direct acceleration of electrons, by injecting a relativistic electron bunch with a co-propagating relativistic electron beam. The work presented in this dissertation represents complete development of the methods required to make the modulated waveguides required for this particle acceleration technique. Thus the main obstacles to experimental demonstration are the creation of radially polarized femtosecond laser pulse and a relativistic seed electron bunch with proper relative phasing.

A method for creating an approximation of a radially polarized laser pulse for the proof-of-concept experiment has been tested at low CW intensities and is ready to be implemented in vacuum with a higher intensity Ti:sapphire pulse. This technique works by imparting a π phase shift on half of a collimated laser beam by transmitting it through a pellicle of appropriate thickness that has been cut in half. Currently, a suitable relativistic electron source has not been tested. One possible method for generating the seed electron beam involves focusing a femtosecond Ti:sapphire laser pulse with several mJ of energy (which could be split off from the main pump pulse of the 25 TW laser system) upon a solid target [153].

6.2.2 Coherent EUV generation

It is likely that amplification was not demonstrated on the $2p \rightarrow 1s$ transition in H-like nitrogen because the 3-body recombination rate was too small compared to the lifetime of the upper level (886.3 fs) as a result of insufficient electron density.

To overcome this problem, there are two approaches that might be pursued.

First, a set of laser-cluster interaction conditions could be found that allow sufficiently fast 3-body recombination and gain to occur during the explosion of the individual nanoplasmas within a picosecond of the arrival of the laser pulse. Initially, this could be pursued by further simulations of the laser-cluster interaction, preferably using a PIC code that is valid at the relativistic laser intensities that are likely to be required

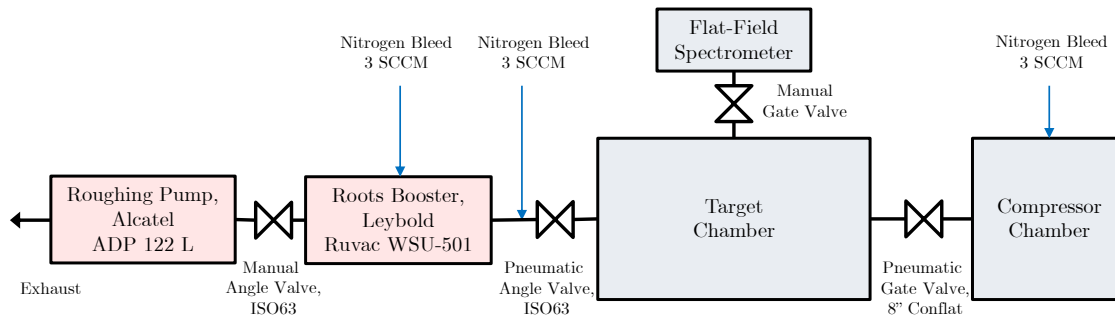
The second approach would entail increasing the average density of the cluster jet in an attempt to create the appropriate electron temperature and density for gain after the exploding clusters have merged into a uniform plasma after ~ 10 ps. In the course of the experiments performed in Chapter 5, this was attempted by removing the elongated nozzle of the gas valve, allowing the laser to strike ~ 1 mm above the circular orifice. However, the laser was unable to penetrate the 1 mm thickness of the jet as a result of high density ($\sim 7 \times 10^{19}$ atoms/cm⁻³, measured with transverse interferometry), leading to a tapered plasma that terminated in the middle of the jet. As a result, EUV emission from the plasma was strongly re-absorbed by the gas, and very little signal was seen on the flat-field EUV spectrometer. It may be possible to circumvent this problem by using a thinner cluster jet or by focusing the laser with a side-pumping geometry, for example with a reflective axicon.

Appendix A

Vacuum System

The vacuum system for the 25 terawatt laser consists of a pair of chambers connected by a 6" ID beam transfer tube, evacuated by a roots booster backed by a 5-stage roots roughing pump (Figure A.1). The chirped laser pulse enters through an AR coated CVI laser window on the chamber containing the compressor gratings (the ‘compressor chamber’). It is then directed through beam transfer tubes to the chamber in which laser-cluster interactions occur, containing the focusing optics and cluster source (the ‘target chamber’). Additional diagnostics such as a Flat-Field EUV spectrometer or an electron spectrometer can be attached to the target chamber via a vacuum bellows. The compressor chamber is a custom $\sim 0.15 \text{ m}^3$ box chamber fabricated by Kurt J. Lesker Company and the target chamber is a $\sim 0.5 \text{ m}^3$ box chamber fabricated by Nor-Cal Products.

The system is evacuated using a five-stage roots-type roughing pump (Alcatel ADP 122 L, or ‘ADP’) backing a single-stage roots-type booster (Oerlikon Leybold RUVAC WSU-501, or ‘RUVAC’). The ADP has a pumping rate of $112 \text{ m}^3\text{h}^{-1}$ with a maximum continuous inlet pressure of 37 Torr. The RUVAC has a nominal pumping speed of $505 \text{ m}^3\text{h}^{-1}$ and a maximum continuous inlet/outlet differential pressure of 60 Torr. When backed by the ADP, the RUVAC has an effective pumping rate of $\sim 450 \text{ m}^3\text{h}^{-1}$ and can draw the total volume of the vacuum system ($\sim 1 \text{ m}^3$) to an



Vacuum System Layout

Figure A.1: Topology of the vacuum system used to run experiments with the 25 TW Ti:sapphire laser.

ultimate pressure of $< 5 \times 10^{-4}$ Torr, measured with a Baratron absolute pressure transducer (MKS Instruments Model 626A) connected to the target chamber where the cluster source resides.

The choice of these vacuum pumps was motivated by the unique system design requirements imposed by the simultaneous presence of the pulse compressor gratings, which require a clean, oil-free vacuum, and the high-output gas valve used to create jets of clusters. Typically, vacuum systems containing pulse compressors are evacuated with turbo pumps backed by scroll pumps. However, a single puff from our cluster jet (a 1 mm orifice backed by 800 PSI gas, open for $\sim 650 \mu\text{s}$) releases sufficient mass to bring the chamber into the viscous flow regime ($\gtrsim 10^{-3}$ Torr) [154], where turbopumps cannot efficiently function; they are designed to operate exclusively in the molecular flow regime ($\lesssim 10^{-4}$ Torr) [154]. It may be possible to operate with a turbopump by substantially reducing the repetition rate of the gas valve, but 10 Hz operation is desirable.

Although roots pumps are ‘dry’ in the parlance of the vacuum industry, this merely means that the seal between the high and low pressure regions in the pump are not held separate with liquid, unlike a ‘wet’ pump such as a rotary vane pump in which oil creates the seal. Therefore, in spite of the fact that they are ‘dry’ pumps, both the ADP and RUVAC have gearboxes containing lubricating oil which become evacuated during operation. Oil is dangerous because it can evaporate in vacuum and then re-condense upon laser optics, allowing the laser to burn the deposited oil which leaves carbon residue on the surface, rendering that region of the optic useless. Therefore caution must be taken to prevent gearbox oil from reaching sections of the vacuum system containing laser optics. This risk is especially acute in the case of the pulse compressor gratings, which are extremely expensive and have a lead time of several months.

In a roots-type pump, the high- and low-pressure regions within the pump are separated by a pair of lobes that rotate at up to 5000 RPM. Each lobe is on a shaft driven by a gearbox that requires lubrication, so a seal on the surface of the rotating shaft is required to isolate the gearbox from the region of the pump body being evacuated by the rotors. The ADP uses dynamic seals that make contact with the moving shaft, and the RUVAC has a ‘labyrinth’ style seal that does not make contact with the shaft but has extremely close tolerances. Both the ADP and RUVAC pumps are lubricated with synthetic oil (Fomblin Y25/6 perfluoropolyether (PFPE)), which has a room temperature vapor pressure of 6×10^{-8} Torr, much lower than the $\sim 10^{-3}$ Torr vapor pressure of natural mineral oil. This reduces but does not eliminate the risk of contamination. Additionally, to minimize any pressure

differential that could draw oil vapor from the gearbox along the shaft and into the main body of the RUVAC, especially during initial evacuation of the chambers, a small auxiliary pump (Oerlikon Leybold DIVAC 0.8 T diaphragm pump) puts negative pressure on the RUVAC gearbox via a direct connection through the oil fill port.

As a further measure to safeguard against any pump seal failure which might allow oil vapor to coat laser optics, a dry nitrogen system has been installed that releases a steady bleed of N_2 at three locations to maintain pressure ($\sim 2 \times 10^{-3}$ Torr) in the viscous flow regime. This is necessary because if the pressure drops into the molecular flow regime, any contaminants can ballistically migrate upstream, and eventually coat all exposed surfaces in the vacuum. Care has also been taken to verify that all moving parts (translation stages, motorized micrometers, motion feedthrus, etc.) contained in the vacuum system use high-vacuum compatible components, containing only low vapor pressure high vacuum grease (Apiezon L or N, Krytox, etc.).

Appendix B

Flat-field EUV spectrometer

To observe the EUV light emitted from plasmas produced in the laser-cluster interaction, a custom flat-field grazing-incidence vacuum EUV spectrometer was used. This spectrometer uses a mechanically ruled aberration-corrected concave diffraction grating with variable line spacing (VLS) [155] to image spectrally dispersed EUV from an entrance slit to a flat focal plane in which a back-thinned CCD detector is placed, allowing us to obtain single-shot spectra at the repetition rate of the laser (Figure B.1a).

The spectrometer can accommodate two different gratings with different ruling densities and incidence angles, allowing the observation of two different wavelength ranges. However, switching the gratings is a time-consuming procedure requiring re-alignment of the spectrometer. Both gratings are manufactured by Hitachi, using Pyrex substrates with height \times length \times thickness dimensions of $30 \times 50 \times 10$ mm. The ruled gold surface is on the concave 30×50 face. The distance between the grating center and entrance slit/spectral plane is 237/235.3 mm for both gratings.

The first grating (Hitachi 001-0437 [156]) has a central ruling density σ_0 of 1200 lines/mm, with a blaze angle of 3.2 degrees and a blaze wavelength of 100 Å. The focal plane is flat in the 50 – 200 Å wavelength region (Figure B.1(b)), where the reciprocal dispersion ranges from 4.3 – 7.7 Å/mm. It is designed to be used at a

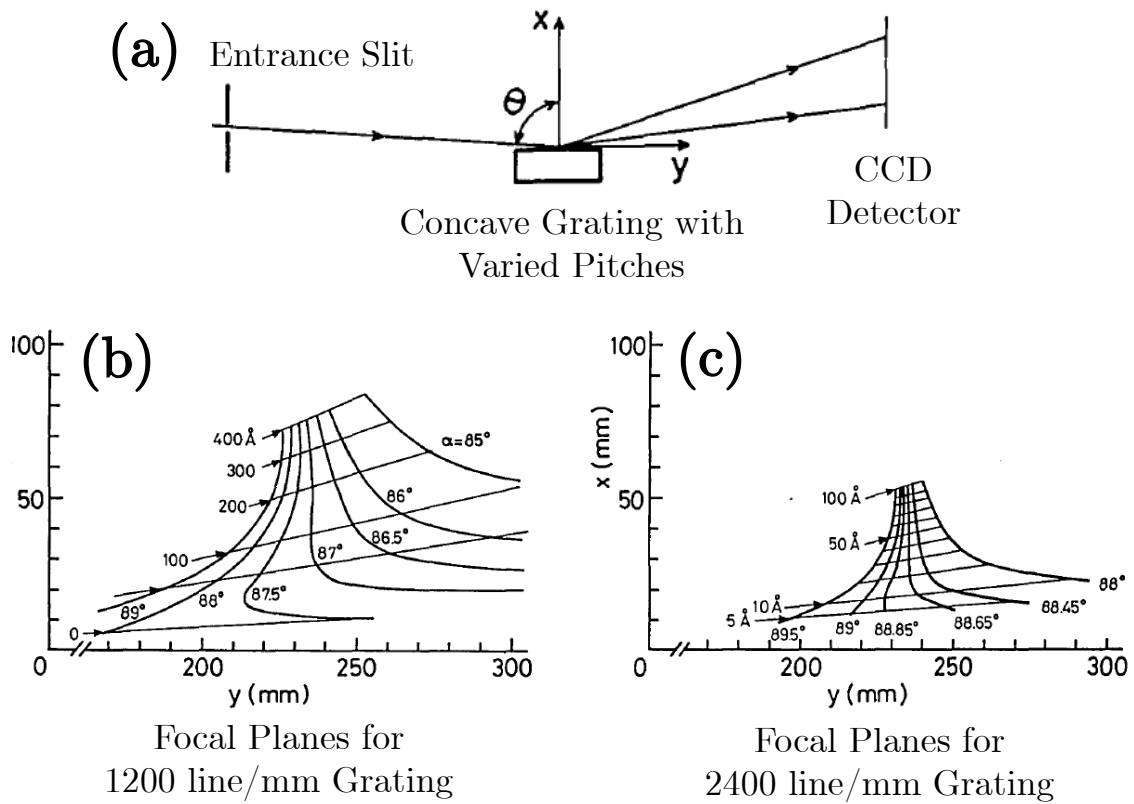


Figure B.1: Optical schematic of the flat-field spectrometer (a) and the focal planes of the 1200 (b) and 2400 (c) line/mm gratings as a function of incidence angle. Reproduced from Reference [156].

3 degree angle of incidence with respect to the plane of the grating. The grooves are variably spaced with minimum and maximum densities of 1010 and 1449 lines/mm, respectively. The ruling density is explicitly described by the expression

$$\sigma = \frac{\sigma_0}{1 + \frac{2b_2}{R}w + \frac{2b_3}{R^2}w^2 + \frac{2b_4}{R^3}w^3} \quad (\text{B.1})$$

where σ is the the ruling density w millimeters from the grating center along the length of the grating, σ_0 is the ruling density at the grating center, $R = 5649 \pm 20$ mm is the radius of curvature of the grating surface and b_2 , b_3 and b_4 are numerical coefficients with values of -20 , 4.558×10^2 and -1.184×10^4 , respectively.

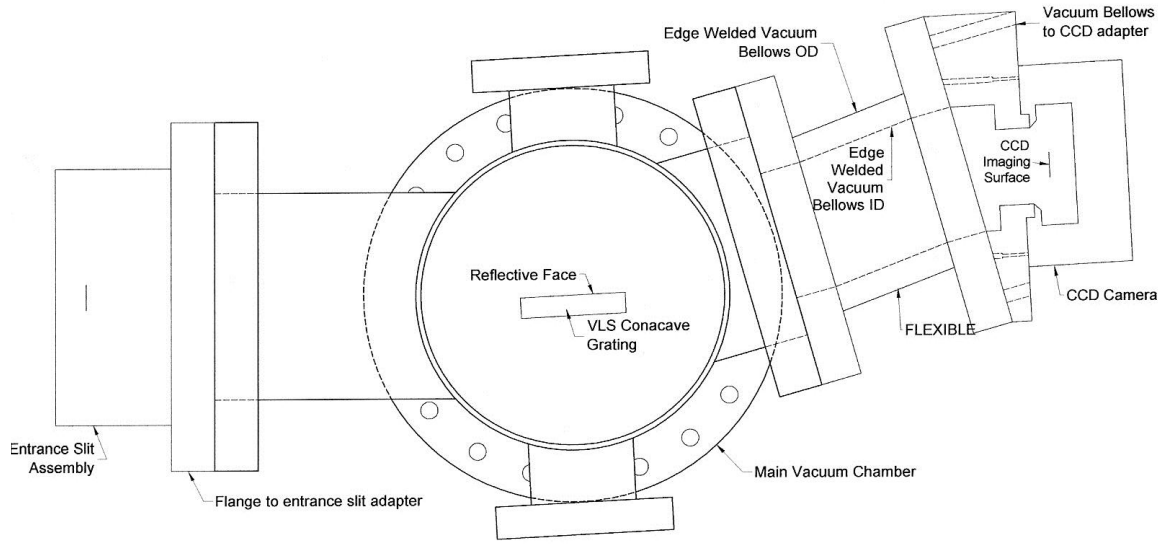
The second grating (Hitachi 001-0450 [156]) has a central ruling density σ_0 of 2400 lines/mm with a blaze angle of 1.9 degrees and a blaze wavelength of 1.5 degrees. The focal plane is flat in the 15 – 100 Å wavelength region (Figure B.1c) with reciprocal dispersion ranging from 1.5 – 3.7 Å/mm [157] at a grazing incidence of 1.35 degrees. The radius of curvature of the concave spherical face is 15920 ±20 mm.

When using the 1200 line/mm grating an Andor Technology iKon-M 934 DO Series back-thinned CCD camera collected EUV spectra. It is uncoated, windowless, cooled to -70° Celsius and mounted via a 6" conflat flange that places the CCD in vacuum. It had a 1024×1024 array of $13 \mu\text{m} \times 13 \mu\text{m}$ pixels. The Andor iKon was a ‘loaner’ camera from Andor that was used while awaiting the arrival of the Andor Newton described in the subsequent paragraph. It was coincidental that the iKon was only used with the 1200 line/mm grating and the Newton was only used with the 2400 line/mm grating.

When using the 2400 line/mm grating an Andor Technology Newton DO920P-BN-9HC Series back-thinned CCD detector recorded spectra. It is uncoated, windowless, cooled to -70° Celsius and mounted in the same way that the iKon was, with a 6" conflat flange. The active area of the CCD is a 1024×256 array of $26 \mu\text{m} \times 26 \mu\text{m}$ pixels, with a rectangular aspect ratio that more closely matches the geometry of the flat focal plane than the square CCD found in the iKon.

The diffraction grating is held in an optical mount (Lees) on a rotational stage (Ealing Electro-Optics) in the center of a custom cylindrical stainless steel vacuum chamber (manufactured by the Kurt J. Lesker Company), connected to the CCD camera by a custom edge-welded metal bellows (manufactured by Metal Flex Welded Bellows, Inc.). The CCD was positioned in the flat-field focal plane of the diffraction grating using a pair of translation stages (Newport Corporation UMR12 series) outfitted with high-strength micrometers (Newport Corporation BM series) and a rotational stage (Newport Corporation UTR series) capable of withstanding the compressive force of the vacuum upon the edge-welded bellows. The Kurt J. Lesker vacuum chamber was connected to the experimental chamber by a hydroform bellows, manually operated gate valve, filter wheel and entrance slit assembly (taken from an Acton VM-502 vacuum monochromator) in that order. The entire flat-field spectrometer assembly was mounted on rails and could be moved transversely by up to 25 mm with respect to the target chamber using another BM series micrometer with the degree of freedom provided by the hydroform bellows.

To block infrared laser light while transmitting EUV, metal filters with thickness $< 1 \mu\text{m}$ were used. Depending on the spectral regime being observed, filters



Flat-field Spectrometer Vacuum Chamber Layout

Figure B.2: Schematic of the vacuum enclosure for the flat-field spectrometer.

made of aluminum (0.25, 0.4 or 0.8 μm), nickel (0.1, 0.2 or 0.4 μm) or zirconium (0.2 μm) were installed. The filters are extremely fragile, and were frequently damaged when > 50 mJ of femtosecond pulse energy impinged upon the them. However, jets of large clusters usually absorbed enough energy to ‘protect’ the filter from the laser. Up to three filters were installed at once in a filter wheel ~ 1 cm in front of the entrance slit to the spectrometer, approximately 60 cm away from the laser-produced plasma.

At the grazing incidence angles of 1.35 and 3 degrees in which they are used, the concave gratings image the entrance slit to the CCD surface with extremely small numerical apertures NA of ~ 0.005 and ~ 0.011 for the 2400 and 1200 line/mm gratings, respectively. However, even the longest EUV wavelength λ_0 at which the spectrometer operates is short enough that this still corresponds to a diffraction-

limited imaged spot radius $w_0 = \lambda_0/(\pi\text{NA})$ that is never larger than ~ 500 nm, more than an order of magnitude smaller than the entrance slit width and CCD pixel size. Thus in practice the maximum attainable spectral resolution of the spectrometer is fundamentally limited by the pixel size of the CCD detector being used. However, for all data presented in this dissertation the resolution was limited by the entrance slit width, usually set to $\sim 100 \mu\text{m}$, chosen because the natural width of the spectral lines typically emitted from the plasma was typically of order 0.5 \AA . Further restricting the slit width attenuated the signal without significantly improving our ability to distinguish adjacent spectral lines.

Bibliography

- [1] T. H. Maiman. Stimulated optical radiation in ruby. *Nature*, 187:493 – 494, Aug 1960.
- [2] D. J. Richardson, J. Nilsson, and W. A. Clarkson. High power fiber lasers: current status and future perspectives. *J. Opt. Soc. Am. B*, 27(11):B63–B92, Nov 2010.
- [3] V. Yanovsky, V. Chvykov, G. Kalinchenko, P. Rousseau, T. Planchon, T. Matsuoka, A. Maksimchuk, J. Nees, G. Cheriaux, G. Mourou, and K. Krushelnick. Ultra-high intensity- 300-tw laser at 0.1 hz repetition rate. *Opt. Express*, 16(3):2109–2114, Feb 2008.
- [4] E. Goulielmakis, M. Schultze, M. Hofstetter, V. S. Yakovlev, J. Gagnon, M. Uiberacker, A. L. Aquila, E. M. Gullikson, D. T. Attwood, R. Kienberger, F. Krausz, and U. Kleineberg. Single-cycle nonlinear optics. *Science*, 320(5883):1614–1617, 2008.
- [5] T. Brabec and F. Krausz. Intense few-cycle laser fields: Frontiers of nonlinear optics. *Rev. Mod. Phys.*, 72:545–591, Apr 2000.
- [6] R. G. Meyerand and A. F. Haught. Gas breakdown at optical frequencies. *Phys. Rev. Lett.*, 11:401–403, Nov 1963.
- [7] F. J. McClung and R. W. Hellwarth. Giant optical pulsations from ruby. *Journal of Applied Physics*, 33(3):828–829, 1962.
- [8] H.A. Haus. Mode-locking of lasers. *Selected Topics in Quantum Electronics, IEEE Journal of*, 6(6):1173 –1185, nov/dec 2000.
- [9] P. Maine, D. Strickland, P. Bado, M. Pessot, and G. Mourou. Generation of ultrahigh peak power pulses by chirped pulse amplification. *Quantum Electronics, IEEE Journal of*, 24(2):398–403, Feb 1988.
- [10] M. D. Perry and G. Mourou. Terawatt to petawatt subpicosecond lasers. *Science*, 264(5161):917–924, 1994.
- [11] D. Umstadter. Relativistic laser-plasma interactions. *Journal of Physics D: Applied Physics*, 36(8):R151, 2003.
- [12] L. V. Keldysh. Ionization in the field of a strong electromagnetic wave. *Soviet Physics JETP*, 20(5):1307, 1965.
- [13] C. Winterfeldt, C. Spielmann, and G. Gerber. Colloquium: Optimal control of high-harmonic generation. *Rev. Mod. Phys.*, 80:117–140, Jan 2008.

- [14] F. Brizuela, G. Vaschenko, C. Brewer, M. Grisham, C. Menoni, M. Marconi, J. Rocca, W. Chao, J. Liddle, E. Anderson, D. Attwood, A. Vinogradov, I. Artioukov, Y. Pershyn, and V. Kondratenko. Reflection mode imaging with nanoscale resolution using a compact extreme ultraviolet laser. *Opt. Express*, 13(11):3983–3988, May 2005.
- [15] A. Rousse, C. Rischel, and J.-C. Gauthier. Femtosecond x-ray crystallography. *Rev. Mod. Phys.*, 73:17–31, Jan 2001.
- [16] J. Filevich, K. Kanizay, M. C. Marconi, J. L. A. Chilla, and J. J. Rocca. Dense plasma diagnostics with an amplitude-division soft-x-ray laser interferometer based on diffraction gratings. *Opt. Lett.*, 25(5):356–358, Mar 2000.
- [17] V. Banine and R. Moors. Plasma sources for euv lithography exposure tools. *Journal of Physics D: Applied Physics*, 37(23):3207, 2004.
- [18] P. Sprangle, E. Esarey, A. Ting, and G. Joyce. Laser wakefield acceleration and relativistic optical guiding. *Applied Physics Letters*, 53(22):2146–2148, nov 1988.
- [19] H. Hora. Self-focusing of laser beams in a plasma by ponderomotive forces. *Zeitschrift fr Physik A Hadrons and Nuclei*, 226:156–159, 1969.
- [20] T. Tajima and J. M. Dawson. Laser electron accelerator. *Phys. Rev. Lett.*, 43(4):267–270, Jul 1979.
- [21] R. Kodama, H. Shiraga, K. Shigemori, Y. Toyama, S. Fujioka, H. Azechi, H. Fujita, H. Habara, T. Hall, Y. Izawa, T. Jitsuno, Y. Kitagawa, K. M. Krushelnick, K. L. Lancaster, K. Mima, K. Nagai, M. Nakai, H. Nishimura, T. Norimatsu, P. A. Norreys, S. Sakabe, K. A. Tanaka, A. Youssef, M. Zepf, and T. Yamanaka. Nuclear fusion: Fast heating scalable to laser fusion ignition. *Nature*, 418:933–934, aug 2002.
- [22] J. D. Kmetec, C. L. Gordon, J. J. Macklin, B. E. Lemoff, G. S. Brown, and S. E. Harris. Mev x-ray generation with a femtosecond laser. *Phys. Rev. Lett.*, 68:1527–1530, Mar 1992.
- [23] M. Protopapas, C. H. Keitel, and P. L. Knight. Atomic physics with super-high intensity lasers. *Reports on Progress in Physics*, 60(4):389, 1997.
- [24] M.M. Murnane, H.C. Kapteyn, R.D. Mordecai, and R.W. Falcone. Ultrafast x-ray pulses from laser-produced plasmas. *Science*, 251(4993):531–536, 1991.
- [25] M. Hegelich, S. Karsch, G. Pretzler, D. Habs, K. Witte, W. Guenther, M. Allen, A. Blazevic, J. Fuchs, J. C. Gauthier, M. Geissel, P. Audebert, T. Cowan, and M. Roth. Mev ion jets from short-pulse-laser interaction with thin foils. *Phys. Rev. Lett.*, 89:085002, Aug 2002.

- [26] R. Volkov, D. Golishnikov, V. Gordienko, P. Mikheev, A. Savelev, V. Sevastyanov, V. Chernysh, and O. Chutko. Neutron generation in dense femtosecond laser plasma of a structured solid target. *JETP Letters*, 72:401–404, 2000. 10.1134/1.1335116.
- [27] T. Ditmire, T. Donnelly, R. W. Falcone, and M. D. Perry. Strong x-ray emission from high-temperature plasmas produced by intense irradiation of clusters. *Phys. Rev. Lett.*, 75:3122–3125, Oct 1995.
- [28] T. Ditmire, T. Donnelly, A. M. Rubenchik, R. W. Falcone, and M. D. Perry. Interaction of intense laser pulses with atomic clusters. *Phys. Rev. A*, 53:3379–3402, May 1996.
- [29] C. G. Durfee and H. M. Milchberg. Light pipe for high intensity laser pulses. *Phys. Rev. Lett.*, 71(15):2409–2412, Oct 1993.
- [30] D. F. Price, R. M. More, R. S. Walling, G. Guethlein, R. L. Shepherd, R. E. Stewart, and W. E. White. Absorption of ultrashort laser pulses by solid targets heated rapidly to temperatures 1-1000 ev. *Phys. Rev. Lett.*, 75:252–255, Jul 1995.
- [31] G. A. Mourou, T. Tajima, and S. V. Bulanov. Optics in the relativistic regime. *Rev. Mod. Phys.*, 78:309–371, Apr 2006.
- [32] B. Dromey, S. Kar, M. Zepf, and P. Foster. The plasma mirror—a subpicosecond optical switch for ultrahigh power lasers. *Review of Scientific Instruments*, 75(3):645–649, 2004.
- [33] A. Jullien, O. Albert, F. Burgy, G. Hamoniaux, J.-P. Rousseau, J.-P. Chambaret, F. Augé-Rochereau, G. Chériaux, J. Etchepare, N. Minkovski, and S. M. Satiel. 10^{-10} temporal contrast for femtosecond ultraintense lasers by cross-polarized wave generation. *Opt. Lett.*, 30(8):920–922, Apr 2005.
- [34] E. W. Becker, K. Bier, and W. Henkes. Strahlen aus kondensierten atomen und molekeln im hochvakuum. *Zeitschrift fr Physik A Hadrons and Nuclei*, 146:333–338, 1956. 10.1007/BF01330428.
- [35] A. W. Castleman and R. G. Keesee. Gas-phase clusters: Spanning the states of matter. *Science*, 241(4861):36–42, 1988.
- [36] O. F. Hagena. Nucleation and growth of clusters in expanding nozzle flows. *Surface Science*, 106(13):101 – 116, 1981.
- [37] R. A. Smith, T. Ditmire, and J. W. G. Tisch. Characterization of a cryogenically cooled high-pressure gas jet for laser/cluster interaction experiments. *Review of Scientific Instruments*, 69(11):3798–3804, 1998.
- [38] O. F. Hagena. Condensation in free jets: Comparison of rare gases and metals. *Zeitschrift fr Physik D Atoms, Molecules and Clusters*, 4:291–299, 1987.

- [39] O. F. Hagena and W. Obert. Cluster formation in expanding supersonic jets: Effect of pressure, temperature, nozzle size, and test gas. *The Journal of Chemical Physics*, 56(5):1793–1802, 1972.
- [40] H. Lu, G. Ni, R. Li, and Z. Xu. An experimental investigation on the performance of conical nozzles for argon cluster formation in supersonic jets. *The Journal of Chemical Physics*, 132(12):124303, 2010.
- [41] O. Danylchenko, S. Kovalenko, and V. Samovarov. Experimental verification of the hagena relation for large clusters formed in a conical nozzle. *Technical Physics Letters*, 34:1037–1040, 2008. 10.1134/S1063785008120146.
- [42] K. Y. Kim, V. Kumarappan, and H. M. Milchberg. Measurement of the average size and density of clusters in a gas jet. *Applied Physics Letters*, 83(15):3210–3212, 2003.
- [43] R. Klingelhofer and H. O. Moser. Production of large hydrogen clusters in condensed molecular beams. *Journal of Applied Physics*, 43(11):4575–4579, 1972.
- [44] J. Wrmer, M. Joppien, and T. Mller. Mass determination of free van der waals clusters from absorption and scattering measurements. *Chemical Physics Letters*, 182(6):632 – 636, 1991.
- [45] R. Karnbach, M. Joppien, J. Stapelfeldt, J. Wormer, and T. Moller. Clulu: An experimental setup for luminescence measurements on van der waals clusters with synchrotron radiation. *Review of Scientific Instruments*, 64(10):2838 – 2849, oct 1993.
- [46] J. Farges, M. F. de Feraudy, B. Raoult, and G. Torchet. Noncrystalline structure of argon clusters. ii. multilayer icosahedral structure of ar_n clusters $50 < n < 750$. *The Journal of Chemical Physics*, 84(6):3491–3501, 1986.
- [47] U. Buck and R. Krohne. Cluster size determination from diffractive he atom scattering. *The Journal of Chemical Physics*, 105(13):5408–5415, 1996.
- [48] J. Wrmer, V. Guzielski, J. Stapelfeldt, and T. Mller. Fluorescence excitation spectroscopy of xenon clusters in the vuv. *Chemical Physics Letters*, 159(4):321 – 326, 1989.
- [49] X. Gao, X. Wang, B. Shim, A. V. Arefiev, R. Korzekwa, and M. C. Downer. Characterization of cluster/monomer ratio in pulsed supersonic gas jets. *Applied Physics Letters*, 100(6):064101 –064101–4, feb 2012.
- [50] E. Parra, S. J. McNaught, and H. M. Milchberg. Characterization of a cryogenic, high-pressure gas jet operated in the droplet regime. *Review of Scientific Instruments*, 73(2):468–475, 2002.

- [51] P. Walzel. *Ullmann's Encyclopedia of Industrial Chemistry*, volume B2, pages 6.1 – 6.14. Weinheim, 5th edition, 1988.
- [52] S. P. Lin and R. D. Reitz. Drop and spray formation from a liquid jet. *Annual Review of Fluid Mechanics*, 30(1):85–105, 1998.
- [53] A. McPherson, B.D. Thompson, A.B. Borisov, K. Boyer, and C.K. Rhodes. Multiphoton-induced x-ray emission at 45 keV from Xe atoms with multiple core vacancies. *Nature*, 370:631–634, 1994.
- [54] K. Boyer, B. D. Thompson, A. McPherson, and C. K. Rhodes. Evidence for coherent electron motions in multiphoton x-ray production from Kr and Xe clusters. *Journal of Physics B: Atomic, Molecular and Optical Physics*, 27(18):4373, 1994.
- [55] T. Ditmire, R. A. Smith, R. S. Marjoribanks, G. Kulcsar, and M. H. R. Hutchinson. X-ray yields from Xe clusters heated by short pulse high intensity lasers. *Applied Physics Letters*, 71(2):166–168, 1997.
- [56] Y. L. Shao, T. Ditmire, J. W. G. Tisch, E. Springate, J. P. Marangos, and M. H. R. Hutchinson. Multi-keV electron generation in the interaction of intense laser pulses with Xe clusters. *Phys. Rev. Lett.*, 77:3343–3346, Oct 1996.
- [57] E. Parra, I. Alexeev, J. Fan, K. Y. Kim, S. J. McNaught, and H. M. Milchberg. X-ray and extreme ultraviolet emission induced by variable pulse-width irradiation of Ar and Kr clusters and droplets. *Phys. Rev. E*, 62:R5931–R5934, Nov 2000.
- [58] M. Lezius, S. Dobosz, D. Normand, and M. Schmidt. Explosion dynamics of rare gas clusters in strong laser fields. *Phys. Rev. Lett.*, 80:261–264, Jan 1998.
- [59] K. Krushelnick, E. L. Clark, Z. Najmudin, M. Salvati, M. I. K. Santala, M. Tatarakis, A. E. Dangor, V. Malka, D. Neely, R. Allott, and C. Danson. Multi-MeV ion production from high-intensity laser interactions with underdense plasmas. *Phys. Rev. Lett.*, 83:737–740, Jul 1999.
- [60] V. P. Yanovsky, T. E. Cowan, G. Hays, T. Ditmire, J. Zweiback, and K. B. Wharton. Nuclear fusion from explosions of femtosecond laser-heated deuterium clusters. *Nature*, 398:489–492, 1999.
- [61] I. Alexeev, T. M. Antonsen, K. Y. Kim, and H. M. Milchberg. Self-focusing of intense laser pulses in a clustered gas. *Phys. Rev. Lett.*, 90:103402, Mar 2003.
- [62] H. M. Milchberg, S. J. McNaught, and E. Parra. Plasma hydrodynamics of the intense laser-cluster interaction. *Phys. Rev. E*, 64:056402, Oct 2001.
- [63] K. Y. Kim, I. Alexeev, E. Parra, and H. M. Milchberg. Time-resolved explosion of intense-laser-heated clusters. *Phys. Rev. Lett.*, 90:023401, Jan 2003.

- [64] C. Rose-Petruck, K. J. Schafer, K. R. Wilson, and C. P. J. Barty. Ultrafast electron dynamics and inner-shell ionization in laser driven clusters. *Phys. Rev. A*, 55:1182–1190, Feb 1997.
- [65] I. Last, I. Schek, and J. Jortner. Energetics and dynamics of coulomb explosion of highly charged clusters. *The Journal of Chemical Physics*, 107(17):6685–6692, 1997.
- [66] T. Ditmire. Simulation of exploding clusters ionized by high-intensity femtosecond laser pulses. *Phys. Rev. A*, 57:R4094–R4097, Jun 1998.
- [67] C. Jungreuthmayer, M. Geissler, J. Zanghellini, and T. Brabec. Microscopic analysis of large-cluster explosion in intense laser fields. *Phys. Rev. Lett.*, 92:133401, Mar 2004.
- [68] T. Taguchi, T. M. Antonsen, and H. M. Milchberg. Resonant heating of a cluster plasma by intense laser light. *Phys. Rev. Lett.*, 92:205003, May 2004.
- [69] I. Last and J. Jortner. Energetics at extremes in coulomb explosion of large finite systems. *Chemical Physics*, (399):218–223, 2012.
- [70] D. Bauer and A. Macchi. Dynamical ionization ignition of clusters in intense short laser pulses. *Phys. Rev. A*, 68:033201, Sep 2003.
- [71] U. Saalmann and J.-M. Rost. Ionization of clusters in intense laser pulses through collective electron dynamics. *Phys. Rev. Lett.*, 91:223401, Nov 2003.
- [72] M Lezius, S Dobosz, D Normand, and M Schmidt. Hot nanoplasmas from intense laser irradiation of argon clusters. *Journal of Physics B: Atomic, Molecular and Optical Physics*, 30(7):L251, 1997.
- [73] T. Fennel, L. Ramunno, and T. Brabec. Highly charged ions from laser-cluster interactions: Local-field-enhanced impact ionization and frustrated electron-ion recombination. *Phys. Rev. Lett.*, 99:233401, Dec 2007.
- [74] S. Namba, N. Hasegawa, K. Nagashima, T. Kawachi, M. Kishimoto, K. Sukegawa, and K. Takiyama. Efficient electron heating in nitrogen clusters irradiated with intense femtosecond laser pulses. *Phys. Rev. A*, 73:013205, Jan 2006.
- [75] F. Dorchies, F. Blasco, C. Bonté, T. Caillaud, C. Fourment, and O. Peyrusse. Observation of subpicosecond x-ray emission from laser-cluster interaction. *Phys. Rev. Lett.*, 100:205002, May 2008.
- [76] T. Shiraishi, M. Mori, and K. Kondo. Estimation of the pulse width of x-ray emission from xe clusters excited by a subpicosecond intense ti:sapphire laser pulse. *Phys. Rev. A*, 65:045201, Mar 2002.

- [77] T. Mocek, J.J. Park, C.M. Kim, H. T. Kim, D. G. Lee, K. H. Hong, and C. H. Nam. Observation of enhanced soft x-ray emission using nitrogen clusters ionized by intense, femtosecond laser. *Journal of Applied Physics*, 93(5):3105–3107, 2003.
- [78] H. Daido. Review of soft x-ray laser researches and developments. *Reports on Progress in Physics*, 65(10):1513, 2002.
- [79] J.A.R Samson. *Techniques of Vacuum Ultraviolet Spectroscopy*. Pied Publications, Lincoln, 1980.
- [80] Thomas Raphael Clark Jr. *Hydrodynamical and Optical Properties of the Plasma Waveguide*. PhD thesis, University of Maryland, College Park, 1998.
- [81] P.G. Gobbi and G.C. Reali. A novel unstable resonator configuration with a self filtering aperture. *Optics Communications*, 52(3):195 – 198, 1984.
- [82] D. Strickland and G. Mourou. Compression of amplified chirped optical pulses. *Optics Communications*, 56(3):219 – 221, 1985.
- [83] P. Maine, D. Strickland, P. Bado, M. Pessot, and G. Mourou. Generation of ultrahigh peak power pulses by chirped pulse amplification. *Quantum Electronics, IEEE Journal of*, 24(2):398 –403, feb 1988.
- [84] K.-Y. Kim. *Measurement of Ultrafast Dynamics in the Interaction of Intense Laser Pulses with Gases, Atomic Clusters, and Plasmas*. PhD thesis, University of Maryland, College Park, 2003.
- [85] E. Esarey, C. B. Schroeder, and W. P. Leemans. Physics of laser-driven plasma-based electron accelerators. *Reviews of Modern Physics*, 81(3):1229, 2009.
- [86] T. M. Antonsen, Jr., J. Palastro, and H. M. Milchberg. Excitation of terahertz radiation by laser pulses in nonuniform plasma channels. *Physics of Plasmas*, 14(3):033107, 2007.
- [87] H. M. Milchberg, C. G. Durfee, and J. Lynch. Application of a plasma waveguide to soft-x-ray lasers. *J. Opt. Soc. Am. B*, 12(4):731–737, 1995.
- [88] J. J. Rocca. Table-top soft x-ray lasers. *Review of Scientific Instruments*, 70(10):3799–3827, 1999.
- [89] A. Butler, A. J. Gonsalves, C. M. McKenna, D. J. Spence, S. M. Hooker, S. Sebban, T. Mocek, I. Bettaibi, and B. Cros. Demonstration of a collisionally excited optical-field-ionization xuv laser driven in a plasma waveguide. *Phys. Rev. Lett.*, 91(20):205001, Nov 2003.
- [90] M. Lewenstein, Ph. Balcou, M. Yu. Ivanov, Anne L’Huillier, and P. B. Corkum. Theory of high-harmonic generation by low-frequency laser fields. *Phys. Rev. A*, 49:2117–2132, Mar 1994.

- [91] H. M. Milchberg, C. G. Durfee III, and T. J. McIlrath. High-order frequency conversion in the plasma waveguide. *Phys. Rev. Lett.*, 75(13):2494–2497, Sep 1995.
- [92] C. Winterfeldt, C. Spielmann, and G. Gerber. Optimal control of high-harmonic generation. *Reviews of Modern Physics*, 80(1):117, 2008.
- [93] P. Arpin, T. Popmintchev, N. L. Wagner, A. L. Lytle, O. Cohen, H. C. Kapteyn, and M. M. Murnane. Enhanced high harmonic generation from multiply ionized argon above 500 eV through laser pulse self-compression. *Phys. Rev. Lett.*, 103(14):143901, 2009.
- [94] A. B. Borisov, A. V. Borovskiy, V. V. Korobkin, A. M. Prokhorov, O. B. Shiryayev, X. M. Shi, T. S. Luk, A. McPherson, J. C. Solem, K. Boyer, and C. K. Rhodes. Observation of relativistic and charge-displacement self-channeling of intense subpicosecond ultraviolet (248 nm) radiation in plasmas. *Phys. Rev. Lett.*, 68:2309–2312, Apr 1992.
- [95] P. Monot, T. Auguste, P. Gibbon, F. Jakober, G. Mainfray, A. Dulieu, M. Louis-Jacquet, G. Malka, and J. L. Miquel. Experimental demonstration of relativistic self-channeling of a multiterawatt laser pulse in an underdense plasma. *Phys. Rev. Lett.*, 74:2953–2956, Apr 1995.
- [96] Y. Ehrlich, C. Cohen, A. Zigler, J. Krall, P. Sprangle, and E. Esarey. Guiding of high intensity laser pulses in straight and curved plasma channel experiments. *Phys. Rev. Lett.*, 77(20):4186–4189, Nov 1996.
- [97] T. Hosokai, M. Kando, H. Dewa, H. Kotaki, S. Kondo, N. Hasegawa, K. Nakajima, and K. Horioka. Optical guidance of terrawatt laser pulses by the implosion phase of a fast z-pinch discharge in a gas-filled capillary. *Opt. Lett.*, 25(1):10–12, Jan 2000.
- [98] A. Butler, D. J. Spence, and S. M. Hooker. Guiding of high-intensity laser pulses with a hydrogen-filled capillary discharge waveguide. *Phys. Rev. Lett.*, 89(18):185003, Oct 2002.
- [99] P. Volfbeyn, E. Esarey, and W. P. Leemans. Guiding of laser pulses in plasma channels created by the ignitor-heater technique. *Physics of Plasmas*, 6(5):2269–2277, 1999.
- [100] E. W. Gaul, S. P. Le Blanc, A. R. Rundquist, R. Zgadzaj, H. Langhoff, and M. C. Downer. Production and characterization of a fully ionized He plasma channel. *Applied Physics Letters*, 77(25):4112–4114, 2000.
- [101] V. Kumarappan, K. Y. Kim, and H. M. Milchberg. Guiding of intense laser pulses in plasma waveguides produced from efficient, femtosecond end-pumped heating of clustered gases. *Phys. Rev. Lett.*, 94:205004, May 2005.

- [102] H. Sheng, K. Y. Kim, V. Kumarappan, B. D. Layer, and H. M. Milchberg. Plasma waveguides efficiently generated by bessel beams in elongated cluster gas jets. *Phys. Rev. E*, 72(3):036411, Sep 2005.
- [103] T. R. Clark and H. M. Milchberg. Optical mode structure of the plasma waveguide. *Phys. Rev. E*, 61(2):1954–1965, Feb 2000.
- [104] F. Dorchies, J. R. Marquès, B. Cros, G. Matthieussent, C. Courtois, T. Vélikorousov, P. Audebert, J. P. Geindre, S. Rebibo, G. Hamoniaux, and F. Amiranoff. Monomode guiding of $10^{16}w/cm^2$ laser pulses over 100 rayleigh lengths in hollow capillary dielectric tubes. *Phys. Rev. Lett.*, 82:4655–4658, Jun 1999.
- [105] S. Jackel, R. Burris, J. Grun, A. Ting, C. Manka, K. Evans, and J. Kosakowskii. Channeling of terawatt laser pulses by use of hollow waveguides. *Opt. Lett.*, 20(10):1086–1088, May 1995.
- [106] C. E. Max, J. Arons, and A. B. Langdon. Self-modulation and self-focusing of electromagnetic waves in plasmas. *Phys. Rev. Lett.*, 33:209–212, Jul 1974.
- [107] A. B. Borisov, A. V. Borovskiy, O. B. Shiryayev, V. V. Korobkin, A. M. Prokhorov, J. C. Solem, T. S. Luk, K. Boyer, and C. K. Rhodes. Relativistic and charge-displacement self-channeling of intense ultrashort laser pulses in plasmas. *Phys. Rev. A*, 45:5830–5845, Apr 1992.
- [108] G.-Z. Sun, E. Ott, Y. C. Lee, and P. Guzdar. Self-focusing of short intense pulses in plasmas. *Physics of Fluids*, 30(2):526–532, 1987.
- [109] P. Sprangle, Cha-Mei Tang, and E. Esarey. Relativistic self-focusing of short-pulse radiation beams in plasmas. *Plasma Science, IEEE Transactions on*, 15(2):145–153, april 1987.
- [110] T. M. Antonsen and P. Mora. Self-focusing and raman scattering of laser pulses in tenuous plasmas. *Phys. Rev. Lett.*, 69:2204–2207, Oct 1992.
- [111] C. A. Coverdale, C. B. Darrow, C. D. Decker, W. B. Mori, K-C. Tzeng, K. A. Marsh, C. E. Clayton, and C. Joshi. Propagation of intense subpicosecond laser pulses through underdense plasmas. *Phys. Rev. Lett.*, 74:4659–4662, Jun 1995.
- [112] E. Esarey, J. Krall, and P. Sprangle. Envelope analysis of intense laser pulse self-modulation in plasmas. *Phys. Rev. Lett.*, 72:2887–2890, May 1994.
- [113] P. Chessa, E. De Wispelaere, F. Dorchies, V. Malka, J. R. Marquès, G. Hamoniaux, P. Mora, and F. Amiranoff. Temporal and angular resolution of the ionization-induced refraction of a short laser pulse in helium gas. *Phys. Rev. Lett.*, 82:552–555, Jan 1999.

- [114] A Pukhov, S Gordienko, S Kiselev, and I Kostyukov. The bubble regime of laserplasma acceleration: monoenergetic electrons and the scalability. *Plasma Physics and Controlled Fusion*, 46(12B):B179, 2004.
- [115] S. Kneip, S. R. Nagel, S. F. Martins, S. P. D. Mangles, C. Bellei, O. Chekhlov, R. J. Clarke, N. Delerue, E. J. Divall, G. Doucas, K. Ertel, F. Fiuza, R. Fonseca, P. Foster, S. J. Hawkes, C. J. Hooker, K. Krushelnick, W. B. Mori, C. A. J. Palmer, K. Ta Phuoc, P. P. Rajeev, J. Schreiber, M. J. V. Streeter, D. Urner, J. Vieira, L. O. Silva, and Z. Najmudin. Near-gev acceleration of electrons by a nonlinear plasma wave driven by a self-guided laser pulse. *Phys. Rev. Lett.*, 103:035002, Jul 2009.
- [116] C. E. Clayton, J. E. Ralph, F. Albert, R. A. Fonseca, S. H. Glenzer, C. Joshi, W. Lu, K. A. Marsh, S. F. Martins, W. B. Mori, A. Pak, F. S. Tsung, B. B. Pollock, J. S. Ross, L. O. Silva, and D. H. Froula. Self-guided laser wakefield acceleration beyond 1 gev using ionization-induced injection. *Phys. Rev. Lett.*, 105:105003, Sep 2010.
- [117] C. G. Durfee, J. Lynch, and H. M. Milchberg. Development of a plasma waveguide for high-intensity laser pulses. *Phys. Rev. E*, 51:2368–2389, Mar 1995.
- [118] H. M. Milchberg, T. R. Clark, C. G. Durfee III, T. M. Antonsen, and P. Mora. Development and applications of a plasma waveguide for intense laser pulses. *Physics of Plasmas*, 3(5):2149–2155, 1996.
- [119] J. Fan, T. R. Clark, and H. M. Milchberg. Generation of a plasma waveguide in an elongated, high repetition rate gas jet. *Applied Physics Letters*, 73(21):3064–3066, nov 1998.
- [120] S. P. Nikitin, I. Alexeev, J. Fan, and H. M. Milchberg. High efficiency coupling and guiding of intense femtosecond laser pulses in preformed plasma channels in an elongated gas jet. *Phys. Rev. E*, 59:R3839–R3842, Apr 1999.
- [121] K. Krushelnick, A. Ting, C. I. Moore, H. R. Burris, E. Esarey, P. Sprangle, and M. Baine. Plasma channel formation and guiding during high intensity short pulse laser plasma experiments. *Phys. Rev. Lett.*, 78:4047–4050, May 1997.
- [122] S.-Y. Chen, G. S. Sarkisov, A. Maksimchuk, R. Wagner, and D. Umstadter. Evolution of a plasma waveguide created during relativistic-ponderomotive self-channeling of an intense laser pulse. *Phys. Rev. Lett.*, 80:2610–2613, Mar 1998.
- [123] Y. Ehrlich, C. Cohen, D. Kaganovich, A. Zigler, R. F. Hubbard, P. Sprangle, and E. Esarey. Guiding and damping of high-intensity laser pulses in long plasma channels. *J. Opt. Soc. Am. B*, 15(9):2416–2423, Sep 1998.

- [124] D. J. Spence and S. M. Hooker. Investigation of a hydrogen plasma waveguide. *Phys. Rev. E*, 63:015401, Dec 2000.
- [125] W. P. Leemans, B. Nagler, A. J. Gonsalves, C. Toth, K. Nakamura, C. G. R. Geddes, E. Esarey, C. B. Schroeder, and S. M. Hooker. GeV electron beams from a centimetre-scale accelerator. *Nature Physics*, 2:696–699, 2006.
- [126] A. G. York, H. M. Milchberg, J. P. Palastro, and T. M. Antonsen. Direct acceleration of electrons in a corrugated plasma waveguide. *Phys. Rev. Lett.*, 100(19):195001, May 2008.
- [127] J. P. Palastro, T. M. Antonsen, S. Morshed, A. G. York, and H. M. Milchberg. Pulse propagation and electron acceleration in a corrugated plasma channel. *Phys. Rev. E*, 77:036405, Mar 2008.
- [128] J. P. Palastro and T. M. Antonsen. Interaction of an ultrashort laser pulse and relativistic electron beam in a corrugated plasma channel. *Phys. Rev. E*, 80:016409, Jul 2009.
- [129] A. Rundquist, C. G. Durfee III, Z. Chang, C. Herne, S. Backus, M. M. Murnane, and H. C. Kapteyn. Phase-Matched Generation of Coherent Soft X-rays. *Science*, 280(5368):1412–1415, 1998.
- [130] M.-C. Chen, P. Arpin, T. Popmintchev, M. Gerrity, B. Zhang, M. Seaberg, D. Popmintchev, M. M. Murnane, and H. C. Kapteyn. Bright, coherent, ultrafast soft x-ray harmonics spanning the water window from a tabletop light source. *Phys. Rev. Lett.*, 105:173901, Oct 2010.
- [131] P. B. Corkum. Plasma perspective on strong field multiphoton ionization. *Phys. Rev. Lett.*, 71:1994–1997, Sep 1993.
- [132] E. A. Gibson, A. Paul, N. Wagner, R. Tobey, D. Gaudiosi, S. Backus, I. P. Christov, A. Aquila, E. M. Gullikson, D. T. Attwood, M. M. Murnane, and H. C. Kapteyn. Coherent soft x-ray generation in the water window with quasi-phase matching. *Science*, 302(5642):95–98, 2003.
- [133] R. Tobey H. Green S. Weiman I. P. Christov M. M. Murnane H. C. Kapteyn A. Paul, R. A. Bartels and S. Backus. Quasi-phase-matched generation of coherent extreme-ultraviolet light. *Nature*, 421:51 – 54, Jan 2003.
- [134] M. Zepf, B. Dromey, M. Landreman, P. Foster, and S. M. Hooker. Bright quasi-phase-matched soft-x-ray harmonic radiation from argon ions. *Phys. Rev. Lett.*, 99:143901, Oct 2007.
- [135] X. Zhang, A. L. Lytle, T. Popmintchev, X. Zhou, H. C. Kapteyn, and M. M. Murnane. Quasi-phase-matching and quantum-path control of high-harmonic generation using counterpropagating light. *Nature Physics*, 3(4):270–275, Apr 2007.

- [136] O. Cohen, X. Zhang, A. L. Lytle, T. Popmintchev, M. M. Murnane, and H. C. Kapteyn. Grating-assisted phase matching in extreme nonlinear optics. *Phys. Rev. Lett.*, 99:053902, Jul 2007.
- [137] E. Seres Ch. Streltsov P. Wobrauschek Ch. Spielmann J. Seres, V. S. Yakovlev and F. Krausz. Coherent superposition of laser-driven soft-x-ray harmonics from successive sources. *Nature Physics*, 3:878–883, 2007.
- [138] A. Willner, F. Tavella, M. Yeung, T. Dzelzainis, C. Kamperidis, M. Bakarezos, D. Adams, M. Schulz, R. Riedel, M. C. Hoffmann, W. Hu, J. Rossbach, M. Drescher, N. A. Papadogiannis, M. Tatarakis, B. Dromey, and M. Zepf. Coherent control of high harmonic generation via dual-gas multijet arrays. *Phys. Rev. Lett.*, 107:175002, Oct 2011.
- [139] J. D. Lawson. Lasers and accelerators. *Nuclear Science, IEEE Transactions on*, 26(4):4217–4219, June 1979.
- [140] W. D. Kimura, G. H. Kim, R. D. Romea, L. C. Steinhauer, I. V. Pogorelsky, K. P. Kusche, R. C. Fernow, X. Wang, and Y. Liu. Laser acceleration of relativistic electrons using the inverse cherenkov effect. *Phys. Rev. Lett.*, 74(4):546–549, Jan 1995.
- [141] B. D. Layer, A. York, T. M. Antonsen, S. Varma, Y.-H. Chen, Y. Leng, and H. M. Milchberg. Ultrahigh-intensity optical slow-wave structure. *Phys. Rev. Lett.*, 99(3):035001, Jul 2007.
- [142] B. D. Layer, A. G. York, S. Varma, Y. H. Chen, and H. M. Milchberg. Periodic index-modulated plasma waveguide. *Opt. Express*, 17(6):4263–4267, 2009.
- [143] L. Schachter. *Beam-Wave Interaction in Periodic and Quasi-Periodic Structures*. Springer-Verlag, Dec 1979.
- [144] A. G. York. *Chapter 3, Novel Applications of High Intensity Femtosecond Lasers to Particle Acceleration and Terahertz Generation*. PhD thesis, University of Maryland, College Park, 2008.
- [145] R. C. Elton. Extension of $3p \rightarrow 3s$ ion lasers into the vacuum ultraviolet region. *Appl. Opt.*, 14(1):97–101, Jan 1975.
- [146] D. L. Matthews, P. L. Hagelstein, M. D. Rosen, M. J. Eckart, N. M. Ceglio, A. U. Hazi, H. Medeki, B. J. MacGowan, J. E. Trebes, B. L. Whitten, E. M. Campbell, C. W. Hatcher, A. M. Hawryluk, R. L. Kauffman, L. D. Pleasance, G. Rambach, J. H. Scofield, G. Stone, and T. A. Weaver. Demonstration of a soft x-ray amplifier. *Phys. Rev. Lett.*, 54:110–113, Jan 1985.
- [147] S. Hulin, T. Auguste, P. D’Oliveira, P. Monot, S. Jacquemot, L. Bonnet, and E. Lefebvre. Soft-x-ray laser scheme in a plasma created by optical-field-induced ionization of nitrogen. *Phys. Rev. E*, 61:5693–5700, May 2000.

- [148] S. Dobosz, P. D'Oliveira, S. Hulin, P. Monot, F. Réau, and T. Auguste. Space- and time-resolved density measurements of a high-intensity laser-produced plasma for x-ray laser studies. *Phys. Rev. E*, 65:047403, Apr 2002.
- [149] T. Ditmire, R. A. Smith, J. W. G. Tisch, and M. H. R. Hutchinson. High intensity laser absorption by gases of atomic clusters. *Phys. Rev. Lett.*, 78:3121–3124, Apr 1997.
- [150] C. Prigent, C. Deiss, E. Lamour, J.-P. Rozet, D. Vernhet, and J. Burgdörfer. Effect of pulse duration on the x-ray emission from ar clusters in intense laser fields. *Phys. Rev. A*, 78:053201, Nov 2008.
- [151] Yu Ralchenko, A. E. Kramida, J. Reader, and Nist A. S. D. Team. NIST Atomic Spectra Database (version 3.1.5), 2008.
- [152] R. G. Fowler and W. R. Atkinson. Electron recombination in atomic hydrogen. *Phys. Rev.*, 113:1268–1269, Mar 1959.
- [153] Aghapi G. Mordovanakis, James Easter, Natalia Naumova, Konstantin Popov, Paul-Edouard Masson-Laborde, Bixue Hou, Igor Sokolov, Gérard Mourou, Igor V. Glazyrin, Wojciech Rozmus, Valery Bychenkov, John Nees, and Karl Krushelnick. Quasimonoenergetic electron beams with relativistic energies and ultrashort duration from laser-solid interactions at 0.5 khz. *Phys. Rev. Lett.*, 103:235001, Dec 2009.
- [154] J. F. O'Hanlon. *A User's Guide to Vacuum Technology*. John Wiley & Sons, Inc., 1989.
- [155] T. Harada and T. Kita. Mechanically ruled aberration-corrected concave gratings. *Appl. Opt.*, 19(23):3987–3993, Dec 1980.
- [156] N. Nakano, H. Kuroda, T. Kita, and T. Harada. Development of a flat-field grazing-incidence xuv spectrometer and its application in picosecond xuv spectroscopy. *Appl. Opt.*, 23(14):2386–2392, Jul 1984.
- [157] M. B. Chowdhuri, S. Morita, and M. Goto. Characteristics of an absolutely calibrated flat-field extreme ultraviolet spectrometer in the 10-130 Å range for fusion plasma diagnostics. *Appl. Opt.*, 47(2):135–146, Jan 2008.